B.O. ANAZODO

DEVELOPMENT OF NIOBIUM SILICIDE BASED ALLOYS WITH REFRACTORY METALS AND Sn AND Ge ADDITIONS FOR GAS TURBINE APPLICATION

MPhil

2014

DEVELOPMENT OF NIOBIUM SILICIDE BASED ALLOYS WITH REFRACTORY METALS AND Sn AND Ge ADDITIONS FOR GAS TURBINE APPLICATION

By

Boniface Obi Anazodo

A Thesis Submitted to the University of Sheffield for Degree of MPhil

DEPARTMENT OF MATERIALS SCIENCE AND ENGINEERING

NOVEMBER 2014

DEDICATION

To the pure, righteous and downtrodden

To the people of **BIAFRA**

To Anazodo's family

Abstract

In this thesis, the microstructures of Nb-Ti-Si-Hf-Mo-W-Sn-Ge-Cr-Al niobium silicide based alloys in as cast (AC) and heat treated (HT = 1500 °C / 100 h) conditions, macrohardness and oxidation behaviour (800 °C, 1200 °C or 1500 °C for ≤ 100 h) are reported. There was strong evidence of solid and liquid miscibility gaps, strong partitioning of Mo and W to Nb_{ss}, and stabilisation of cubic primitive (cP8) Nb_3Sn (A15) in the alloys of this study. Ternary eutectic consisting of Nb_{ss} + Nb_3Sn + βNb_5Si_3 formed in the alloys of this study where the A15 formed in the as cast alloy.

In Nb-11Ti-18Si-1Hf-6Mo-2.5W-xSn-xGe (x = 2; alloy BA1 and x = 5; alloy BA6), the phases present in the alloys were β(Nb, Ti)$_5Si_3$, α(Nb, Ti)$_5Si_3$, (Nb, Mo)$_{ss}$ and HfO_2 (BA1-AC), α(Nb, Ti)$_5Si_3$, (Nb, Mo)$_{ss}$, A15 and HfO_2 (BA1-HT); β(Nb, Ti)$_5Si_3$, (Nb, Mo)$_{ss}$, A15 and HfO_2 (BA6-AC), and α(Nb, Ti)$_5Si_3$, (Nb, Mo)$_{ss}$ no Si, A15, HfO_2 and TiN (BA6-HT). The critical concentration of Sn required for formation of A15 in the as cast alloy was in the range 1.8 at% < Sn < 4 at%.

In Nb-11Ti-18Si-1Hf-6Mo-2.5W-xSn-xGe-xCr-xAl (x = 2; alloy BA5 and x = 5; alloys BA2 and BA3), there was significant loss of Sn for x = 5 at%Sn. The phases present in the alloys were β(Nb, Ti)$_5Si_3$, (Nb, Ti)$_{ss}$ and HfO_2 (BA5-AC), α(Nb, Ti)$_5Si_3$, (Nb, Mo)$_{ss}$ no Si, A15, HfO_2 and TiN (BA5-HT); β(Nb, Ti)$_5Si_3$, (Nb, Mo)$_{ss}$, A15, C14 (Nb, Ti)Cr_2 Laves and HfO_2 (BA2-AC), β(Nb, Ti)$_5Si_3$, (Nb, Mo)$_{ss}$ no Si, A15, HfO_2 and TiN (BA2-HT); β(Nb, Ti)$_5Si_3$, (Nb, Mo)$_{ss}$ and C14 (Nb, Ti)Cr_2 Laves (BA3-AC), and β(Nb, Ti)$_5Si_3$, (Nb, Mo)$_{ss}$ no Si, A15, HfO_2 and TiN (BA3-HT).

In Nb-xTi-18Si-1Hf-6Mo-2.5W-(5+y)Sn-5Ge-5Cr-5Al (x = 11; alloy BA3b, x = 15; alloy BA7, x = 20; alloy BA4, and y = Sn compensation), there was formation of novel alloys with core / shell macrostructures and stabilisation of ternary beta $Nb_5Si_xX_y$ (X = Sn, Ge, Al; x+y = 3, 0 < x ≤ 2 and 0 < y ≤ 2) silicides.
Niobium silicide based alloy with metal recession rate 0.25 μm / h at 1500 °C after 100 h exposure was discovered in this study. Oxidation products after the 100 h isothermal test were TiO_2, Al_2O_3, SiO_2, Cr_2O_3 and nitrides. The oxides formed continuous and protective film. There was a significant increase in the macrohardness of the alloys of this study after the heat treatment at 1500 °C / 100 h.

Table of Contents

ABSTRACT ..... **II**

TABLE OF CONTENTS ..... **III**

ACKNOWLEDGMENT ..... **VII**

INTRODUCTION ..... **VIII**

CHAPTER 1 ..... **1**

LITERATURE REVIEW 1
1.1 Phase equilibria 1
1.1.1 The Nb-Si system 1
1.1.2 The Nb-Ti system 5
1.1.3 The Si–Ti system 6
1.1.4 The Nb-Si-Ti system 10
1.1.5 The Cr-Nb system 11
1.1.6 The Cr-Si system 13
1.1.7 The Nb-Cr-Si system 16
1.1.8 The Nb-Al-Cr system 19
1.1.9 The Nb-Al-Si system 19
1.1.10 The Cr-Ti system 19
1.1.11 The Cr-Nb-Ti system 26
1.1.12 The Cr-Nb-Mo system 26
1.1.13 The Mo – Si system 27
1.1.14 The Nb-Mo-Si system 29
1.1.15 The Si – W system 30
1.1.16 The Nb–W–Si system 32
1.1.17 The Nb – Sn system 33
1.1.18 The Nb-Si-Sn system 35
1.1.19 The Nb-Ge system 37
1.1.20 The Ge-Nb-Si system 39
1.2 Processing 41
1.2.1 Arc melting 41
1.3 Properties 42
1.3.1 Toughness 43
1.3.2 High temperature strength 47
1.3.3 Oxidation 48
1.4 Summary of the literature review and research objectives 50

CHAPTER 2 ..... **53**

EXPERIMENTAL PROCEDURES 53

2.1 Selection of alloy compositions 53
2.2 Preparation of ingots 56
2.3 Preparation of specimens for microstructure characterisation 57
2.4 Heat treatment 58
2.5 X-ray diffraction 58
2.6 Scanning electron microscopy with quantitative energy dispersive spectrometry 58
2.7 Hardness measurement 59
2.8 Thermo-gravimetric analysis (TGA) 59
2.9 Density measurement 59

CHAPTER 3 60

THE MICROSTRUCTURE OF THE ALLOY Nb-11Ti-18Si-1Hf-6Mo-2.5W-xSn-xGe 60
3.1 Introduction 60
3.2 Experimental 61
3.3 Results 62
3.3.1 Nb-11Ti-18Si-1Hf-6Mo-2.5W-2Sn-2Ge (Alloy BA1) 63
3.3.1.1 As cast 63
3.3.1.2 Heat treated 63
3.3.2 Nb-11Ti-18Si-1Hf-6Mo-2.5W-5Sn-5Ge (Alloy BA6) 64
3.3.2.1 As cast 64
3.3.2.2 Heat treated 65
3.4 Discussion 81
3.4.1 As cast 81
3.4.1.1 Phases present in the cast alloys 81
3.4.1.2 Microstructures of the cast alloys 82
3.4.2 Heat treated 85
3.4.2.1 Phases present after heat treatment 85
3.4.2.2 Microstructures of the heat treated alloys 86
3.4.2.3 Lattice parameters of Nb_{ss}, αNb_5Si_3, βNb_5Si_3 and Nb_3Sn 87
3.5 Conclusions 88

CHAPTER 4 121

THE MICROSTRUCTURE OF Nb-11Ti-18Si-1Hf-6Mo-2.5W-xSn-xGe-xCr-xAl 121
4.1 Introduction ..... **Error! Bookmark not defined.**
4.2 Results ..... **Error! Bookmark not defined.**
4.2.1 Nb-11Ti-18Si-1Hf-6Mo-2.5W-2Sn-2Ge-2Cr-2Al (Alloy BA5) ..... **Error! Bookmark not defined.**
4.2.1.1 As cast ..... **Error! Bookmark not defined.**
4.2.1.2 Heat treated ..... **Error! Bookmark not defined.**

4.2.2 Nb-11Ti-18Si-1Hf-6Mo-2.5W-5Sn-5Ge-5Cr-5Al (Alloy BA3) .....**Error! Bookmark not defined.**
4.2.2.1 As cast ..... **Error! Bookmark not defined.**
4.2.2.2 Heat treated ..... **Error! Bookmark not defined.**
4.2.3 Nb-11Ti-18Si-1Hf-6Mo-2.5W-5Sn-5Ge-5Cr-5Al (Alloy BA2) .....**Error! Bookmark not defined.**
4.2.3.1 As cast ..... **Error! Bookmark not defined.**
4.2.3.2 Heat treated ..... **Error! Bookmark not defined.**
4.3 Discussion ..... **Error! Bookmark not defined.**
4.3.1 The Nb-11Ti-18Si-1Hf-6Mo-2.5W-2Sn-2Ge-2Cr-2Al (Alloy BA5)**Error! Bookmark not defined.**
4.3.1.1 As cast ..... **Error! Bookmark not defined.**
4.3.1.2 Heat treated ..... **Error! Bookmark not defined.**
4.3.2 The Nb-11Ti-18Si-1Hf-6Mo-2.5W-5Sn-5Ge-5Cr-5Al (Alloy BA3)**Error! Bookmark not defined.**
4.3.2.1 As cast ..... **Error! Bookmark not defined.**
4.3.2.2 Heat treated ..... **Error! Bookmark not defined.**
4.3.3 The Nb-11Ti-18Si-1Hf-6Mo-2.5W-5Sn-5Ge-5Cr-5Al (Alloy BA2)**Error! Bookmark not defined.**
4.3.3.1 As cast ..... **Error! Bookmark not defined.**
4.3.3.2 Heat treated ..... **Error! Bookmark not defined.**
4.4 Conclusions ..... **Error! Bookmark not defined.**

CHAPTER 5 159

STUDY OF THE EFFECTS OF Ti CONCENTRATION ON MICROSTRUCTURE OF Nb-xTi-18Si-1Hf-6Mo-2.5W-5Sn-5Ge-5Cr-5Al 159
5.1 Introduction ..... **Error! Bookmark not defined.**
5.2 Experimental ..... **Error! Bookmark not defined.**
5.3 Results ..... **Error! Bookmark not defined.**
5.3.1 Nb-20Ti-18Si-1Hf-6Mo-2.5W-(5+y)Sn-5Ge-5Cr-5Al (Alloy BA4).**Error! Bookmark not defined.**
5.3.1.1 As Cast ..... **Error! Bookmark not defined.**
Alloy 1 ..... **Error! Bookmark not defined.**
Boundary between Alloys 1 and 2 ..... **Error! Bookmark not defined.**
Alloy 2 ..... **Error! Bookmark not defined.**
5.3.1.2 Heat treated ..... **Error! Bookmark not defined.**
Alloy 1 ..... **Error! Bookmark not defined.**
Boundary between Alloys 1 and 2 ..... **Error! Bookmark not defined.**
Alloy 2 ..... **Error! Bookmark not defined.**
5.3.2 Nb-15Ti-18Si-1Hf-6Mo-2.5W-(5+y)Sn-5Ge-5Cr-5Al (Alloy BA7)**Error! Bookmark not defined.**
5.3.3 Nb-11Ti-18Si-1Hf-6Mo-2.5W-(5+y)Sn-5Ge-5Cr-5Al (Alloy BA3b)**Error! Bookmark not defined.**

5.4 Discussion ..... **Error! Bookmark not defined.**
Liquid miscibility gap and core / shell microstructure .... **Error! Bookmark not defined.**
Solid state miscibility gap ..... **Error! Bookmark not defined.**
5.4.1 The Nb-11Ti-18Si-1Hf-6Mo-2.5W-(5+y)Sn-5Ge-5Cr-5Al (BA3b) and Nb-15Ti-18Si-1Hf-6Mo-2.5W-(5+y)Sn-5Ge-5Cr-5Al (BA7).**Error! Bookmark not defined.**
5.4.2 The Nb-20Ti-18Si-1Hf-6Mo-2.5W-(5+y)Sn-5Ge-5Cr-5Al (Alloy BA4) ..... **Error! Bookmark not defined.**
5.4.2.1 As cast ..... **Error! Bookmark not defined.**
Solidification microstructure..... **Error! Bookmark not defined.**
Phase selection ..... **Error! Bookmark not defined.**
5.4.2.2 Heat treated ..... **Error! Bookmark not defined.**
5.5 Conclusions..... **Error! Bookmark not defined.**

CHAPTER 6 160

MACROHARDNESS AND OXIDATION BEHAVIOUR OF SELECTED ALLOYS OF THIS STUDY..... 160
6.1 Introduction..... **Error! Bookmark not defined.**
6.2 Results..... **Error! Bookmark not defined.**
6.2.1 Macrohardness ..... **Error! Bookmark not defined.**
6.2.2 Isothermal oxidation ..... **Error! Bookmark not defined.**
6.2.2.1 Isothermal oxidation at 800 °C ..... **Error! Bookmark not defined.**
Oxidation product after the isothermal oxidation at 800 °C**Error! Bookmark not defined.**
6.2.2.2 Isothermal oxidation at 1200 °C ..... **Error! Bookmark not defined.**
Oxidation product after isothermal oxidation at 1200 °C **Error! Bookmark not defined.**
6.2.2.3 Isothermal oxidation at 1500 °C ..... **Error! Bookmark not defined.**
6.3 Discussion..... **Error! Bookmark not defined.**
6.3.1 Macrohardness ..... **Error! Bookmark not defined.**
6.3.2 The oxidation behaviour at 800 °C ..... **Error! Bookmark not defined.**
Pest oxidation..... **Error! Bookmark not defined.**
6.3.3 The oxidation behaviour at 1200 °C ..... **Error! Bookmark not defined.**
6.3.4 The oxidation behaviour at 1500 °C ..... **Error! Bookmark not defined.**
6.4 Conclusions..... **Error! Bookmark not defined.**

CHAPTER 7 161

CONCLUSIONS AND SUGGESTIONS FOR FUTURE WORK 161
7.1 Conclusions..... **Error! Bookmark not defined.**
7.1.1 Microstructure..... **Error! Bookmark not defined.**
7.1.2 Macrohardness ..... **Error! Bookmark not defined.**
7.1.3 Oxidation..... **Error! Bookmark not defined.**

7.2 Suggestions for future work..... **Error! Bookmark not defined.**

REFERENCES 162

ACKNOWLEDGMENT

This thesis is a culmination of research I carried out in the Department of Materials Science and Engineering at the University of Sheffield starting from January 2011 to November 2014.

The research would have not been possible if not for the sponsorship, guidance and support of many. Therefore I must first and foremost thank Mr Uzo C. Anazodo and Mr Emma T. Uzoezie for sponsorship they gave to me which began in 2009 during my MSc(Eng) programme here at the University of Sheffield; thank my supervisor Professor Panos Tsakiropoulos without him this work would have not been possible; thank the head of the Department of Materials Science and Engineering, Professor W.M Rainforth, the Department of Materials Science and Engineering and the High-temperature Alloys Research Group for financial supports and some fees waiver.

I am also indebted to all the staff and students in the University of Sheffield especially those in the Department of Materials Science and Engineering. The technical staff based in the Hadfield building and Sorby Centre contributed immensely to the success of my research.

I must not forget the sacrifices made by my family; relations and friends. Nnedinma, you endured five (5) years of loneliness may it be crowned with joy and happiness.

Introduction

The progresses in gas-turbine engines in the past years are closely linked to the availability of new materials and improved manufacturing routes. For example, the use of directional solidification (DS) and single crystal (SX) superalloys added 93.3 °C increase in high temperature capabilities more than the usual multi-grain equiaxed cast alloys (Koff, 2004). Improvements in alloy composition give extra enhancement generating a collective temperature capability rise to 125 °C in SX high-pressure nickel based superalloy turbine blades (Bewlay et al., 2003b, Jackson et al., 1996). Application of coating systems and multi-wall blade cooling designs give additional improvements in high temperature capabilities. A typical coating system consists of a bond coat (BC), thermally grown oxide (TGO) and ceramic top coat (Parlakyigit and Karaoglanli, 2014). The bond coat is aluminium rich metallic coating used for oxidation resistance and eliminates the difference in thermal expansion of the substrate metal (superalloy) and the ceramic top coat layer. The ceramic top coat (e.g., yttria-stabilised zirconia) has low thermal conductivity and insulates the superalloy from the hot gases such that the surface temperature of the ceramic top coat can be significantly higher than 1150 °C. The latter is essentially the maximum surface temperature for Ni superalloys due to reasons given in the next paragraph. The ceramic top coat is permeable to oxygen and therefore do not offer oxidation protection to the superalloy (Pint et al., 2006). The TGO is an in-situ formed oxide (αAl_2O_3) at the BC/ Ceramic top coat interface at high temperatures.

Further boost in the temperature capability of the nickel-based superalloys is very unlikely due to the following reasons, one, nickel-based superalloys can suffer incipient melting at 1270 °C – 1316 °C (Koff, 2004, Bewlay et al., 2003b). Two, the ceramic top coat and bond coat damage tolerance and reliability requires improvement because loss of the coatings would raise the surface temperature in the area. Three, the bond-coat and substrate metal interaction zone can soften and melt at temperatures less

than 1250 °C. Thus, there are clear built-in hindrances that limit additional increases in the use temperatures of nickel based superalloys. Therefore, new lightweight high-temperature materials that can operate past the current temperature boundary are required for the development of next generation gas turbine engines that are expected to operate at metal surface temperature of about 1400 °C.

The choice of materials that can meet the present high (> 1200 °C) melting point temperature needs include alloys of the refractory metals (metallic materials with melting points > 2000 °C) such as niobium (Nb), molybdenum (Mo), tantalum (Ta) and tungsten (W); ceramics (inorganic non metallic solids), and composite materials (a mixture of two or more material types).

If a composite material develops during solidification, the composite is in-situ composite and if put together by mechanical means it is ex-situ. Stable in-situ composite systems have the advantages of co-existence in thermodynamic equilibrium of monolithic phases over ex-situ composites. Thus in-situ composite engineering approach has the potential to enable the development of new lightweight materials superior to the nickel based superalloys (Subramanian et al., 1997). The foremost assignment is to build up a refractory metal based solid solution, strengthened by ceramic and or intermetallic phase(s). Intermetallics can be compounds of metals (Taub and Fleischer, 1989) and semi-metals like Si (Sauthoff, 1996). They maintain a particular order in their crystal structure (Taub and Fleischer, 1989), that is, specific type of atoms occupy specific atomic (lattice) site. Some intermetallics are non-stoichiometric meaning they are not strict in site occupancy, and thus can exist over a range of compositions about the ideal stoichiometric ratio. Such deviations manifest as anti-site defects, such as one species taking up the position of another different species, by vacancies, or interstitials solute additions.

In choosing the refractory metal based solid solution, the physical and mechanical properties of each metal must be considered in relation to service requirements. Table 1.1 compares the refractory metals Nb, Mo, Ta, and W. Niobium is the preferred refractory metal due to combination of its properties: the lowest density, good specific strength and DBTT (Ductile-to-Brittle-Transition-Temperature) lower than -50 °C. The latter is a requirement for materials used in aerospace structural applications.

Table 1.1 Comparisons of some physical and mechanical properties of Nb, Mo, Ta and W, data from (Grill and Gnadenberger, 2006).

Physical properties	**Metal**			
	Nb	**Mo**	**Ta**	**W**
Melting point (°C)	2470	2610	2996	3410
Density (g/cm^3)	8.57	10.2	16.6	19.3
Crystal structure	BCC	BCC	BCC	BCC
Ductile-to-Brittle-Transition-Temperature (DBTT) (°C)	-150	-20	-260	300
Young's Modulus (GPa)	110	290	186	358

The next issue is to decide which Nb-based system to employ. The Nb-Si system (Figure 1.1) has eutectic points, niobium solid solution (Nb_{ss}) denoted by β(Nb,Si) and intermetallic silicide phases. One of the intermetallic silicides has melting point above that of Nb, and exists in equilibrium with the Nb_{ss} over a wide range of temperatures (≤ 1700 °C) and Si compositions (≤ 37.5.at %). This endorses the formation of in-situ composites that are stable at high temperatures, an essential requirement for high temperature structural materials. The eutectic allow for solidification processing in which case, eutectic-coupled growth, near-net-shape casting, directional solidification and possibility of growing single crystals would be feasible. Research on the binary Nb-Si and higher order systems confirmed the existence of technical basis for developing materials for very high (> 1200 °C) temperature applications based on Nb_{ss} and Nb_5Si_3 (Subramanian et al., 1997). Monolithic niobium has relatively high fracture toughness but has low ambient temperature strength and very poor creep resistance. Niobium has strong affinity for interstitials especially nitrogen and oxygen (Grill and Gnadenberger, 2006). These interstitials have very negative effects on mechanical properties due to embrittlement and have dramatic effects on the DBTT of Nb. Less than 0.1 at% Nitrogen or 0.6 at% Oxygen raises the DBTT above -50 °C. The pent-oxide of niobium has poor mechanical strength and do not offer long lasting protection (Murakami et al., 2001). Monolithic Nb_5Si_3 has good creep property but has poor fracture toughness and inadequate oxidation resistance. However, the Nb_5Si_3 is non-stoichiometric and could be modified by alloying to improve fracture toughness and oxidation properties (Bewlay et al., 2002, Bewlay et al., 1996). Alloying additions

dissolve in Nb and form solid solution (Nb_{ss}) with improved strength, creep and oxidation properties.

In this study we aim to develop new very-high temperature materials that can be used in the next generation of gas turbine engines.

The objectives of this research are: (1) to systematically study the effects of Mo and W in synergy with Sn and Ge on microstructure of Nb-Ti-Si-Hf silicide based alloys, in the presence and absence of Cr and Al, and (2) to study the oxidation behaviour and macrohardness of selected alloys.

The approach adopted to achieve these objectives included: (a) the use of x-ray diffraction (XRD) and scanning electron microscopy with energy dispersive x-ray spectroscopy (SEM/EDS) to characterise the microstructures of the new alloys; (b) the use of thermogravimetric analysis (TGA) to study the oxidation behaviour at 800 °C and 1200 °C and (c) the use of bulk and glancing angle XRD and SEM to study the oxides formed in the alloys.

This thesis begins with a review of literature on development of Nb silicide based alloys, presented in Chapter 1. At the end of the Chapter 1 is a summary of the literature in relation to research objectives. The experimental techniques are described in Chapter 2; results and discussions are presented in Chapters 3 to 6 while conclusions made and directions for future work pointed out and presented in Chapter 7.

CHAPTER 1

LITERATURE REVIEW

In order to design and develop the new high temperature alloys for this study, this chapter will consider briefly the following binary and ternary phase equilibria: Nb-Si, Nb-Ti, Si-Ti, Nb-Cr, Si-Cr, Ti-Cr, Mo-Si, Si-W, Nb-Sn, Ge-Nb, Nb-Si-Ti, Nb-Cr-Si, Nb-Cr-Al, Nb-Si-Al, Nb-Ti-Cr, Cr-Nb-Mo, Nb-Mo-Si, Nb-W-Si, Nb-Si-Sn and Ge-Nb-Si; review properties of niobium silicide based alloys and property goals.

1.1 Phase equilibria

Phase-selection and stability in alloy systems depend most importantly on the crystal structures of the phases, the alloy chemistry and the temperature (Taub and Fleischer, 1989). Processing route can also play an important role in the stability of phases (Subramanian et al., 1997).

1.1.1 The Nb-Si system

The Nb-Si phase diagram (Figure 1.1) has the following stable phases:

1. The Liquid (L) denoted by Liq in Figure 1.1
2. The terminal body centred cubic (bcc) niobium solid solution with two atoms per unit cell (cI2) Nb_{ss} (prototype W) denoted by β(Nb,Si) in Figure 1.1
3. The tetragonal primitive niobium 3-1 silicide containing thirty-two atoms per unit cell (tP32) Nb_3Si (prototype Ti_3P).
4. The high temperature (ht) body centred tetragonal niobium 5-3 silicide containing thirty-two atoms per unit cell (tI32) βNb_5Si_3 (prototype W_5Si_3).
5. The low temperature (lt) body centred tetragonal niobium 5-3 silicide containing thirty-two atoms per unit cell (tI32) αNb_5Si_3 (prototype Cr_5B_3) denoted by Nb_5Si_3 in Figure 1.1.
6. The hexagonal close packed (hcp) niobium disilicide containing eight atoms per unit cell (hP8) $NbSi_2$ (prototype $CrSi_2$).

7. The face centred cubic (fcc) Silicon with eight atoms per unit cell (cF8) Si_{ss} (prototype C –diamond) denoted by (Si) in Figure 1.1.

Figure 1.1 The Nb-Si system (Yang et al., 2003) was removed.

The aforementioned phases and phase transformations in the Nb-Si system are given in Tables 1.2 and 1.3 respectively. Note that some of the reaction temperatures are different in Figure 1.1 and Table 1.3.

Table 1.2 Crystal structures of phases present in the Nb – Si system. Data from (Okamoto et al., 1990)

Phase	**Composition at% Si**	**Pearson symbol**	**Prototype**	**Lattice parameters (Å)**	
				a	c
β(Nb,Si)	0 – 3.5	cI2	W	3.3067	
(Si)	100	cF8	C (diamond)	5.4309	
Nb_3Si	25	tP32	Ti_3P	10.224	5.189
βNb_5Si_3	37.5 – 40.5	tI32	W_5Si_3	10.040	5.081
αNb_5Si_3	37.5 – 38.5	tI32	Cr_5B_3	6.571	11.889
$NbSi_2$	66.7	hP9	$CrSi_2$	4.81	6.61

Table 1.3 Reactions in the Nb-Si system. Data from (Okamoto et al., 1990).

Reaction	Phase composition (at % Si)			Tempera-ture (°C)	Reaction type
	A	B	C		
$L \rightarrow \beta(Nb,Si)$		0		2469	Freezing
$L \rightarrow \beta(Nb,Si) + Nb_3Si$	17.5	3.5	25	1920	Eutectic
$L + \beta Nb_5Si_3 \rightarrow Nb_3Si$	19	37.5	25	1980	Peritectic
$Nb_3Si \rightarrow \beta(Nb,Si) + \alpha Nb_5Si_3$	25	1.6	37.5	1770	Eutectoid
$L \rightarrow \beta Nb_5Si_3$		38		2520	Congruent
$Nb_3Si + \beta Nb_5Si_3 \rightarrow \alpha Nb_5Si_3$	25	37.5	37.5	1940	Peritectoid
$\beta Nb_5Si_3 \rightarrow \alpha Nb_5Si_3 + NbSi_2$	39.5	38.5	66.7	1650	Eutectoid
$L \rightarrow \beta Nb_5Si_3 + NbSi_2$	57	40.5	66.7	1900	Eutectic
$L \rightarrow NbSi_2$		66.7		1940	Congruent
$L \rightarrow NbSi_2 + (Si)$	98	66.7	100	1400	Eutectic
$L \rightarrow (Si)$		100		1414	Freezing

The Nb-corner of Nb-Si system (Figure 1.2) is of particular interest for this work. The Nb_5Si_3 exhibits solubility width higher for βNb_5Si_3 than αNb_5Si_3 and alloying elements can substitute for Nb or Si in the sub-lattice or fill interstitial-voids and vacancies to form $(Nb,M)_5(Si,X)_3$ where M and X stands for one or more elements substituting for Nb and Si respectively.

Figure 1.2 The Nb_{ss}-rich corner of Nb-Si depicting the compositions of interest (Bewlay et al., 2003b) was removed.

The thermodynamic equilibrium coexistence of the Nb_5Si_3 and Nb_{ss} over a wide range of temperature means that the alloy (in essence an in-situ composite) is thermo-chemically and thermo-physically stable. Thermo-chemical stability means that the phases would not react with each other and would not easily undergo significant changes in chemistry due to variation in temperature. Thermo-physical stability means that the phases would not undergo morphological changes and would act as a couple under mechanical loading due to interface existing between them. Mechanical coupling is important in these in-situ composites for practical applications as it would allow the utilization of multi-component monolithic phases with desired properties.

The βNb_5Si_3 and Nb_3Si at about 1940 °C undergo peritectoid reaction, $Nb_3Si + \beta Nb_5Si_3 \rightarrow \alpha Nb_5Si_3$, and the Nb_3Si eutectoid transformation occur at about 1700 °C according to the reaction $Nb_3Si \rightarrow Nb_{ss} + \alpha Nb_5Si_3$. The eutectoid transformation of Nb_3Si result to fine lamellar microstructure and can be used to produce very fine Nb_{ss} and αNb_5Si_3 microstructure in Nb silicide based alloys. Experiments have shown that the above transformations do not proceed to completion due to slow solid-state transformation kinetics. Thus, significant volume fractions of Nb_3Si and βNb_5Si_3 can be present in the microstructure as metastable phases. The Nb_3Si silicide has less attractive properties than 5-3 silicides and the βNb_5Si_3 exhibits less isotropic properties than the αNb_5Si_3. Therefore, it is desirable to encourage the eutectoid transformation of the Nb_3Si or to suppress its formation via alloying for example alloying with Al, Cr, Ge, Mo and W can suppress the formation of Nb_3Si which is replaced with βNb_5Si_3 (Bewlay et al., 2009, Yang et al., 2007, Ma et al., 2004, Zifu and Tsakiropoulos, 2010). The βNb_5Si_3 can transform to αNb_5Si_3 after heat treatment.

Table 1.4 gives a list of metastable phases identified in Nb-Si system.

Table 1.4 Crystal structures of metastable phases in the Nb-Si system (Schlesinger et al., 1993).

Phase	Composition (at%Si)	Pearson symbol	Prototype
Nb_7Si	8-13	C**	-
Nb_4Si	20	hP*	ε-Fe_3N
Nb_3Si-m	10-22	cP8	Cr_3Si
Nb_3Si-m`	10-27	cF8	Cu
Nb_3Si-m``	25	cP4	$AuCu_3$
Nb_3Si I	25	t**	-
γNb_5Si_3	37.5	hP16	Mn_5Si_3

1.1.2 The Nb-Ti system

Titanium improves the oxidation resistance and fracture toughness of Nb and is considered to be a critical alloying addition in Nb silicide based alloys.

The Nb-Ti phase diagram is shown in Figure 1.3. The equilibrium phases present consist of:

1. The Liquid (L)
2. The room temperature (rt) terminal hexagonal close packed (hcp) alpha titanium solid solution with two atoms per unit cell (hP2) (Ti) (prototype Mg)
3. The body centred cubic (bcc) niobium-titanium solid solution with two atoms per unit cell (cI2) (Ti, Nb) (prototype W)

Niobium has a maximum solubility of about 2 at% in the (Ti) rt whereas in (Ti) ht a continuous solubility exists. Addition of Nb (> 20 at%) to Ti stabilise the (Ti) ht to lower temperatures (see Figure 1.3).

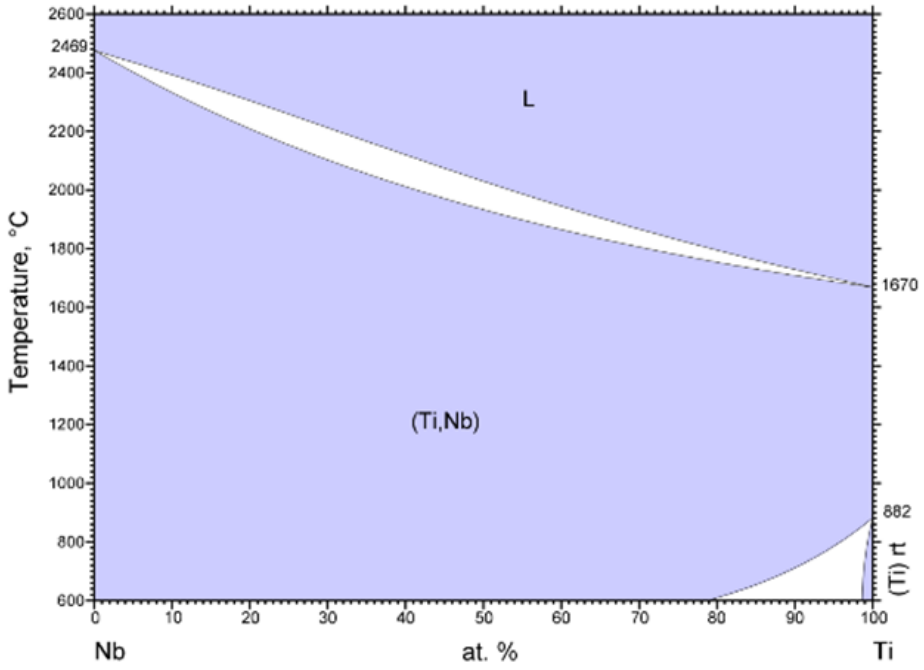

Figure 1.3 The Nb-Ti system (Antonova et al., 2003).

Reprinted with permission of ASM International.

1.1.3 The Si–Ti system

Alloying Nb-Si based systems with Ti opens up the possibility of ternary Si-Ti phases and thus the phase equilibria in the binary Si-Ti is important when designing Nb

silicide based alloys. The Si-Ti phase diagram (Figure 1.4) consists of ten stable

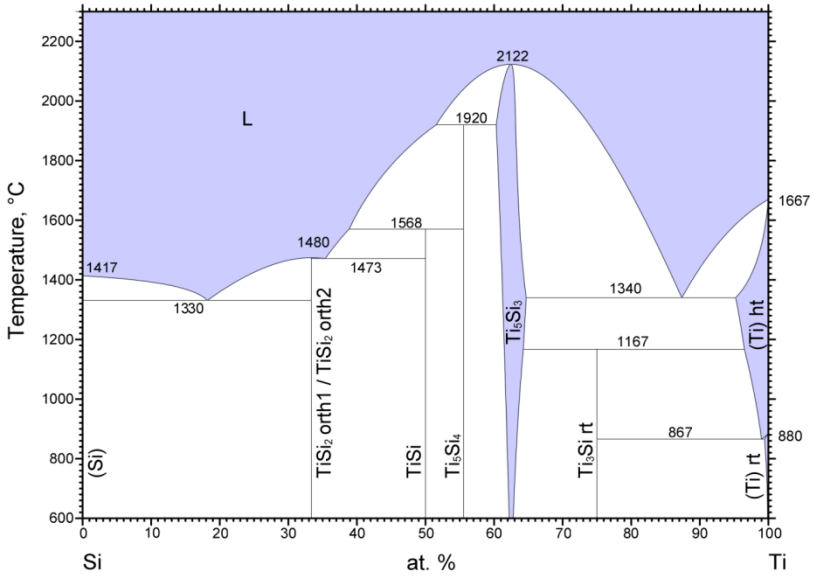

Figure 1.4 The Si-Ti system (Seifert et al., 1996). Note that some of the reaction temperatures are different from those given in Table 1.6. Reprinted with permission of ASM International.

phases. These phases are:

1. The Liquid (L)
2. The room temperature (rt) hexagonal close packed (hcp) alpha-titanium solid solution with two atoms per unit cell (hP2) αTi (prototype Mg) denoted by (Ti) rt in Figure 1.4
3. The high temperature (ht) body centred cubic (bcc) beta-titanium solid solution with two atoms per unit cell (cI2) βTi (prototype W) denoted by (Ti) ht in Figure 1.4
4. The room temperature (rt) tetragonal primitive (tP32) Ti_3Si (prototype Ti_3P) with thirty-two atoms per unit cell
5. The face centred orthorhombic-1 titanium disilicide with twenty-four atoms per unit cell (oF24)$TiSi_2$ (prototype $TiSi_2$)

6. The side face centred orthorhombic-2 titanium disilicide with twelve atoms per unit cell (oS12)$TiSi_2$ (prototype $ZrSi_2$)
7. The orthorhombic primitive with eight atoms per unit cell (oP8)TiSi

   (prototype FeB-b)
8. The tetragonal primitive (tP36)Ti_5Si_4 (prototype Si_4Zr_5) with thirty-six atoms per unit cell
9. The hexagonal close packed (hcp) with sixteen atoms per unit cell (hP16) Ti_5Si_3 (prototype Mn_5Si_3)
10. The face centred cubic (fcc) with eight atoms per unit cell (cF8)(Si) (prototype C)

The crystal structures and phase transformations in the Si–Ti phase diagram are given in Tables 1.5 and 1.6. The Ti_3Si is stable below 1167 °C while the Nb_3Si is stable above 1700 °C. Ti_3Si is in thermodynamic equilibrium with (Ti) at < 1167 °C whereas the αNb_5Si_3 and Nb_{ss} are in equilibrium at < 1700 °C. The Nb_3Si form from peritectic reaction L + $\beta Nb_5Si_3 \rightarrow Nb_3Si$ at about 1980 °C and the eutectic reaction L $\rightarrow Nb_{ss}$ + Nb_3Si at about 1880 °C while Ti_3Si is formed from peritectoid reaction Ti_5Si_3 + (Ti) ht $\rightarrow Ti_3Si$ at about 1167 °C. The Ti_3Si (tP32) is isomorphous with the Nb_3Si (tP32) (see Tables 1.2 and 1.5) and hence Ti addition to Nb-Si binary alloys could stabilise the Nb_3Si to lower temperatures as the Ti_3Si is stable to room temperature. Ti addition could also destabilise the (tI32) Nb_5Si_3 since the Ti_5Si_3 (hP16) is non-isomorphous with the former. Thus, the solubility of Ti in Nb_5Si_3 is very important because of the potential to change the structure of the (tI32) Nb_5Si_3 from tetragonal βNb_5Si_3 to hexagonal γNb_5Si_3. The melting temperature of Ti_5Si_3 is lower than that of βNb_5Si_3 and thus the former is expected to have inferior creep resistance than the latter. It should be noted that the metastable γNb_5Si_3 (see Table 1.4) that is stabilised by interstitials is isomorphous with the Ti_5Si_3.

Table 1.5 Crystal structures of phases present in the Si–Ti system. Data from (Seifert et al., 1996)

Phase	Composition at% Ti	Pearson symbol	Prototype	Lattice parameters (Å)		
				a	b	c
(Ti) rt	99.5 – 100	hP2	Mg	2.9512		4.6845
(Ti) ht	95 – 100	cI2	W	3.3066		
(Si)	0	cF8	C (diamond)	5.4309		
TiSi	50	oP8	FeB-b	6.5383	3.6413	5.002
$TiSi_2$	33.3	oF24	$TiSi_2$	8.2671	4.800	8.5505
$TiSi_2$	33.3	oS12	$ZrSi_2$	3.61	13.77	3.65
Ti_3Si	75	tP32	Ti_3P	10.39		5.17
Ti_5Si_3	60.5 – 64.5	hP16	Mn_5Si_3	7.4610		5.1508
Ti_5Si_4	55.6	tP36	Si_4Zr_5	6.702		12.174

Table 1.6 Reactions in the Si – Ti system. Data from (Seifert et al., 1996)

Reaction	Phase composition (at%Ti)			Tempera-ture (˚C)	Reaction type
	A	B	C		
$L \rightarrow (Si) + TiSi_2$	16	0	33.3	1330	Eutectic
$L \rightarrow TiSi_2$		33.3		1490	Congruent
$L \rightarrow TiSi_2 + TiSi$	36	33.3	50	1480	Eutectic
$L + Ti_5Si_4 \rightarrow TiSi$	40	55.6	50	1568	Peritectic
$L + Ti_5Si_3 \rightarrow Ti_5Si_4$	52	60.5	55.6	1920	Peritectic
$L \rightarrow Ti_5Si_3$		62.5		2122	Congruent
$L \rightarrow Ti_5Si_3 + (Ti)$ ht	86.5	64.5	95	1340	Eutectic
$Ti_5Si_3 + (Ti)$ ht $\rightarrow Ti_3Si$	64.5	96	75	1170	Peritectoid
(Ti) ht $\rightarrow Ti_3Si + (Ti)$ rt	99	75	99.5	865	Eutectoid
$L \rightarrow$ (Ti) ht		100		1670	Freezing
(Ti) ht $\rightarrow$ (Ti) rt		100		882	polymorphic
$L \rightarrow$ (Si)		0		1414	Freezing

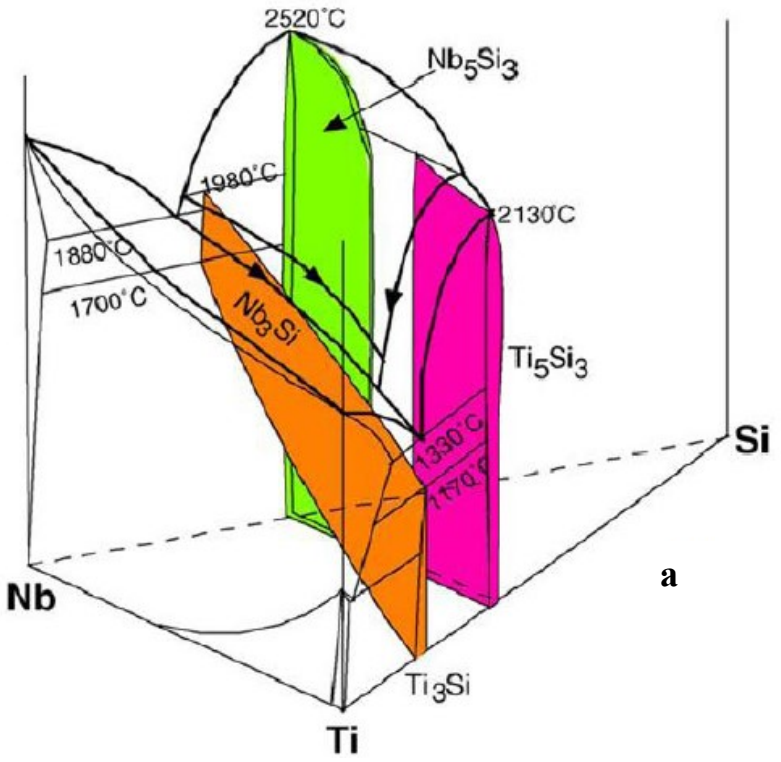

b Part of the Figure 1.5 was removed.

Figure 1.5 The metal-rich corner of the Nb-Si-Ti system (a) 3D- phase diagram and (b) Liquidus projection (Zhao et al., 2004c, Bewlay et al., 1997). Note that reaction temperatures for the Nb-Si and Si-Ti binaries are different from those in Figures 1.1, 1.2 and 1.4.

1.1.4 The Nb-Si-Ti system

The ternary Nb-Si-Ti is of great importance for the design and processing of Nb Silicide based alloys given the importance of alloying Nb with Si and Ti. Phase equilibria for this system are shown in Figure1.5. This gives a 3D- phase diagram and liquidus projection of the metal rich corner of the Nb-Si-Ti system. There are two transition reactions: L + $Nb(Ti)_5Si_3$ → $(Nb,Ti)_3Si$ + $Ti(Nb)_5Si_3$ at 1600 °C to 1650 °C and L + $(Nb,Ti)_3Si$ → (Nb,Ti,Si) + $Ti(Nb)_5Si_3$ at ~1350 °C denoted by u_1 and u_2 respectively in Figure 1.5b. $Nb(Ti)_5Si_3$ and $Ti(Nb)_5Si_3$ stand for the Nb- and the Ti-based 5-3 silicides where Nb is substituted by Ti in the former and vice versa. The p1

in the Figure 1.5b stands for the peritectic reaction L + $Nb(Ti)_5Si_3 \rightarrow Ti(Nb)_5Si_3$. The Figure 1.5 also shows some degree of solubility of Ti and Nb in both 5-3 silicides. Titanium addition lowers the eutectic temperatures, from 1880 °C to 1330 °C, and therefore the liquidus of these alloys. Titanium contents of these alloys should be < 25 at% to keep eutectic temperature above 1700 °C and prevent the formation of the undesirable hexagonal Ti_5Si_3 phase which is detrimental to creep (Bewlay et al., 2002).

1.1.5 The Cr-Nb system

Chromium tends to be a desirable element in alloys used at high temperatures because it can benefit oxidation behaviour due to the formation of Cr_2O_3, which is one of the three desirable and stable oxides, the other two being the SiO_2 and Al_2O_3.

The Cr-Nb phase diagram is shown in Figure 1.6 and the crystal structure of phases and reactions in this system are given in Tables 1.7 and 1.8. The high temperature $NbCr_2$ (ht) C14 Laves is unstable below 1570 °C. Stabilisation of the latter to lower temperature is desirable for high temperature applications due to its high melting point. It can be seen that alloying with Cr decreases the melting temperature of Nb and since Ti has a similar effect (Figure 1.3) it is important to consider the effect of both elements on the liquidus of the alloys. Zelenitsas and Tsakiropoulos reported liquation when the alloys Nb-24Ti-18Si-8Cr-4Al and Nb-24Ti-6Ta-18Si-8Cr-4Al were heat treated at 1500 °C for 100 h but not in Nb-24Ti-18Si-5Cr-4Al and Nb-24Ti-6Ta-18Si-5Cr-4Al after similar heat treatment (Zelenitsas and Tsakiropoulos, 2006b).

Furthermore, the Laves phase has good oxidation resistance and thus it can be desirable when designing alloys for improved oxidation behavior. However, the Laves forms a eutectic with Nb denoted by (Nb) in Figure 1.6 at 1650 °C, in other words aiming for Laves in the microstructure has implications for the liquidus of the alloy.

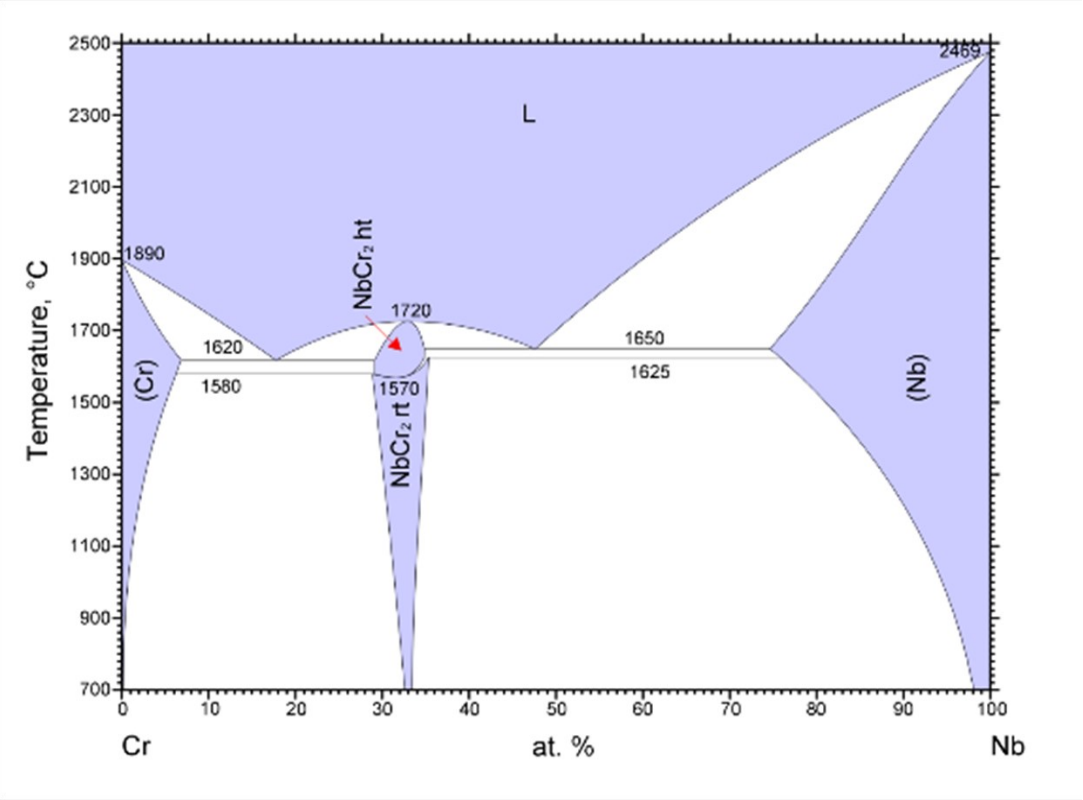

Figure 1.6 The Cr-Nb system (Neto et al., 1993). Note that some of the reaction temperatures are different from those given in Table 1.8. Reprinted with permission of ASM International.

Table 1.7 The crystal structure of phases present in the Cr-Nb system. Data from (Neto et al., 1993)

Phase	**Composition (at% Nb)**	**Pearson symbol**	**Prototype**	**Lattice parameters (Å)**	
				a	**c**
(Cr)	0-5.6	cI2	W	2.891	
$NbCr_2$ (ht)	30.5-38	hP12	$MgZn_2$	4.931	8.123
$NbCr_2$ (rt)	31.5-39.5	cF24	$MgCu_2$	6.991	
(Nb)	75.6-100	cI2	W	3.262	

1.1.6 The Cr-Si system

Alloying Nb-Si based alloys with Cr opens up the possibility of forming Cr-Si phases in addition to Nb-Cr ones as discussed in the previous section and thus the Cr-Si phase equilibria is very important. The Cr-Si phase diagram (Figure 1.7) has the following stable phases:

1. The Liquid (L)
2. The terminal body centred cubic (bcc) Cr solid solution with two atoms per unit cell (cI2) (Cr) (prototype W)
3. The cubic primitive chromium 3-1 silicide with eight atoms per unit cell (cP8) Cr_3Si) (prototype Cr_3Si)
4. The high temperature (ht) Cr_5Si_3 (no crystal structure information)
5. The room temperature (rt) body centred tetragonal alpha Cr 5-3 silicide with thirty-two atoms per unit cell (tI32) Cr_5Si_3 (αCr_5Si_3) (prototype W_5Si_3)
6. The cubic primitive CrSi with eight atoms per unit cell (cP8) CrSi (prototype FeSi)
7. The hexagonal close packed (hcp) Cr disilicide containing nine atoms per unit cell (hP9) $CrSi_2$ (prototype $CrSi_2$)
8. The terminal face centred cubic (fcc) silicon with eight atoms per unit cell (cF8) (Si) (prototype C)

It should be noted that other phase diagram give only the tI32 (W_5Si_3) crystal structure for Cr_5Si_3 (Tsakiropoulos, 2014).

The crystal structure data, phases and reactions in the Cr-Si system are given in Tables 1.9 and 1. 10. Chromium has negligible solubility in Si while up to 11.7 at % Si could dissolve in Cr at the eutectic temperature of 1680 °C. The αCr_5Si_3 is isomorphous with the βNb_5Si_3, thus addition of Cr to Nb-Si based alloys could stabilise the βNb_5Si_3 to room temperature and reduce the melting point of the 5-3 silicide. However, the Cr_3Si is not isomorphous with tP32 Nb_3Si and thus would be expected to destabilise the latter.

Table 1.8 Reactions in the Cr-Nb system. Data from (Neto et al., 1993).

Reaction	**Composition (at%Nb)**			**Tempera-ture (°C)**	**Reaction type**
	A	**B**	**C**		
L → (Cr)+$NbCr_2$ (ht)	18.5	5.6	30.8	1668	Eutectic
L → $NbCr_2$ (ht)		33.5		1730	Congruent
$NbCr_2$ (ht)→(Cr)+$NbCr_2$ (rt)	30.5	4.5	31.5	1585	Eutectoid
$NbCr_2$ (ht)+ (Nb)→NbCr2 (rt)	38	79	39.5	1625	Peritectoid
L→ $NbCr_2$ (ht)+ (Nb)	49.5	38.2	75.6	1703	Eutectic
L→ (Cr)				1863	Freezing
L→ (Nb)	100	100		2469	Freezing

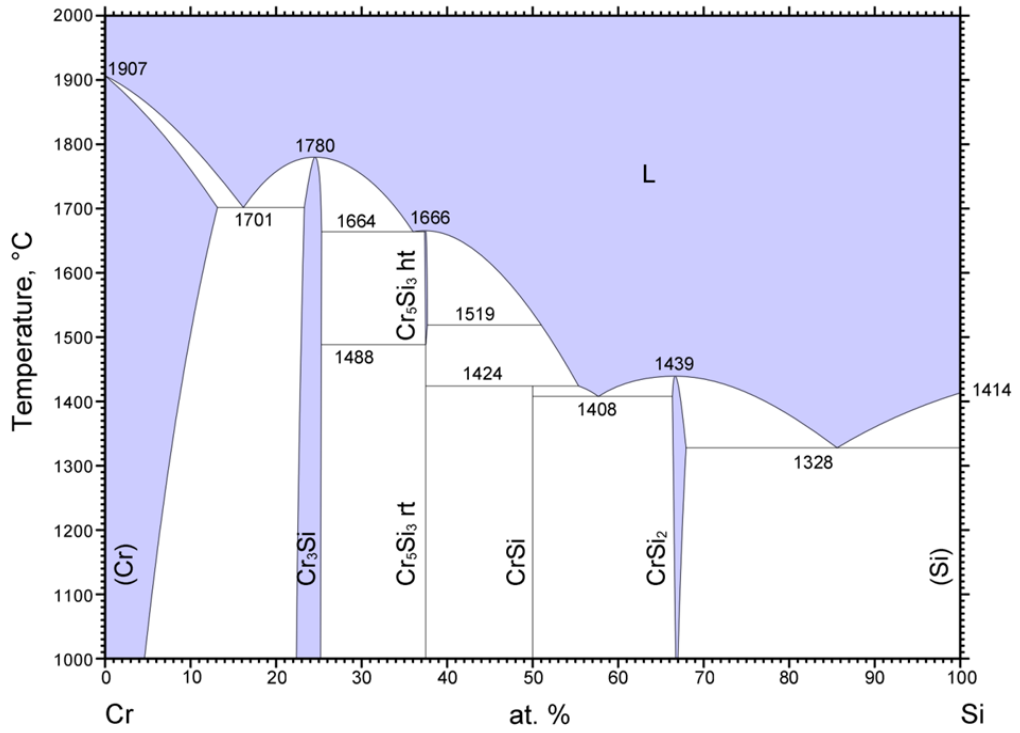

Figure 1.7 The Cr-Si system (Okamoto, 2001). Note that the reaction temperatures are different from those given in Table 1.10. Reprinted with permission of ASM International.

Table 1.9 The crystal structure of phases present in the Cr-Si system. Data taken from (Okamoto, 2001)

Phase	Composition (at %Si)	Pearson symbol	prototype	Lattice parameters (Å)	
				a	c
(Cr)	0-11.7	cI2	W	2.88	
Cr_3Si	23.5-27.5	cP8	Cr_3Si	4.556	
Cr_5Si_3 rt	37.5	tI32	W_5Si_3	9.17	4.636
CrSi	50	cP8	FeSi	4.62	
$CrSi_2$	65.7-66.7	hP9	$CrSi_2$	4.422	6.351
(Si)	100	cF8	C	5.4324	

Table 1.10 Reactions in the Cr-Si system. Data taken from (Okamoto, 2001)

Reaction	Composition (at%Si)			Tempera-ture (°C)	Reaction type
	A	B	C		
$L \rightarrow (Cr) + Cr_3Si$	16	11.7	23.5	1680	Eutectic
$L \rightarrow Cr_3Si$		25.5		1770	Congruent
$L \rightarrow Cr_3Si + Cr_5Si_3$	36.5	27.5	37.5	1675	Eutectic
$L \rightarrow Cr_5Si_3$		37.5		1680	Congruent
$L + Cr_5Si_3 \rightarrow CrSi$	55	37.5	50	1440	Peritectic
$L \rightarrow CrSi + CrSi_2$	57	50	65.7	1435	Eutectic
$L \rightarrow CrSi_2$		66.7		1465	Congruent
$L \rightarrow CrSi_2 + (Si)$	87	67.5	100	1335	Eutectic
$L \rightarrow (Cr)$				1863	Freezing
$L \rightarrow (Si)$	100	100		1414	Freezing

1.1.7 The Nb-Cr-Si system

This is a very important system giving the important role that Cr and Si play in mechanical and environmental properties of Nb silicide based alloys. The Nb-Cr-Si system (Figure 1.8) is one of the most studied ternary phase diagrams (Zhao et al., 2003), because there is disagreement over the stability of phases (Bewlay et al., 2009). Even though the work of Zhao et al. agrees with the thermodynamic calculation of the Nb-Cr-Si by Shao (Shao, 2005), there is still disagreement over the existence of Nb_{ss} + Nb_5Si_3 + C14($NbCr_2$) or Nb_{ss} + Nb_5Si_3 + CrNbSi three phase equilibria. The first phase equilibria studies of the Nb-Cr-Si system by Goldschmidt and Brand (Goldschmidt and Brand, 1961b) gives the former; Zhao et al. suggested the latter. The thermodynamic calculation of Shao (2005) suggested the former, which was also supported by the work of Geng et al. (Geng et al., 2006b) who identified the Nb_{ss} + Nb_5Si_3 + C14($NbCr_2$) three phase equilibria experimentally.

Bewlay et al. (2009) sought to produce a liquidus surface of the metal-rich end of the Nb-Cr-Si system. Experimentally they reported the existence of new ternary eutectic comprising the Nb_{ss} + $Nb_9(Cr,Si)_5$ + C14($NbCr_2$) phases and proposed new phase equilibria for the Nb-Cr-Si system (Figure 1.8)(Bewlay et al., 2009). No other worker has confirmed the phase equilibria reported by Bewlay et al. It is also important to note that all the workers reported stabilisation of C14 $NbCr_2$ Laves by Si to at least 1000 °C.

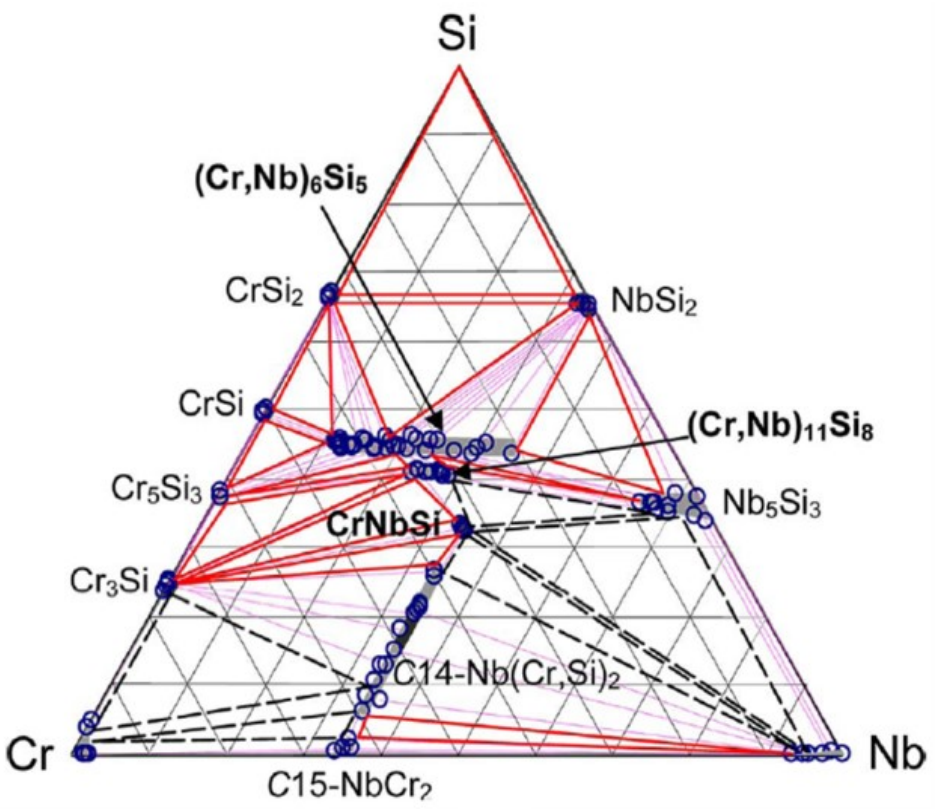

a

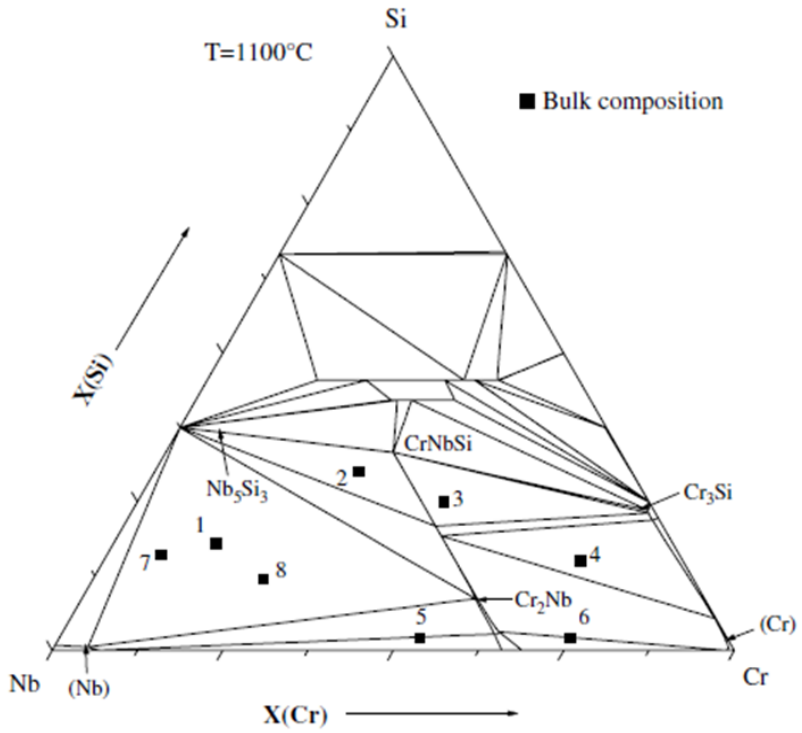

b

Figure 1.8 continues on next page.

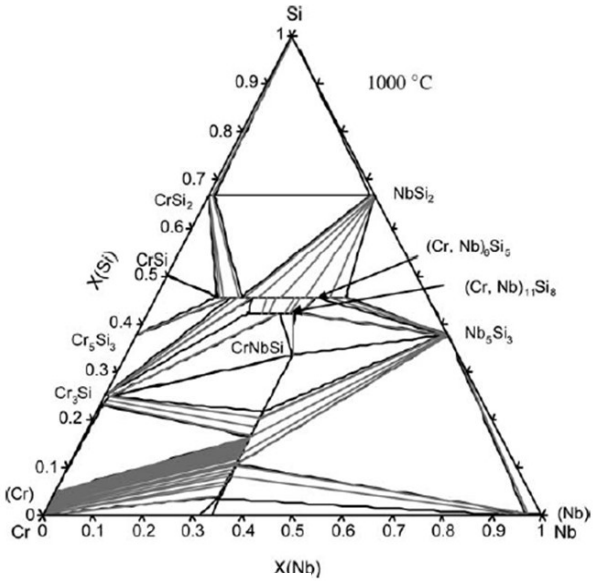

c

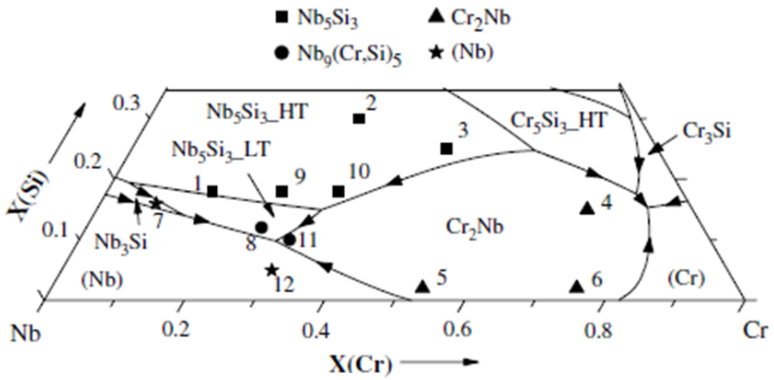

d

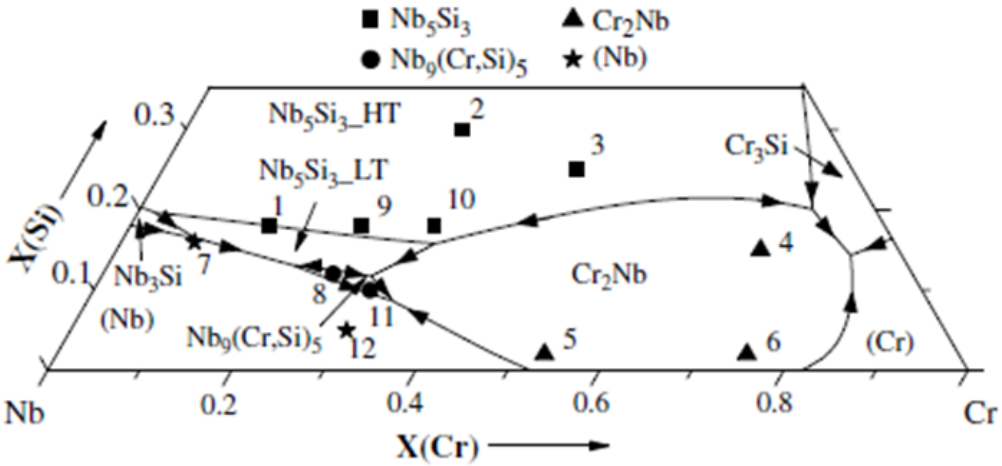

e

Figure 1.8 The Nb-Cr-Si system (a) Zhao et al. (2003) 1000 °C isotherm; (b) Bewlay et al. (2009) 1100 °C isotherm; (c) Shao (2005) 1000 °C isotherm; (d) liquidus projection and (e) proposed new liquidus projection both (d) and (e) by Bewlay et al. (2009).

1.1.8 The Nb-Al-Cr system

Like the Nb-Cr-Si system, this ternary system is very important for the design of Nb silicide based alloys giving the importance of Al_2O_3 and Cr_2O_3 formation for oxidation resistance, the effect of Al and Cr on DBTT (see section 1.3.1) and on the toughness of the Nb_{ss}. Isothermal sections for 1000 °C are given in Figure 1.9. There is agreement that the synergy of Al and Cr stabilises the C14 Laves phase.

The Nb-Cr rich ends of four Nb-Al-Cr 1000 °C isothermal sections in Figure 1.9 are in agreement in terms of number of stable phases but differ in the positions of phase boundaries. The latter was attributed to the use of different experimental methods. No ternary compounds have been reported in the Nb-Al-Cr ternary. Note that the experimentally determined isothermal sections do not show the C14 Laves phase to be in equilibrium with the A15 Nb_3Al but the assessment by He et al. reported in (Raghavan, 2011).

1.1.9 The Nb-Al-Si system

Figures 1.10 and 1.11 show the experimentally determined and calculated isothermal sections of the Nb-Al-Si system respectively. The ternary compounds $Nb_{10}Si_3Al_3$ and $Nb_3Si_5Al_2$ (C54) have been reported to form in the Nb-Al-Si system. The latter is stable down to temperatures below 1000 °C, but the former is not. The crystal structure data of the ternary compounds in the Nb-Al-Si system is given in Table 1.11.

1.1.10 The Cr-Ti system

Chromium and titanium are important alloying elements in Nb silicide based alloys owing to their effect on the alloy liquidus (Zelenitsas and Tsakiropoulos, 2006b), but also because they can form Laves phase. The Cr-Ti binary phase diagram is shown in Figure 1.12.

Figure 1.9 continues on next page. Removed.

Figure 1.9 The Nb-Al-Cr 1000 °C isothermal sections (a) proposed by Hunt and Raman (1968), (b) proposed by Mahdouk and Gachon (2001), (c) proposed by Zhao et al. (2004b) and (d) thermodynamic assessment by He et al. (2010). Note (a to c) in (Zhao et al., 2004b) and (d) in (Raghavan, 2011). Removed

Figure 1.10 Reported experimental isothermal sections of Nb-Al-Si as given by Shao (2004) (a) 1400 °C (upper part), 500 °C (lower part), (b) 1400 °C, (c) 1200-1600 °C and (d) 1000 °C . Removed

Table 1.11 Crystal structures of ternary phases in the Nb-Al-Si system. Data from (Shao, 2004).

Phase	**Pearson symbol**	**Prototype**	**Lattice parameters (Å)**		
			a	**b**	**c**
$Nb_3Si_5Al_2$	oF24	$TiSi_2$	8.403	4.901	8.794
$Nb_{10}Si_3Al_3$	tI32	W_5Si_3	10.16	-	5.08

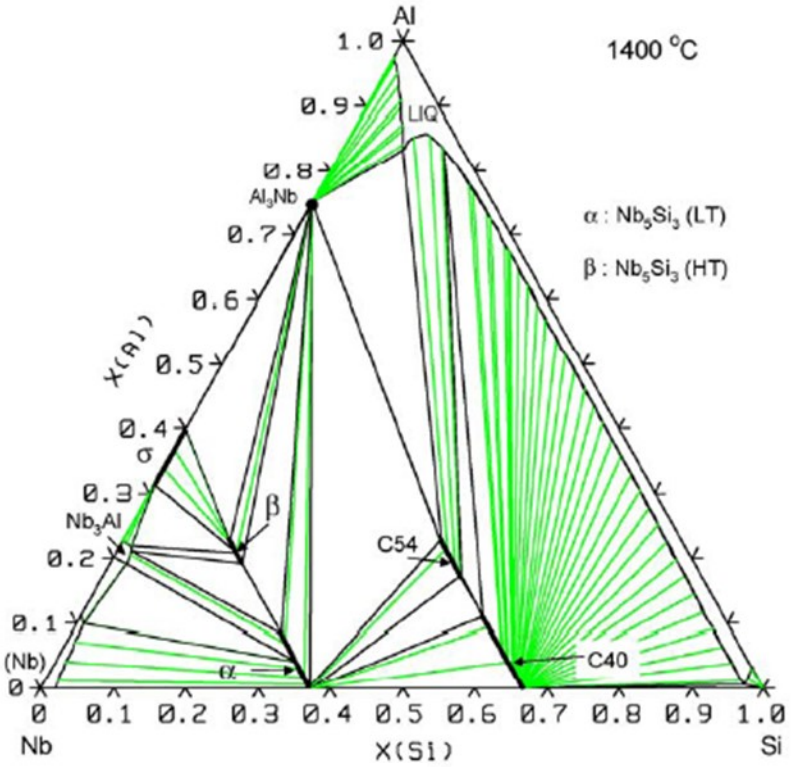

a

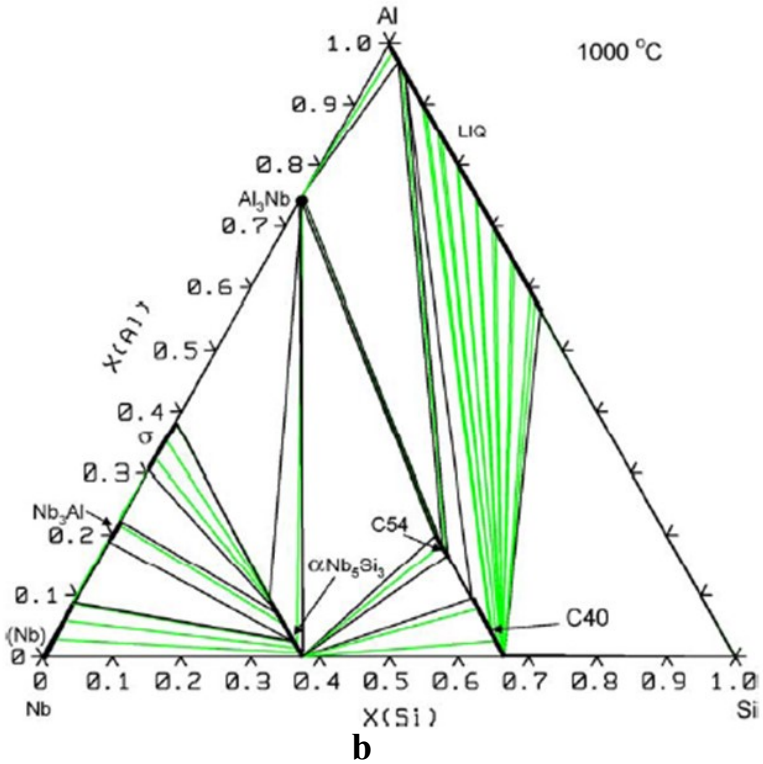

b

Figure 1.11 Calculated isothermal sections of the Nb-Al-Si system (a) 1400 °C and (b) 1000 °C (Shao, 2004).

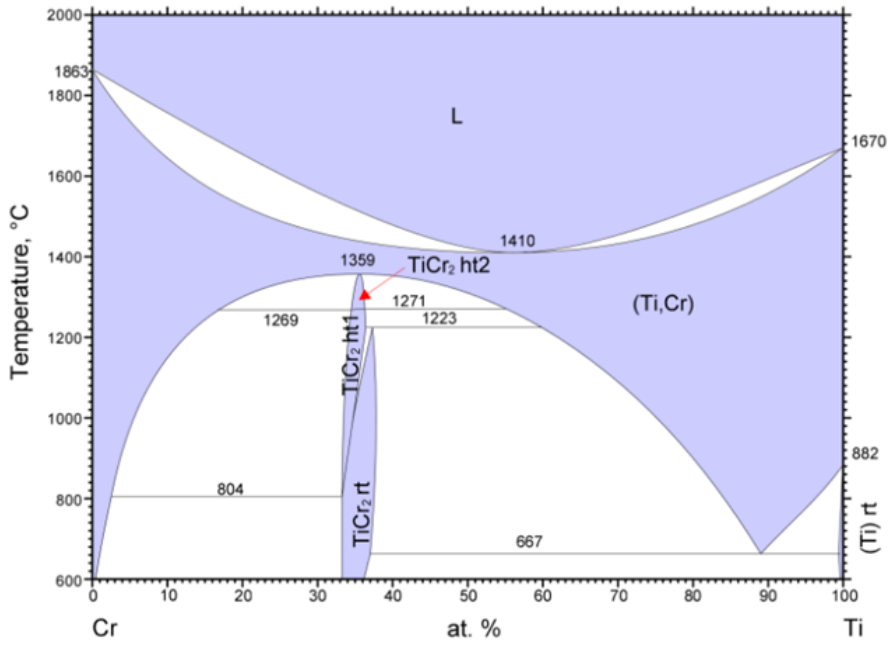

Figure 1.12 The Cr-Ti system (Okamoto, 2002). Note that reaction temperatures are different from those given in Table 1.13. Reprinted with permission of ASM International.

The stable phases in the Cr-Ti system are:

1. The body centred cubic (bcc) beta titanium-chromium solid solution with two atoms per unit cell cI2 (βTi,Cr) (prototype W) denoted by (Ti,Cr) in Figure 1.12
2. The high temperature (ht) hexagonal close packed (hcp) Cr_2Ti Laves phase with twenty-four atoms per unit cell hP24 Cr_2Ti (prototype $MgNi_2$) denoted by $TiCr_2$ ht2
3. The high temperature (ht) hexagonal close packed (hcp) Cr_2Ti Laves phase with twelve atoms per unit cell hP12 Cr_2Ti (prototype $MgZn_2$) denoted by $TiCr_2$ ht1
4. The room temperature (rt) face centred cubic Cr_2Ti Laves phase with twenty-four atoms per unit cell cF24 Cr_2Ti (prototype Cu_2Mg) denoted by $TiCr_2$ rt
5. The room temperature (rt) hexagonal close packed (hcp) α-Ti solid solution with two atoms per unit cell hP2 αTi (prototype Mg) denoted by (Ti) rt.

The crystal structure of phases and reactions in the Cr-Ti phase diagram are given in Tables 1.12 and 1.13. The $TiCr_2$ ht1 (800 °C – 1270 °C) is isomorphous with the $NbCr_2$ C14 Laves (1570 – 1720 °C) while the $TiCr_2$ rt (≤ 1220 °C) is isomorphous with the $NbCr_2$ C15 Laves (≤ 1625 °C). Thus alloying with Ti could stabilise C14 Laves phase to lower temperatures.

Table 1.12 The crystal structure of phases in the Cr-Ti system Data from (Okamoto, 2002)

Phase	**Composition (at%Ti)**	**Pearson symbol**	**Prototype**	**Lattice parameters (Å)**	
				a	**c**
(Ti,Cr)	0-100	cI2	W	2.932	
$TiCr_2$ ht1	33-36	hP12	$MgZn_2$	4.932	8.005
$TiCr_2$ ht2	33-36	hP24	$MgNi_2$	4.932	16.01
$TiCr_2$ rt	33-37	cF24	Cu_2Mg	6.939	
(Ti) rt	99.8-100	hP2	Mg	2.9486	4.67

Table 1.13 Reactions in the Cr-Ti system. Data from (Okamoto, 2002)

Reaction	**Composition (at% Ti)**			**Tempera-ture (°C)**	**Reaction type**
	A	**B**	**C**		
L → (Ti,Cr)		56		1040	
(Ti,Cr) → $TiCr_2$ ht2		33.3		1370	
$TiCr_2$ ht2 → $TiCr_2$ ht1		33.3-36		1270	Polymorphic
$TiCr_2$ ht1 → (Ti, Cr) + $TiCr_2$ rt	33.3	4	35	800	Eutectoid
$TiCr_2$ ht1→(Ti, Cr)+$TiCr_2$ rt	36	60	37	1220	Peritectoid
(Ti,Cr)→$TiCr_2$ rt+(Ti) rt	37.5	37	100	667	Eutectoid

1.1.11 The Cr-Nb-Ti system

The Cr-Nb-Ti phase diagram (Figure 1.13) has no ternary compounds. The 1150 °C isotherm shows complete solid solubility between the C15 ($TiCr_2$ rt and $NbCr_2$ rt) phases and that the solubility of Cr in the Nb based solid solution increases with Ti.

1.1.12 The Cr-Nb-Mo system

The Nb-Mo phase diagram shows a continuous solid solubility (Okamoto, 1991) and the Cr-Mo phase diagram has continuous body centre cube chromium-molybdenum solid solution, with two atoms per unit cell cI2 (Cr, Mo) (prototype W). At temperatures below 940 °C, a miscibility gap opens out (Cr, Mo) → $(Cr, Mo)_1$ + $(Cr, Mo)_2$ where subscript 1 and 2 means Cr- and Mo-rich solid solutions (Turchi et al., 2006).

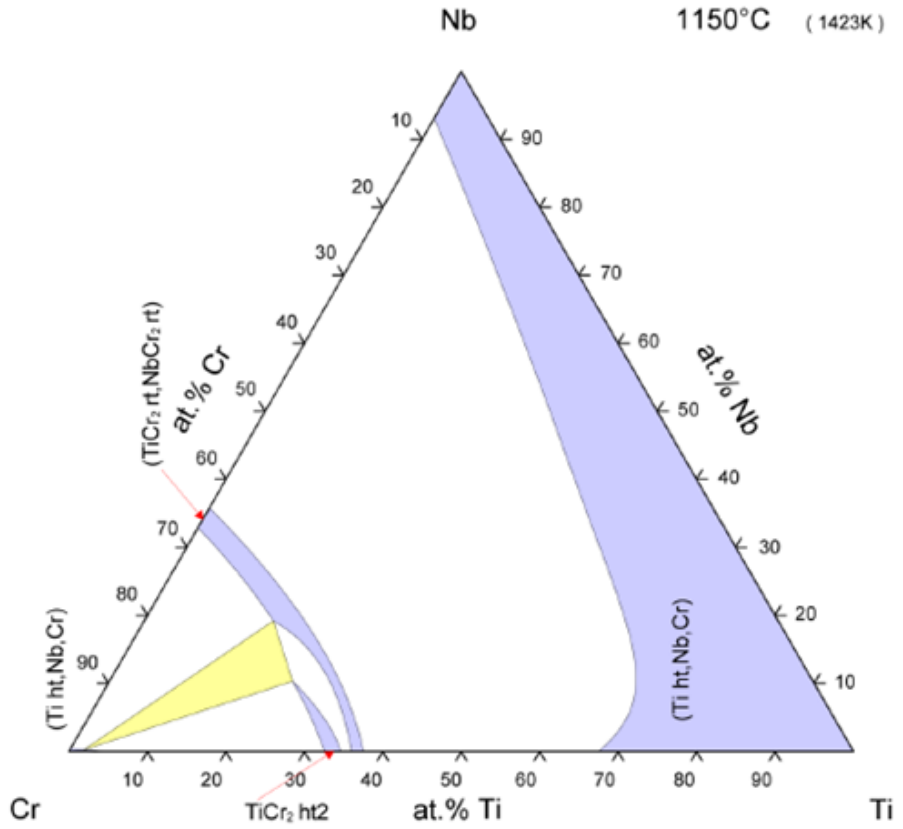

Figure 1.13 The 1150 °C isothermal section of the Cr-Nb-Ti system (Zhao et al., 2004a). Reprinted with permission of ASM International.

The Cr-Nb-Mo 1000 °C isotherm (Figure 1.14) consists of a single phase (α) Mo (the α_1 is Cr-rich while α_2 is Nb-rich) phase field and a miscibility gap region. The latter is further partitioned into $\alpha_1 + \alpha_2$, $\alpha_1 + \alpha_2 + \rho$, $\alpha_1 + \rho$, ρ and $\alpha_2 + \rho$ phase fields. According to Goldschmidt and Brand (1961a), miscibility gap $\alpha \rightleftharpoons \alpha_1 + \alpha_2$ or $\alpha \rightleftharpoons \alpha_1 + \alpha_2 + \rho$ or $\alpha \rightleftharpoons \alpha_2 + \rho$ open out at temperatures ≤ 1000 °C and closes at > 1000 °C.

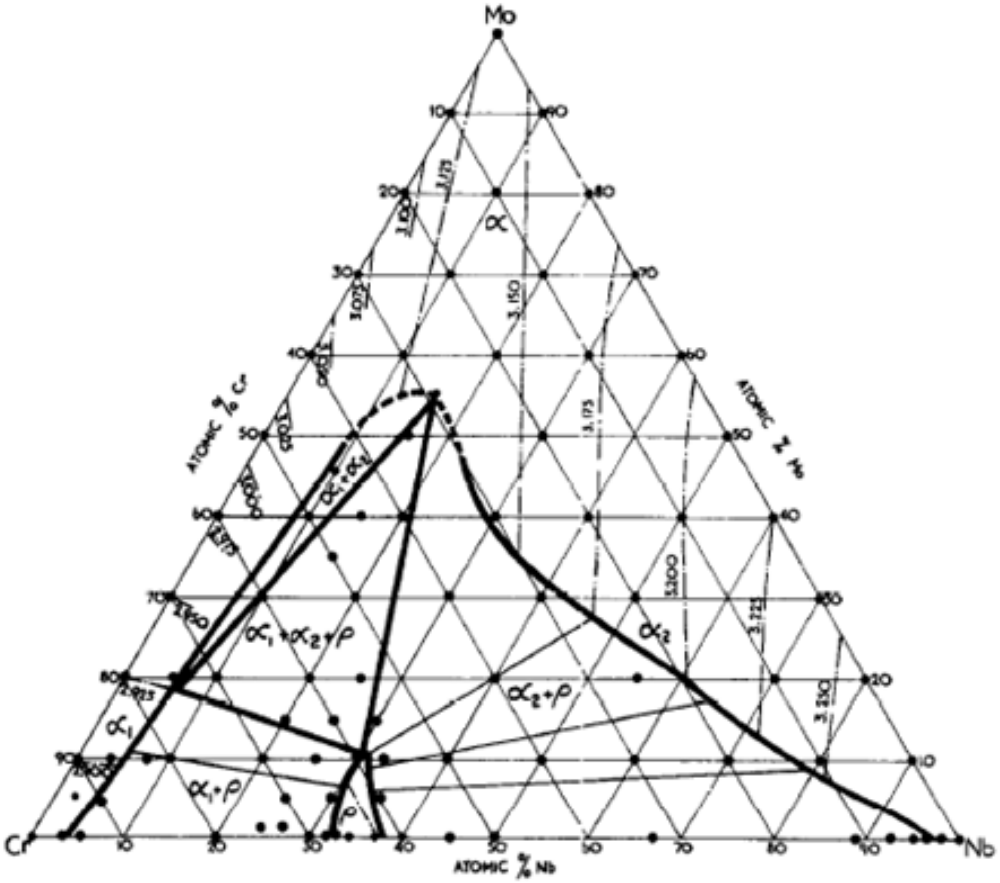

Figure 1.14 The Cr-Nb-Mo 1000 °C isotherm (Goldschmidt and Brand, 1961a)

1.1.13 The Mo – Si system

Alloying with Mo enhances the high temperature strength of the $(Nb, Mo)_{ss}$. However, Mo like Nb can form silicides and thus the Mo-Si phase equilibria are important for the design of Nb silicide alloys. The Mo – Si phase diagram (Figure 1.15) has the following stable phases:

1. The Liquid (L)

2. The body centred cubic (bcc) molybdenum solid solution with two atoms per unit cell cI2 (Mo) (prototype W)
3. The cubic primitive with eight atoms per unit cell (cP8) Mo_3Si (prototype Cr_3Si)
4. The body centred tetragonal with thirty-two atoms per unit cell (tI32)Mo_5Si_3 (prototype W_5Si_3)
5. The high temperature (ht) hexagonal close packed (hcp) with nine atoms per unit cell (hP9) β$MoSi_2$ (prototype $CrSi_2$) denoted by $MoSi_2$ ht
6. The room temperature (rt) body centred tetragonal with six atoms per unit cell (tI6) α$MoSi_2$ (prototype $MoSi_2$) denoted by $MoSi_2$ rt
7. The face centred cubic (fcc) silicon solid solution with eight atoms per unit cell (cF8) (Si) (prototype C)

More recent research has indicated that there is only one $MoSi_2$ stable phase with the tI6 structure (Tsakiropoulos, 2014).

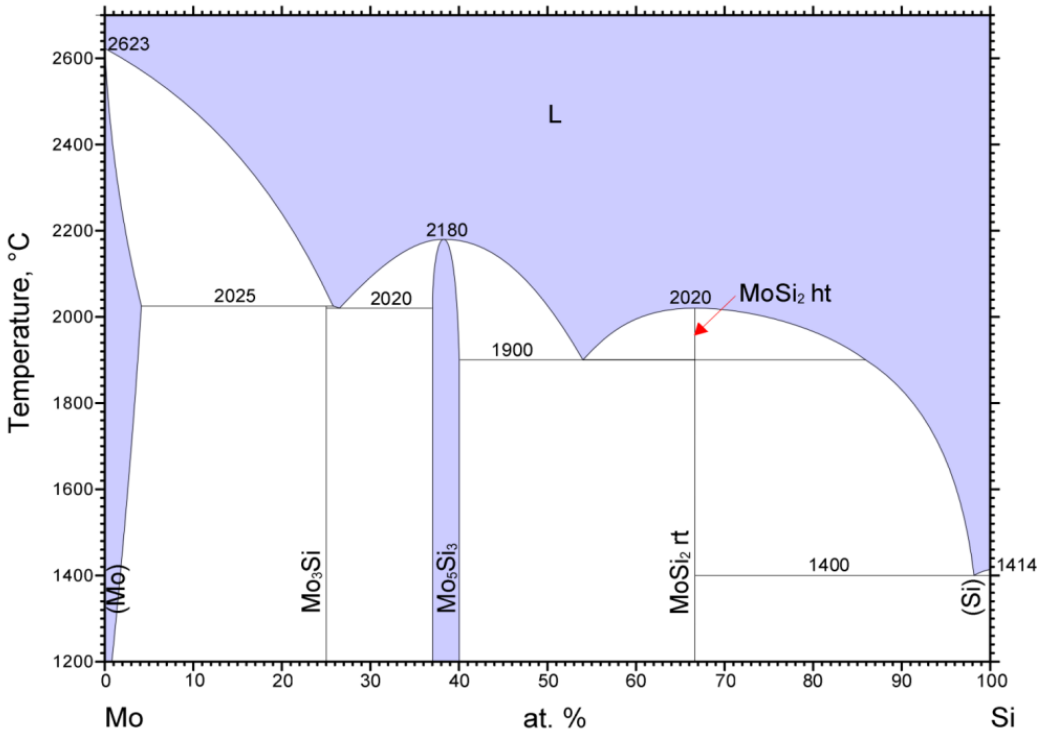

Figure 1.15 The Mo-Si system (Gokhale and Abbaschian, 1990). Reprinted with permission of ASM International.

Unlike the Nb-Si system, the (tI32) Mo_5Si_3 does not exist in equilibrium with the terminal molybdenum solid solution (Mo). The crystal structures of the phases and the reaction data for the Mo –Si phase diagram in Figure 1.15 are given in Tables 1.14 and 1.15.

Table 1.14 Crystal structure of phases present in the Mo – Si phase diagram. Data from (Gokhale and Abbaschian, 1990)

Phase	Composition (at%Si)	Pearson symbol	Prototype	Lattice parameters (Å)	
				a	c
(Mo)	0- 4	cI2	W	3.147	
Mo_3Si	25	cP8	Cr_3Si	4.897	
Mo_5Si_3	37-40	tI32	W_5Si_3	9.65	4.911
$MoSi_2$ ht	66.7	hP9	$CrSi_2$	4.614	6.414
($MoSi_2$) rt	66.7	tI6	$MoSi_2$	3.2112	7.8249
(Si)	100	cF8	C	5.4309	

Table 1.15 Reactions in the Mo – Si system. Data from (Gokhale and Abbaschian, 1990)

Reaction	Composition (at %Si)			Temperature (˚C)	Reaction type
	A	B	C		
L + (Mo) → Mo_3Si	25.72	4	25	2025	Peritectic
L → Mo_3Si +Mo_5Si_3	26.4	25	37	2020	Eutectic
L → Mo_5Si_3		38		2180	Congruent
L → Mo_5Si_3 + $MoSi_2$ ht	54	40	66.7	1900	Eutectic
L → $MoSi_2$ ht		66.7		2020	Congruent
$MoSi_2$ ht → $MoSi_2$ rt		66.7		1900	Polymorphic
L → $MoSi_2$ rt+ (Si)	98	66.7	100	1400	Eutectic
L → (Mo)		0		2623	Freezing
L → (Si)		100		1414	Freezing

1.1.14 The Nb-Mo-Si system

The liquidus projection (Figure 1.16) of the Nb-Mo-Si ternary has four zones: the β(Nb, Mo)$_5Si_3$ denoted by β silicide in Figure 1.16, Nb_{ss}, (Mo(Nb))$_3$Si and

$(Nb(Mo))_3Si$. The $\beta(Nb, Mo)_5Si_3$ and Nb_{ss} eutectic exists for Mo concentration > 3 at% to $\leq$ 40 at% (Ma et al., 2004, Ma et al., 2000). This means that $(Nb(Mo))_3Si$ and Nb_{ss} eutectic could be replaced by the $\beta(Nb, Mo)_5Si_3$ and Nb_{ss} eutectic.

Figure 1.16 The liquidus projection in the metal rich corner of Nb-Mo-Si (Ma et al., 2000), Removed.

1.1.15 The Si – W system

Like Mo, W is a strong solid solution strengthener of Nb and an important alloying addition for improving the high temperature strength of Nb. The Si – W phase diagram (Figure 1.17) has the following stable phases:

1. The Liquid (L)
2. The face centred cubic (fcc) solid solution with eight atoms per unit cell(cF8) (Si) (prototype C)
3. The body centred tetragonal with six atoms per unit cell (tI6) WSi_2 (prototype $MoSi_2$)
4. The body centred tetragonal with thirty-two atoms per unit cell (tI32) W_5Si_3 (prototype W_5Si_3)
5. The body centred cubic solid solution with two atoms per unit cell (cI2) (W) (prototype W)

Alloying W with Si depresses the liquidus of binary W-Si alloys drastically and like Cr and Mo the melting temperature of the 5-3 silicide is lower than that of the metal. This effect is the strongest for W as the ratio of the melting point of the 5-3 silicide to the metal increases from 0.67 for the case of W to 0.83 for Mo, to 0.87 for Cr compared with 1.02 for Nb. Ti is an exception with 1.27. The crystal structure of the phases and reactions in the Si – W system are given in Tables 1.16 and 1.17. The W_5Si_3 is isomorphous with βNb_5Si_3, therefore W would be expected to stabilise the latter to lower temperatures.

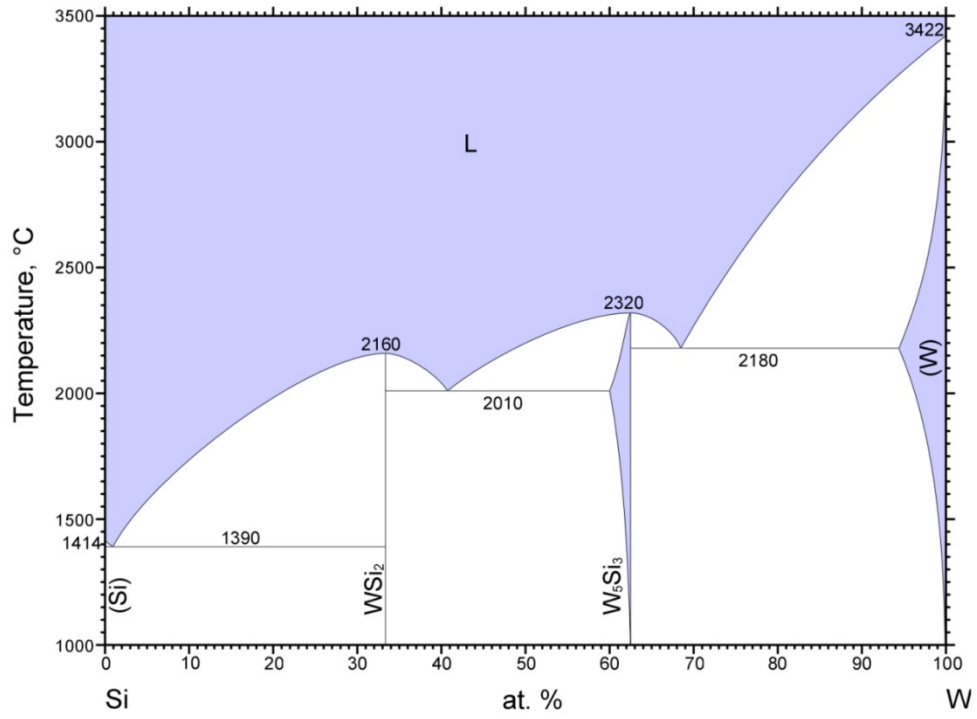

Figure 1.17 The Si-W system (Naidu et al., 1990b). Reprinted with permission of ASM International.

Table 1.16 crystal structure of phases in the Si – W system. Data from (Naidu et al., 1990b)

Phase	Composition (at% W)	Pearson symbol	Prototype	Lattice parameters(Å)	
				a	c
(Si)	0	cF8	C	5.4309	
WSi_2	33.2	tI6	$MoSi_2$	3.2178	7.8403
W_5Si_3	60-62.5	tI32	W_5Si_3	9.645	4.97
(W)	94.5-100	cI2	W	3.1649	

Table 1.17 Reactions in the Si – W system. Data from (Naidu et al., 1990b)

Reaction	Composition (at% W)			Temperature (˚C)	Reaction type
	A	B	C		
L → (Si) + WSi_2	1	0	33.3	1390	Eutectic
L → WSi_2		33.3		2160	Congruent
L → WSi_2 + W_5Si_3	40.7	33.3	60	2010	Eutectic
L → W_5Si_3		62.5		2320	Congruent
L → W_5Si_3 + (W)	68.5	62.5	94.5	2180	Eutectic
L → (Si)		0		1414	Freezing
L → (W)		100		3422	Freezing

1.1.16 The Nb–W–Si system

Like Nb-Mo, the Nb-W system shows continuous solid solubility (Naidu et al., 1990a). Unlike the Nb–Si and the Mo–Si systems there is eutectic reaction L → W_5Si_3 + W_{ss} at 2180 °C for 33.3at%Si. In the metal-rich end of the Nb–W–Si system, the liquidus projection in Figure 1.18 has three zones: Nb_{ss}, β(Nb, W)$_5Si_3$ denoted by β silicide, and (Nb, W)$_3$Si denoted by Nb(W)$_3$Si. The Figure 1.18 also shows that the Nb_{ss} and β(Nb, W)$_5Si_3$ eutectic exist in the Nb–W–Si ternary for W concentration > 3 at% as was the case in the Mo-Nb-Si system. Thus the 3-1 silicide and Nb_{ss} eutectic can be suppressed by increasing the W concentration in the Nb silicide based alloys.

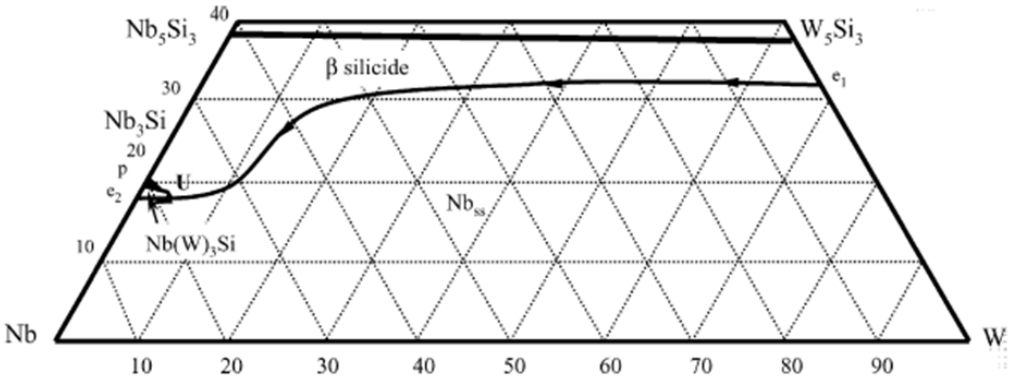

Figure 1.18 The liquidus projection in the metal rich corner of Nb-W-Si system (Ma et al., 2004).

1.1.17 The Nb – Sn system

Tin is an important alloying addition in Nb silicide based alloys as it improves their oxidation and suppresses pest oxidation (Geng and Tsakiropoulos, 2007). Pest oxidation is the rapid disintegration of refractory metals and some of their alloys into powder at intermediate temperatures (< 850 °C). Sn forms A15 Nb_3Sn phase which improves the hot strength of the alloys. Thus, the Nb-Sn phase equilibria is important for the development of Nb silicide based alloys with a balance of properties. The Nb – Sn phase diagram Figure 1.19 has the following stable phases:

1. The Liquid denoted by L in Figure 1.19
2. The body centred cubic (bcc) niobium solid solution with two atoms per unit (cI2) Nb_{ss} (prototype W) denoted by (Nb) in Figure 1.19
3. The high temperature (ht) cubic primitive with eight atoms per unit cell (cP8) Nb_3Sn (prototype Cr_3Si)
4. The high temperature (ht) body centred orthorhombic with forty-four atoms per unit cell (oI44) Nb_6Sn_5 (prototype Ti_6Sn_5)
5. The face centred orthorhombic with forty-eight atoms per unit cell (oF48) $NbSn_2$ (prototype Mg_2Cu)
6. The low temperature (lt) face centred cubic (fcc) alpha-tin solid solution containing eight atoms per unit cell (cF8) αSn_{ss} (prototype C-diamond) (denoted by (Sn) lt)
7. The room temperature (rt) body centred tetragonal with four atoms per unit cell (tI4) βSn_{ss} (denoted by (Sn) rt) (prototype Sn).

The crystal structures of phases and reactions in the Nb-Sn phase diagram are shown in Tables 1.18 and 1.19. It should be noted that the Nb_3Sn phase (A15-structure) is isomorphous with Nb_3Al, Cr_3Si and Mo_3Si and like those compounds is stable to room temperature. The Nb_3Sn forms via a peritectic reaction which means that it surrounds the Nb_{ss} in the solidified microstructure and therefore the vol% of the Nb_{ss} will be reduced as the peritectic reaction proceeds to completion.

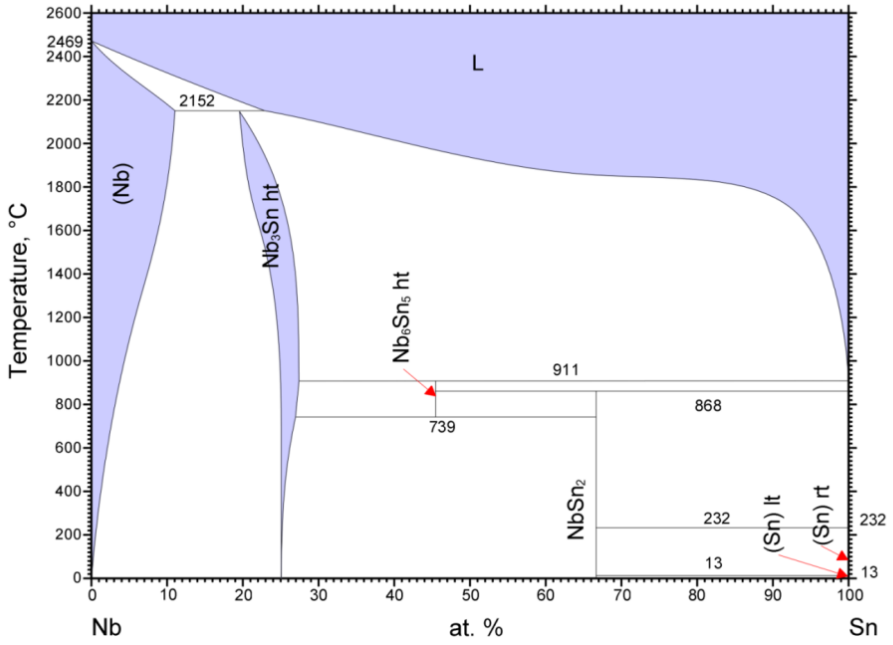

Figure 1.19 The Nb-Sn system (Okamoto, 2003). Note that some of the reaction temperatures and compositions are different from those given in Tables 1.18 and 1.19. Reprinted with permission of ASM International.

Table 1.18 The crystal structure and phases present in the Nb-Sn system. Data from (Okamoto, 2003)

Phase	Composition (at% Sn)	Pearson symbol	Prototype	Lattice parameters (Å)		
				a	b	c
(Nb)	0 -10	cI2	W	3.306		
Nb_3Sn ht	15.5-33.2	cP8	Cr_3Si	5.291		
Nb_6Sn_5 ht	45.5	oI44	Ti_6Sn_5	5.656	9.199	16.843
$NbSn_2$	66.7	oF48	Mg_2Cu	5.626	9.874	19.116
(Sn) lt (A4)	100	cF8	C	5.43		
(Sn) rt (A5)	100	tI4	Sn	5.8308		3.181

Table 1.19 Reactions in the Nb – Sn system. Data from (Okamoto, 2003)

Reaction	Composition (at% Sn)			Tempera-ture (˚C)	Reaction type
	A	B	C		
L + (Nb) → Nb_3Sn ht	25	10	15.5	2130	Peritectic
L + Nb_3Sn ht → Nb_6Sn_5 ht	100	33.2	45.5	916	Peritectic
Nb_6Sn_5 ht → Nb_3Sn + $NbSn_2$	45.5	25	66.7	739	Eutectoid
L + Nb_6Sn_5 ht → $NbSn_2$	100	45.5	66.7	830	Peritectic
L → $NbSn_2$ + (Sn) rt	100	66.7	100	231.9681	Eutectic
$NbSn_2$ + (Sn) rt + (Sn) lt	66.7	100	100	13	Unknown
L → (Nb)	0			2469	Freezing
L → (Sn) rt	100	100		232	Freezing
(Sn) rt → (Sn) lt	100	100		13	Polymorphic

1.1.18 The Nb-Si-Sn system

Isothermal sections of Nb-Sn rich corner of the Nb-Si-Sn ternary system are shown in Figure 1.20. The isothermal section has six phase regions namely Nb_{ss} denoted by (Nb), A15, (Nb) + αNb_5Si_3, A15 + (Nb), A15 + αNb_5Si_3 and A15 + (Nb) + αNb_5Si_3 for 1500 °C isotherm and additional ternary phase Nb_5SiSn_2 with W_5Si_3 structure for 900 °C and 1200 °C isotherms. The A15 is the Nb_3Sn. The liquidus projection of Nb-Si-Sn is shown in Figure 1.20d. In the Sn-rich end of the liquidus projection there is a miscibility gap which occupies the greater part of the liquidus surface. The invariant reactions are shown in Table 1.20 and four out of the five invariant reactions intersect the miscibility gap.

Table 1.20 Invariant reactions in the Nb-Si-Sn liquidus surface. Data from (Sun et al., 2012).

Calculated Temperature (°C)	Reactions
1974	L1 + βNb_5Si_3 → L2 + αNb_5Si_3
1874	L → (Nb) + A15 + αNb_5Si_3
1731	L1 → L2 + αNb_5Si_3 + A15
1664	L1 → L2 + $NbSi_2$ + βNb_5Si_3
1298	L1 → (Si) + L2 + $NbSi_2$

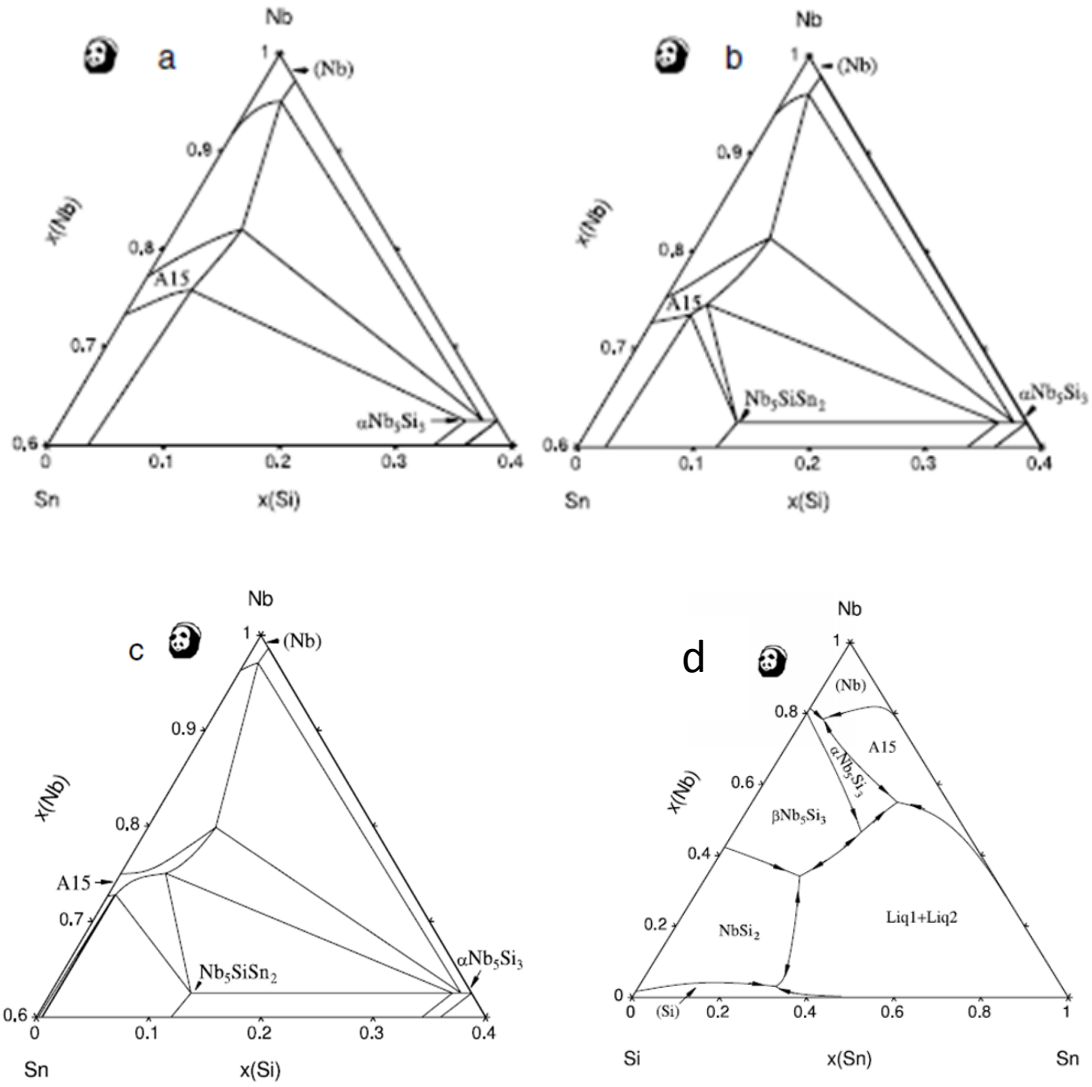

Figure 1.20 The Nb-Si-Sn system (a) 1500 °C isotherm, (b) 1200 °C, (c) 900 °C and (d) Liquidus projection, the A15 is Nb_3Sn (Sun et al., 2012).

1.1.19 The Nb-Ge system

Germanium, like tin, improves the oxidation behaviour and hot strength of Nb silicide based alloy (Zifu, 2012). Thus, the Nb-Ge phase equilibria is important for the design of Nb silicide based alloys. The Nb – Ge phase diagram according to Geng et al. (2011) (Figure 1.21) has the following stable phases:

1. The Liquid
2. The face centred cubic (fcc) germanium solid solution (cF8) Ge (denoted by (Ge) in Figure 1.21) (prototype C) with eight atoms per unit cell
3. The hexagonal close packed (hcp) with nine atoms per unit cell (hP9) $NbGe_2$ (prototype $CrSi_2$)
4. The hexagonal close packed (hcp) with sixteen atoms per unit cell (hP16) Nb_3Ge_2 (prototype Mn_5Si_3)
5. The body centred tetragonal with thirty-two atoms per unit cell (tI32)Nb_5Ge_3 (prototype W_5Si_3)
6. The cubic primitive with eight atoms per unit cell (cP8) Nb_3Ge (prototype Cr_3Si)
7. The body centred cubic (bcc) niobium solid solution containing two atoms per unit cell (cI2) Nb_{ss} (denoted by Bcc in Figure 1.21) (prototype W)

The Nb_5Ge_3 is isomorphous with βNb_5Si_3 and the Nb_3Ge is isomorphous with Nb_3Sn, Cr_3Si, Nb_3Al and Mo_3Si (A15- compounds). The crystal structure of phases and reactions in the Nb – Ge phase diagram are shown in Tables 1.21 and 1.22.

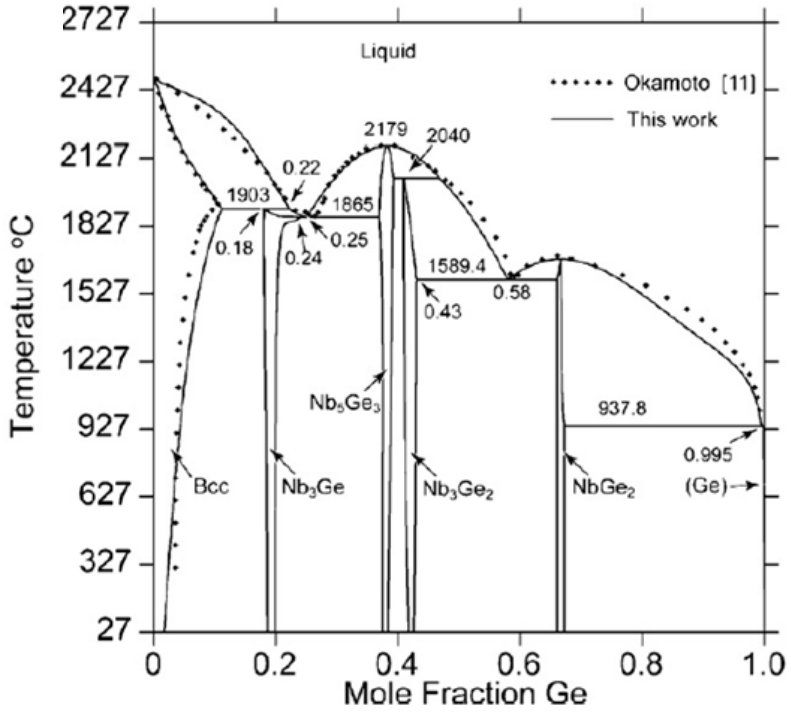

Figure 1.21 The Nb-Ge system (Geng et al., 2011) [1mole Ge = 100 at%Ge]

Table 1.21 Crystal structures of phases in the Nb-Ge system. Data from (Geng et al., 2011)

Phase	**Composition (at% Ge)**	**Pearson symbol**	**Prototype**
(Ge)	99.5-100	cF8	C
$NbGe_2$	66-68.7	hP9	$CrSi_2$
Nb_3Ge_2	41-43	hP16	Mn_5Si_3
Nb_5Ge_3	37-39.3	tI32	W_5Si_3
Nb_3Ge	18.1-24	cP8	Cr_3Si
Nb_{ss}	88.9-100	cI2	W

Table 1.22 Reactions in the Nb-Ge system. Data from (Geng et al., 2011)

Reaction	**Composition (at% Ge)**			**Temperature (˚C)**	**Reaction type**
	A	B	C		
L → $NbGe_2$	66.7	66.7		1680	Congruent
L → Nb_5Ge_3	38.2	38.2		2179	Congruent
L → Nb_5Ge_3 + Nb_3Ge	25	37	24	1865	Eutectic
L→ Nb_3Ge_2+$NbGe_2$	58	43	66	1589.4	Eutectic
L→$NbGe_2$+(Ge)	99.5	67.2	99.7	937.8	Eutectic
L+Nb_5Ge_3→Nb_3Ge_2	46.8	39.3	41	2040	Peritectic
L + Nb_{ss} → Nb_3Ge	22	11.1	18.1	1903	Peritectic
L → (Ge)		100		938.3	Freezing
L → Nb_{ss}		0		2469	Freezing

1.1.20 The Ge-Nb-Si system

The importance of Ge and Si in improvement of the oxidation resistance of Nb silicide alloys have been mentioned in previous sections. Ge-Si phase diagram shows complete solid solubility (Olesinski and Abbaschian, 1990). In the metal rich corner of Nb-Si binary (Figure 1.1), Si forms 3-1 and 5-3 silicides. The 5-3 silicide comprises of βNb_5Si_3 and αNb_5Si_3 with the latter being stable to room temperature. The 3-1 silicide is unstable below 1700 °C. According to Geng et al. (2011) germanium forms Nb_5Ge_3 and Nb_3Ge which are both stable to room temperature. The former is isomorphous with βNb_5Si_3 while the latter is isomorphous with metastable 3-1 silicide formed by Nb (see Table 1.4). Thus Ge-Nb-Si ternary is important in understanding how Ge would affect phase equilibria in Nb silicide based alloys. The 1780, 1800 and 1820 °C isothermal sections of Ge-Nb-Si system reported by Pan et al. (1982) are shown in Figure 1.22.

Region of transit to a stable ternary isomorphous phase (see section 5.4.2.2, page 164)

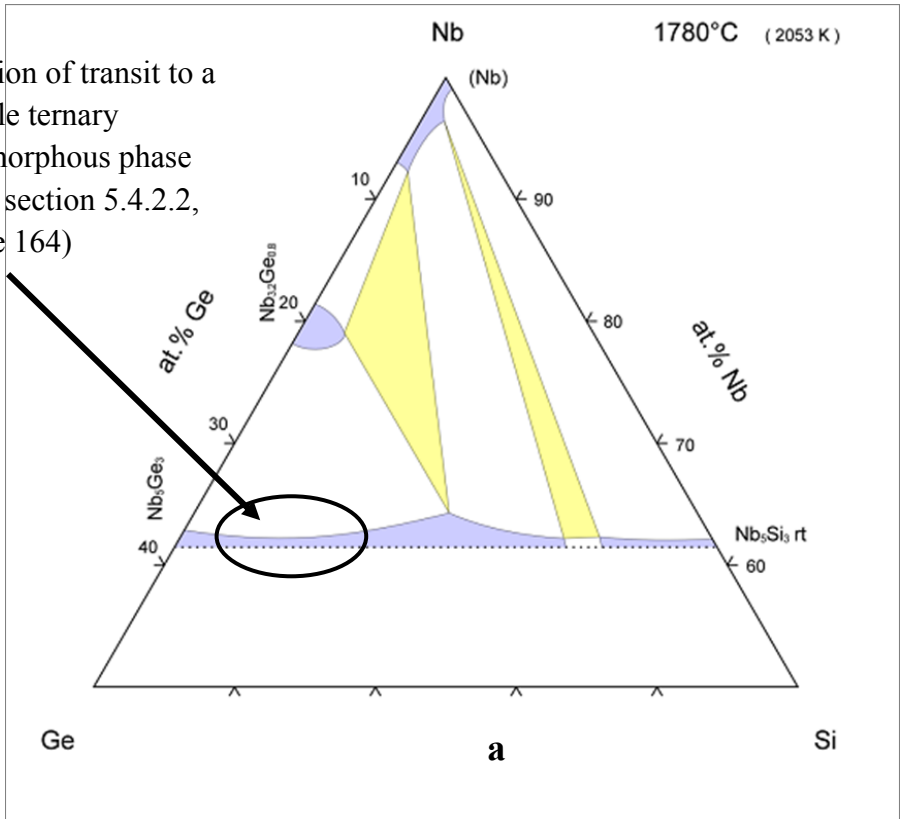

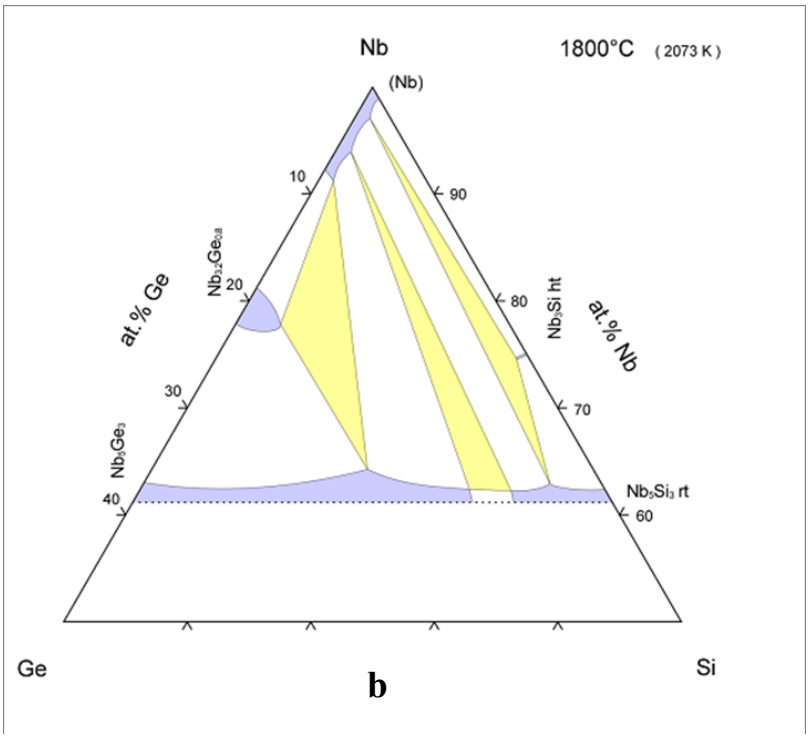

Figure 1.22 continues on next page.

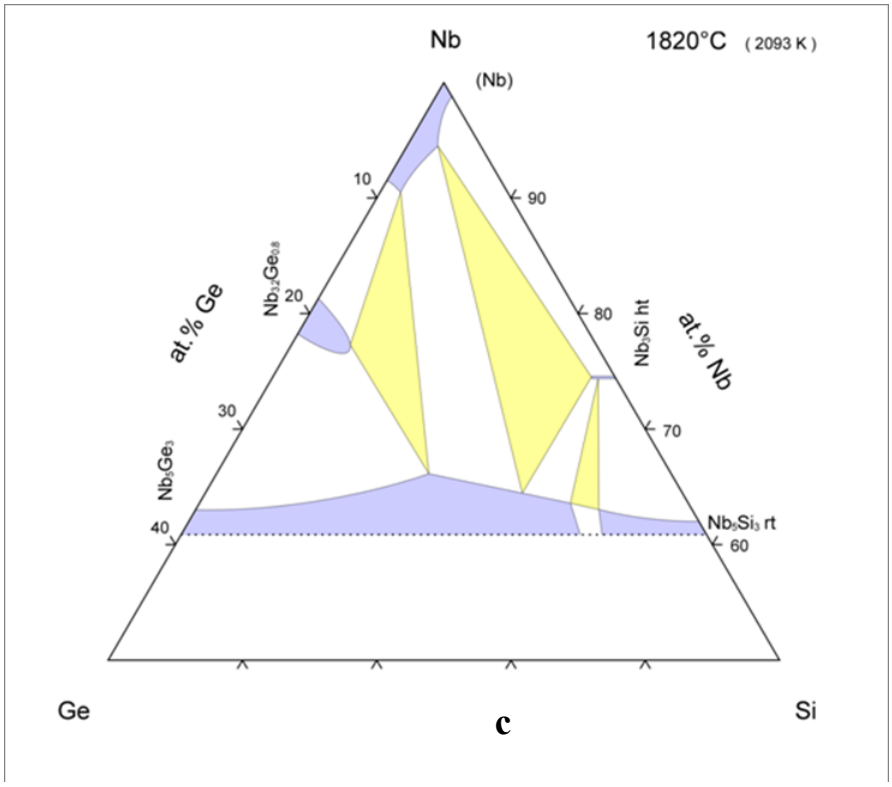

Figure 1.22 The Ge-Nb-Si (a to c) 1780 °C, 1800 °C and 1820 °C isothermal sections (Pan et al., 1982). Reprinted with permission of ASM International.

1.2 Processing

Properties of Nb silicide based alloys depend on the alloy's chemistry and processing route. The latter presents challenges due to high melting points and high reactivity of the elements. A series of processing methods has been employed to make Nb silicide based alloys. These include casting (arc-melting and directional solidification), powder metallurgy (HIP and sintering pre-alloyed powders, mechanical alloying) and thermo mechanical processing (forging and extrusion). Each of these approaches has produced laboratory-scale volumes of materials with characteristic microstructure for property studies.

1.2.1 Arc melting

The major challenges in melting and casting of the Nb silicide based alloys are their high liquidus temperatures and high reactivity with mould materials. This influenced

super heating and choice of moulds. These challenges are overcome by using cold-crucible methods, in which the charge is melted and cast in the same mould. The crucible mould is made of copper. Homogenisation of the ingot is achieved by turning and remelting the ingot for several times.

Arc melting technique involves usage of either consumable or non-consumable electrode. While melting, the stirring of the molten alloy by the plasma can be controlled by varying the current and electrode to melt distance. By extinguishing the heat source, the molten alloy is cooled in a water-cooled copper crucible. Alloys made in our group using non-consumable electrode arc melting have shown loss of alloying elements.

1.3 Properties

The Nb silicide based alloys must meet property goals for toughness, creep and oxidation. The fracture toughness goal is minimum toughness of 20 MPa√m, the creep goal is creep strain of < 1% in 125 hours at T > 1200 °C for tensile stresses of at least 175 MPa, and for the oxidation goal the oxidation losses of < 0.25 μm / h at 1315 °C for 100 h exposure (Bewlay et al., 2003b) and the alloy must not suffer from pest oxidation (Tsakiropoulos 2010).

The Nb_{ss} is the key phase for achieving the required property goals. Its chemistry, vol%, size and spatial distribution in the microstructure are important for ductile phase toughening and oxidation behaviour, with high vol% expected to benefit toughness but being detrimental to oxidation. The creep properties of the Nb_{ss} are inferior to those of silicides, thus high vol% of the Nb_{ss} in the microstructure is undesirable for meeting the creep goal. Figure 1.23 shows the secondary creep rate behaviour of monolithic Nb_5Si_3 at 1100 °C in comparison with binary Nb + Nb_5Si_3 alloys and other intermetallic and commercial materials of high temperature application. Figure 1.24 shows that measurable elongation is possible with increasing temperature whereas yield strength and ultimate tensile strength increases to some maximum value and then fall sharply (Kim et al., 2003).

Figure 1.23 The comparison of secondary compressive creep behaviour of monolithic Nb_5Si_3 and Nb + Nb_5Si_3 at 1100 °C with some commercial high-temperature materials (Bewlay et al., 1996)]. Removrd.

Figure 1.24 The tensile properties of the alloy Nb-18Si-5Mo-5Hf (mol%) in situ composite at ambient temperature and selected elevated temperatures (1470, 1570, 1670 and 1770 K) (Kim et al., 2003). Removed.

1.3.1 Toughness

The chemistry of the solid solution is important regarding its fracture toughness. Alloying elements in solution in Nb are known to affect its DBTT. Pioneering work carried out by Begley (1994) on the effect of some binary additions on the DBTT of niobium was summarised in Figure 1.25a. Figure 1.25b shows the effect of the interstitials nitrogen and oxygen on the DBTT of niobium.

Obviously, the additions of Hf and Ti have no significant effect on the DBTT of niobium but Zr increases it to -100 °C at ~ 12 at% while smaller additions of Re, Al, Cr, W and Mo have a much more pronounced effect. Nitrogen and oxygen have strong effect on the DBTT of niobium with nitrogen increasing it beyond -50 °C at ~ 0.2 at% (Grill and Gnadenberger, 2006). The data shows how important are to control the contaminations by N and O during processing. Even more than 30 at% Ti or Hf; up to 16 at% Zr; up to 10 at% V; up to 7 at% Mo; about 5 at% Cr; about 4 at% W and less than 5 at% Al could be added to niobium in binary alloys, without raising the DBTT above the critical limit of -50 °C.

Figure 1.25 The effects of (a) alloying elements (b) nitrogen and oxygen on the DBTT of niobium (Grill and Gnadenberger, 2006, Begley, 1994). Removed.

The intermetallic phases (β and α) Nb_5Si_3, A15 Nb_3Sn and C14 $NbCr_2$ (this structure of the Laves phase is stabilised by Si and Al) are desirable, the (β and α) Nb_5Si_3 and A15 Nb_3Sn for high temperature strength and the C14 $NbCr_2$ for oxidation resistance. In monolithic form, polycrystalline Nb_5Si_3 has a fracture toughness of 1-3 MPa√m (Mitra, 2006). Ti addition improves the fracture toughness of the niobium silicide alloy (Chan, 2002, Chan and Davidson, 1999) see Figure 1.26.

The toughness of the Laves phase is also very low and like Nb_5Si_3 improves with alloying, see Figure 1.27. In the case of the Nb_5Si_3 silicide the best toughness is achieved with about 30 at%Ti substituting for Nb. However, it should be noted that at such high Ti content the structure of Nb_5Si_3 is likely to change from the desirable tetragonal to the undesirable hexagonal structure. The solid solubility of Ti in the Nb_5Si_3 depends on other alloying additions, in particular Hf and the actual Ti content of the Nb_5Si_3 also depends on the Ti content of the alloy. The latter should not exceed 25 at% owing to the strong effect of Ti on the alloy liquidus and the detrimental effect of Ti on high temperature strength.

Figure 1.26 Fracture toughness of $D8_l$ Nb_5Si_3, $D8_8$ Ti_5Si_3 and alloyed $D8_l$ and $D8_8$ Nb-based silicides as a function of Ti content (Chan, 2005). The $D8_1$ is the tetragonal and $D8_8$ the hexagonal structure respectively. Removed.

Figure 1.27 Fracture toughness of C14 and C15 Nb-based Laves phases as a function of Cr content (Chan, 2005). Removed.

The fracture failure of Nb silicide based alloys initiates with cracking of intermetallic phase(s), for example Laves ($NbCr_2$) and 5-3 silicide particles (Figure 1.28), followed by the blunting of the cracks and bridging of the main crack and micro cracks by intact ligaments, stretching, and failure of the bridging ligaments. The solid solution phase provides the ligaments (Chan, 2002).

Figure 1.28 The fracture mechanisms in Nb silicide based alloy showing particle fracture and crack bridging: (a) cracked $NbCr_2$ (dark) particles and intact Nb_{ss} (light phase) ligaments in $Nb_{ss}/NbCr_2$ and (b) cracked Nb_5Si_3 particles and intact Nb_{ss} ligaments in Nb_{ss}/Nb_5Si_3 (Chan, 2002).

Deformation mechanisms identified in Nb silicide alloys are interface de-bonding, plastic deformation of Nb_{ss} and cleavage of the silicide and Laves phases (Chan, 2002, Kim et al., 2003). Cleavage fracture involves splitting of the silicide. Plastic deformation of Nb_{ss} means stretching of Nb_{ss} beyond elastic limit followed by necking and final rupture. Interface de-bonding involves separation of Nb_{ss} from the silicide and/or Laves phase along the boundary line. Because there is high level of stability between these phases, the interfacial-bond-strength is so strong that limited de-bonding occurs (Mitra, 2006). The resultant effect is that the highly constrained Nb_{ss} which is the ductile phase also fails by cleavage fracture especially at low (< 1200 °C) temperatures and no ductility is observed. At high (> 1200 °C) temperatures, the Nb_{ss} possess greater potential to suppress crack escalation within itself. Improved ductility of Nb_{ss} due to temperature increase, reduced stress concentration at Nb_{ss}/Nb_5Si_3 interface and as a result significant elongation of Nb_{ss} occurs before the rupture of Nb_{ss} (Kim et al., 2003). The thicker the Nb_{ss}, the greater is the elongation.

Table 1.23 shows fracture toughness values of some Nb_{ss}/Nb_5Si_3 alloys processed by different methods. This shows that processing is the key to improving the toughness of Nb silicide based alloys and that Al, Cr and Hf in synergy with Ti can improve room temperature fracture toughness to over 20 MPa$\sqrt{m}$.

Table 1.23 Room temperature fracture toughness of Nb_{ss}/silicide based alloys processed by different methods, data from (Mitra, 2006).

CONTENTS REMOVED

1.3.2 High temperature strength

The strength of Nb silicide based alloys depends on chemistry and volume fraction of the Nb_{ss}, and type(s) of intermetallic phase(s) present in the microstructure. Regarding high temperature strength, specific alloying additions including refractory metals are important. Considerable strengthening has been reported when Nb is alloyed with Cr, Mo, Re, V and W in binary alloys. Figure 1.29 show the 0.2% yield strength of binary Nb-X alloys at 1095 °C (Begley, 1994).

Figure 1.29 The effect of binary additions on yield strength of niobium (Begley, 1994) .

Gettering of oxygen by Zr and Hf contribute to their strengthening effects. Ti has a weak strengthening effect on the yield strength compared with Mo, Re, V and W. Contamination by interstitials like nitrogen could lead to false strength values (Grill and Gnadenberger, 2006). Begley (1994) reported the results of the study by McAdam on substitution binary additions on the high temperature strength of niobium. These are presented in Figure 1.30 as a percentage of the effect of tungsten, the most potent solid solution strengtheners. In Figure 1.30 the zero line represents the strength of unalloyed niobium. The data show that Ti, Zr, Hf and V have negative effect and that Mo and Ta have stronger effects compared with Cr.

The creep deformation of Nb silicide based alloys depends on the Nb_{ss} and intermetallic phases present. For two phased silicide based alloys consisting of Nb_{ss} and silicide, creep deformation is under the control of the Nb_{ss} at < 12 at% Si and by the silicide phase at > 20 at% Si, Figure 1.31. The 12 at% Si provides ~70 vol% Nb_{ss} and ~30 vol% silicide phase while 18 or 22 at%Si provide 40 or 30 vol % and 60 or 70 vol % Nb_{ss} and silicide phases respectively. The minimum secondary steady state creep rate occurs at about 18 at%Si (Bewlay et al., 2002). Diffusion of niobium atoms is the dominant mechanism for creep deformation of Nb silicide alloys. However, at > 20 at% Si the cracking of silicide phases becomes dominant. The rate of diffusion is highest in the solid solution and this accounts largely for the poorer creep performance of the composite at higher temperatures and stresses compared to the monolithic silicide phase.

Figure 1.30 The strengthening effect of alloying elements in columbium (niobium) (Begley, 1994). Removed.

Figure 1.31 The effect of metal and silicide volume fractions on secondary creep behaviour of a two phased quaternary Nb silicide based alloy, expressed as a percentage of silicon content at 1200 °C and 140 – 280 MPa stresses (Bewlay et al., 2002). Removed.

1.3.3 Oxidation

The design of Nb silicide based alloys with oxidation resistance to meet this property goal has focused entirely on eliminating any internal oxidation and form adherent, continuous and non-porous oxide scale on the surface and at the same time maintaining a balance of mechanical properties. This involves inclusion of alloying elements which can severely reduce the diffusivity of oxygen in niobium, elements that have greater affinity for oxygen than Nb and can form protective oxide at the surface without conducting the oxygen into the bulk alloy. Alloying elements like Al, Cr, Hf, Sn and Ti have been reported to improve the oxidation resistance of Nb silicide

based alloys. The oxidation of developmental Nb silicide based alloys has been found to consist of high metal deterioration rates, spalling of the oxide scale and disintegration of both the oxide and alloy. Nb dissolves a substantial amount of oxygen causing hardening and embrittlement of Nb phase in the alloy (Subramanian et al., 1997).

Binary Nb alloys with additions like W, V, Mo, Zr and Ta have poor oxidation resistance. Niobium silicide based alloys with Ti, Al and Hf additions have shown very significant improvement in oxidation resistance over the Nb-Si binary alloys (Subramanian et al., 1997). Cr stabilises the Cr rich Laves phase that has excellent oxidation behaviour. Hf showed no impact on oxidation in the presence of Cr and Al. Alloying with Ge showed the best oxidation resistance at 6 at%, whereas alloying with B is best in the range 2-6 at%. Beyond this concentration, the Ge addition becomes unfavourable as it lowers the melting point. Addition of Sn is considered to be beneficial at temperatures below 1000 °C. The Sn addition has entirely eliminated the problem of pest oxidation which occurs at intermediate temperatures (500-800 °C).

Figure 1.32 shows advances in cyclic oxidation of uncoated Nb silicide based alloys and set goals.

Figure 1.32 The oxidation performance of recently developed Nb silicide composite (Nb silicide B) and the pre 1998 denoted by Nb silicide D in the figure (Bewlay et al., 2003a). Removed.

The figure shows material loss against temperature. The increase in temperature capability from 871 to 1370 °C depicts the improvements in comparison with previously developed alloys denoted by the dotted line (Nb silicide D). Two goals were set, the short and long-term goals. The short-term goal is material loss of less than 200 μm in 10 h of exposure at 1370 °C while the long term goal is material loss of less than 25 μm in 100 h at 1315 °C. The overall aim of these goals is to achieve the same oxidation life at 1315 °C as a second generation superalloy at 1150 °C.

The short-term goal would ensure that the uncoated alloy survived engine test in an uncoated condition in which allowable material loss is 190 μm. Uncoated Nb silicide alloys have met this goal as the measured material loss was 100-125μm. Recent developmental Nb silicide has shown less than 25μm material loss in 100 h at ~1200 °C but not at 1315 °C (Bewlay et al., 2003b).

1.4 Summary of the literature review and research objectives

The "desirable phases" for the new alloys of this study are the tetragonal (β or α) Nb_5Si_3 (for creep), Nb_{ss} no Si (for fracture toughness), C14 $NbCr_2$ Laves (for oxidation resistance) and A15 Nb_3Sn (for hot strength retention). Al, Cr, Ge, Mo, Sn and W promote the stability of the tetragonal Nb_5Si_3; Ti and Hf promote the stability of the unwanted hexagonal γNb_5Si_3; Al, Si stabilise the C14 $NbCr_2$ Laves, and Al, Cr, Ge, Mo and Si promote the stability of the A15 Nb_3Sn.

In this work, for the first time (to the knowledge of the author), the Nb-Ti-Si-Hf-Mo-W-Sn-Ge-Cr-Al silicide based alloy system is selected for study. Three groups of alloys (BA-alloys series) were designed, see Table 2.1: (1) alloys without Cr and Al (alloys BA1 and BA6) in which Ti-Si-Hf-Mo-W concentrations are kept constant while increasing the concentrations of Sn and Ge at constant ratio (1:1); (2) alloys with Cr and Al (alloys BA2, BA3, BA3b and BA5) in which Ti-Si-Hf-Mo-W contents are kept constant at same concentration as in the BA1 while increasing Sn-Ge-Cr-Al concentrations at constant ratio (1:1:1:1). Alloys BA2, BA3 and BA3b nominal compositions are same but have significantly different actual compositions (given in their respective result's sections) owing to significant losses in Sn (a processing problem encountered as Sn nominal concentration was increased from 2 to 5 at% - this problem was successfully addressed, see Table 2.2); (3) alloys with higher concentrations of Ti (alloys BA4 and BA7) in which Si-Hf-Mo-W-Sn-Ge-Cr-Al contents are same as in BA3b.

In designing the alloys of this study, results from previous studies were considered. Particular attention was on the chemistry of Nb_{ss} (Si content), the stability of A15 Nb_3Sn and the structure of the Nb_5Si_3 (hexagonal or tetragonal).

The unwanted hexagonal γNb_5Si_3 structure is stable in alloys with 24 at%Ti + 5 at%Hf in their nominal alloy compositions – see Grammenos and Tsakiropoulos (2010) and Geng et al. (2007a).

The desired A15 Nb_3Sn which is stable in the alloy Nb-24Ti-18Si-5Sn (NV6) Vellios and Tsakiropoulos (2007) is "destabilised and chemistry of Nb_{ss} significantly modified" by addition of 5Cr + 5Al + 2Mo + 5Hf as is "the case" in the alloy Nb-24Ti-18Si-5Cr-5Al-2Mo-5Hf-5Sn (JG6). According to Geng et al. (2007a, 2007b) and Geng and Tsakiropoulos (2007), γNb_5Si_3, Si-rich C14 $NbCr_2$ Laves phase, "Sn-rich Nb_{ss}" and "Sn-poor Nb_{ss}" formed in the alloy JG6. In the "Sn-rich Nb_{ss}" the average Si content is 4.6 at%. This is high and undesirable in the Nb_{ss}.

The destabilisation of the A15 Nb_3Sn observed by Geng et al. in the alloy JG6 arouses enormous curiosity (evidenced by the number of publications it received), considering that Al, Cr, Mo and Si form phases with A15 structures, and as such are expected to stabilise the A15 Nb_3Sn individually and in synergy.

Therefore, the question arising: **why is A15 Nb_3Sn not stabilised in the alloy JG6 where Sn (5 at%) is in synergy with 18Si + 5Cr + 5Al + 2Mo?** (See section 4.3.3.1, paragraphs 3 and 4 on pages 124/125 of this thesis).

The base alloy for this study, alloy BA1 (Nb-11Ti-18Si-1Hf-6Mo-2.5W-2Sn-2Ge) was designed to modify the crystal structure of Nb_5Si_3 (from hexagonal to tetragonal structure) by increasing the concentration of RM (Mo+W) while keeping Ti and Hf concentrations low compared to JG6 (Nb-24Ti-18Si-5Cr-5Al-2Mo-5Hf-5Sn) and YG3 (Nb–18Si–24Ti–5Hf), and to see how Mo and W in synergy with Sn and Ge affect the chemistry of Nb_{ss}. A15 Nb_3Sn was not expected to be stable at the low (~ 2 at%) concentration of Sn in the BA1; however, after appropriate heat treatment, a small but

significant vol% of stabilised A15 phase was observed.

The alloy BA2 was designed to see how Mo and W (in synergy with Sn and Ge) will affect the structure of Nb_5Si_3, chemistry of Nb_{ss} and stability of A15 Nb_3Sn at lower concentrations of Ti and Hf, in the presence of Cr and Al. In this alloy, we also aim to introduce the C14 $NbCr_2$ Laves phase into the microstructure, for improved oxidation resistance. The alloy BA3 was essentially, a repeat of alloy BA2, in a bid to eliminate

the significant loss of Sn observed in the latter. However, greater loss of Sn was observed in the alloy BA3 and confirmed significant loss of Sn in BA alloys series as the nominal content of Sn is increased.

Owing to the significant losses of Sn in the alloys BA2 and BA3, the nominal composition of the alloy BA2 was again reproduced in BA3b. This time Sn compensation was made.

The alloy BA3b was severely cracked (see Figure 5.13a) after hot mounting (see Chapter 2). Therefore, alloy BA4 was designed to first tackle the toughness issue with the alloy BA3b (by increasing Ti content) and, secondly, to see how the structure of the Nb_5Si_3, and the chemistry of Nb_{ss}, will be affected at this higher Ti concentration which is lower than those in JG6 and YG3.

The alloys BA5 and BA6 were designed to explore the role played by Cr and Al in the core / shell macrostructure formation observed in BA3b.

The alloy BA7 was designed to explore the role of Ti concentration on the core / shell macrostructure formation observed in BA4.

CHAPTER 2

EXPERIMENTAL PROCEDURES

This chapter presents the alloys selected for this study, processing route and the techniques used for the characterisation of the alloys. The alloys were made using non-consumable tungsten electrode arc melting, and casting in a water-cooled copper mould. The microstructures of the alloys were characterised using x-ray diffraction (XRD), and scanning electron microscopy (SEM) with energy dispersive x-ray spectroscopy (EDS) analysis; the oxidation properties were evaluated using thermo-gravimetric analysis (TGA) technique or in air without TGA, and the hardness properties of the alloys were determined using the Vickers hardness test method.

2.1 Selection of alloy compositions

The nominal compositions (all compositions are in at% unless otherwise stated) of the Nb silicide alloys designed for this study are given in Table 2.1. The Sn compensated nominal composition is given in Table 2.2.

Table 2.1 The designed nominal compositions (at%) of the BA-alloys series.

Alloy Code	Elements (at%)									
	Nb	**Ti**	**Si**	**Hf**	**Mo**	**W**	**Sn**	**Ge**	**Cr**	**Al**
BA1	57.5	11	18	1	6	2.5	2	2	-	-
BA2	41.5	11	18	1	6	2.5	5	5	5	5
BA3	41.5	11	18	1	6	2.5	5	5	5	5
BA3b	41.5	11	18	1	6	2.5	5	5	5	5
BA4	32.5	20	18	1	6	2.5	5	5	5	5
BA5	53.5	11	18	1	6	2.5	2	2	2	2
BA6	51.5	11	18	1	6	2.5	5	5	-	-
BA7	37.5	15	18	1	6	2.5	5	5	5	5

Table 2.2 The converted Sn compensated nominal compositions (at%) of BA3b, BA4, BA6 and BA7 of the BA-alloys series.

CONTENTS REMOVED

The microstructures of the Nb silicide based alloys contain Nb_{ss} and Nb based intermetallics such as Nb_3Si, Nb_5Si_3 and other intermetallics as appropriate. The percentage volume of the silicide phase(s) in higher order alloys depends on the synergy of Si with other elements. In the silicides simple metals (Al, Sn) and metalloids (Ge) can substitute for Si whereas transition (Cr, Hf, Ti) and refractory metals (Mo, W) for Nb. Upon alloying the crystal structure of Nb_5Si_3 can change from tetragonal (β or α desirable) to hexagonal (undesirable). Depending on temperature and composition, the tetragonal can change from β to α (α is the most preferable owing to better isotropic properties) and vice versa.

Resistance to creep is maximum when Si content is about 18 at% and vol% of silicide phase about 60% (Bewlay et al., 2002). Hence the alloys of this study were based on 18 at%Si. Silicon is also beneficial (i) for high (> 1200 °C) temperature oxidation resistance of the alloys and stabilises the C14 Laves phase, which is also beneficial for oxidation resistance (Jackson and Bewlay, 1999) and (ii) for alloy density.

Titanium in the range 10 to 15 at% in Nb-Ti alloys exerts positive influence on the high (1095 °C) temperature yield strength of Nb but has negative effect at higher concentrations (Figure 1.29). Titanium has no significant effect on the DBTT of Nb up to about 12 at%, and increases the DBTT from – 200 °C to about – 100 °C at ~ 25 at% (Figure 1.25). Titanium also improves significantly the fracture toughness of the Nb_{ss}

by decreasing the energy required to move dislocation (Peierls-Nabarro barrier energy) in the solid solution (Chan and Davidson, 1999) and of Nb silicide alloys (Chan, 2005, Jackson et al., 1996). Ti substitution for Nb in Nb_5Si_3 improves the toughness of Nb_5Si_3 by decreasing the strength of Nb-Si bond by forming Nb(Ti)-Si bond, but above 25 at%Ti the hP16 (hexagonal) $(Ti,Nb)_5Si_3$ is stabilised. The latter is considered to be detrimental for creep (Bewlay et al., 2002). The synergy of Hf and Ti can lead to stabilization of the hP16 $(Ti,Nb)_5Si_3$ when Nb/(Ti+Hf) is about 0.9 or lower for example stabilisation of γNb_5Si_3, which has hP16 structure was possible in the Nb-24Ti-18Si-5Al-5Cr-2Mo-5Hf alloy where both tetragonal and hexagonal 5-3 silicide formed (Geng et al., 2007a). Titanium also stabilises the tP32 Nb_3Si to temperatures lower than 1700 °C (Figure 1.5) and (Qu et al., 2007, Zelenitsas and Tsakiropoulos, 2005). Titanium has also been reported to be very beneficial for the oxidation resistance of Nb silicide based alloys, by reducing oxygen diffusion through the Nb_{ss} (Zelenitsas, 2005) and the oxidation properties of these alloys tend to improve as the Nb/Ti ratio in Nb_{ss} decreases. The Ti addition must be optimised due to its adverse effect on liquidus temperature and creep (Figures 1.5 and 1.30).

Hafnium was reported to be beneficial for oxidation resistance of Nb silicide alloys (Geng and Tsakiropoulos, 2007) and has similar effect as Ti on the DBTT of Nb but has negative effect on high temperature (≥ 1200 °C) retention (Figure 1.30). Hafnium is beneficial for controlling contamination of the alloys by oxygen as it scavenges oxygen and forms HfO_2. The latter however has adverse effect on toughness.

Sn and Ge were reported to be beneficial to the oxidation resistance of Nb silicide alloys (Geng and Tsakiropoulos, 2007, Zifu, 2012). It has been shown that both elements destabilise the (tP32) Nb_3Si (Vellios and Tsakiropoulos, 2007, Zifu and Tsakiropoulos, 2010) with Sn being more effective. Both elements can have adverse effect on the vol% of Nb_{ss} which is very important for fracture toughness and ductility. Tin partitions to the Nb_{ss}, and stabilise the (cP8) Nb_3Sn at ~ 5 at% whereas Ge partitions to the silicide and is expected to partition to Nb_3Sn.

Mo and W form complete solid solutions with Nb, and in Nb-Si-Q alloys (Q = Mo, W) partition to the Nb_{ss} and suppress the Nb_{ss} + Nb_3Si eutectic. The latter was replaced by

Nb_{ss} + Nb_5Si_3 eutectic for Q concentrations ≥ 3 at% (Figures 1.16 and 1.18). Both elements give strong solid solution strengthening to the Nb_{ss} and have been reported to improve hot strength retention and creep resistance of Nb, with W being the most effective (Figure 1.30). However, Mo and W have negative influence on the DBTT of Nb in Nb-Q alloys (Figure 1.25). At about 4 at% W and 7 at% Mo the DBTT of Nb is raised above -50 °C. The fracture toughness of Nb-Si-Mo silicide based alloys is better by addition of 5 at%Mo (Kim et al., 2002). Molybdenum at > 6 at% significantly deteriorate the oxidation resistance of Nb silicide based alloys (Mitra, 2006). The 6 at% Mo was chosen for this study to balance oxidation resistance with strengthening. Tungsten was kept at 2.5 at% to balance density with strengthening.

Aluminium and Cr are detrimental to fracture toughness but desirable for oxidation resistance. Al is also desirable because it destabilises the Nb_3Si and the Nb_{ss} + Nb_3Si eutectic that is replaced by the Nb_{ss} + Nb_5Si_3 eutectic and enhances the transformation of βNb_5Si_3 to αNb_5Si_3. Al also stabilises the C14 $NbCr_2$ Laves phase to lower temperature. However, Al (≥ 4 at%) and Cr (> 3.5 at%) have adverse effect on the DBTT of Nb (Begley, 1994) and the toughness of Nb silicide alloys. Thus, the sum Al+Cr content is critical.

2.2 Preparation of ingots

The arc-melter used in this study is shown in Figure 2.1. The starting materials for the alloys of this study were high purity (wt%) elements of Nb (99.9 %); Ti (99.95%); Si (99.9%); Hf (99.7%); Mo (99.5%); W (99.99 %); Sn (99.99 %); Ge (99.99 %); Cr (99.5%) and Al (99.99%).The elemental charges were melted in a water-cooled copper crucible under argon atmosphere using a non consumable tungsten electrode. The chamber was evacuated to < 10^{-3} Pa via a rotary pump and a diffusion pump. Prior to melting, the chamber was back filled with argon to a pressure of ~ 50 kPa. A voltage of ~ 50 V and current of ~ 600 A were used to arc melt the charge. Pure Ti was melted first before melting the alloy charge and intermittently as an oxygen getter. To ensure homogeneous melt, each alloy button was turned over and re-melted four times. The melt was left in the water-cooled copper hearth to cool down to ambient temperature. Figure 2.2 shows a typical button of the cast alloy.

Figure 2.1 Photograph of the arc-melter used in making the alloys of this study.

Figure 2.2 A typical photograph of as cast alloy of this study (diameter ~ 18mm; thickness ~ 8mm).

2.3 Preparation of specimens for microstructure characterisation

The ingots were cut so that the bottom, middle and top areas of the button could be studied. Non-ferrous diamond blade in Isomet 5000 linear precision saw was used to cut the specimens. While cutting, the blade was cooled using 1 part cool 2 fluid to 3 parts of water (41-10102 Buehler product). The exposed surfaces were then mounted in conductive bakelite using automatic mounting press, heated and cooled for 8 and 4 minutes respectively, ground and polished using 120/240/400/600/800/1200 water-cooled SiC grits on manual polisher and 6/3/1 μm diamond pastes. All efforts were

made to ensure that the surfaces were flat. Each time a grit or paste was changed the samples were thoroughly rinsed in water, cleaned in isopropanol, dried using a warm air blower and then turned 90°. Prior to analysis all samples were ultrasonically cleaned with isopropanol for 10 minutes.

2.4 Heat treatment

Cross sections from the ingots were wrapped in Ta foil and placed in an alumina boat and heat treated at 1500 °C for 100 h in a calibrated tube furnace under flowing argon with volumetric flow rate of 10^{-5} m^3s^{-1}. Another alumina boat with pure Ti sponge was placed at the entrance of the argon flow (as oxygen getter) in the furnace. A heating rate of three degrees per min was used to raise the temperature of the specimens to 1500 °C and was held for 100 h. The specimens were furnace-cooled with a cooling rate of three degrees per min.

2.5 X-ray diffraction

The XRD studies of the alloys were carried out using fine powders of the cast and heat-treated alloys prepared using pestle and mortar. STOE STADI P Diffractometers (IP – Imaging plate and PSD – Position sensitive detector) were used with $CuK_{\alpha 1}$(λ=1.54056Å) radiation to record the diffractograms. The data from the IP detector and International Centre for Diffraction Data (ICDD) were used for the identification of constituent phases. The data from the PSD detector was used to determine the lattice parameters of the phases in the cast and heat treated specimens using Refine and Index in $WinX^{POW}$.

2.6 Scanning electron microscopy with quantitative energy dispersive spectrometry

Back-scatter electron images of the samples were taken in Jeol 6400 and InspectF SEMs while quantitative chemical analyses to (i) determine the bulk and (ii) the composition of the constituent phases in the alloys in the cast and heat treated conditions were carried out in the Jeol6400 or Psem500 (Philips-Sem) equiped with energy dispersive x-ray spectroscopy. Prior to EDS analyses, pure Co was used for calibration and dead time (in Jeol6400 SEM) maintained at 26% and calibration count rate (in Psem500) maintained between 1950 to 2500 cps by adjusting the probe current. The calibration was repeated after 5 analysis. High purity Al, Cr, Ge, Hf, Mo, Nb, Si, Sn, Ti and W were used as standard for the EDS analyses. The analysed phases

were ≥ 5 μm in diameter and an acceleration voltage of 20 kV (Jeol6400 SEM) and 25 kV (Psem500) were used. Ten spot-analyses were done for each phase. Analyses to determine the overall composition (large area analysis) of the alloys were done at low magnification, with five analyses each at the bottom, middle and top areas of the specimen. The ZAF correction (Z = atomic mass, A = absorption and F = fluorescence) was applied and the result was normalised to give concentration in 100%. EDS data were reported with the average, minimum and maximum values, and standard deviation.

The %area of the 5-3 silicide (+ C14 Laves) was calculated using Image J software.

2.7 Hardness measurement

Vickers macro indentation hardness of the alloys were measured using a load of 10kg and holding time of 15 seconds on a Struers Durascan 70 hardness machine. A minimum of ten indents were taken for each specimen.

2.8 Thermo-gravimetric analysis (TGA)

Thermo-gravimetric analysis was carried out at 800 °C and 1200 °C for 100 h. Rectangular cubes were cut from the cast alloys, and their surfaces were ground to 400 grits. The mass of the specimens were measured using a Mettler Toledo mass balance, model: MS104S/01 (accuracy 0.0001g). The surface areas were measured using a Polyvar optical microscope. Prior to the isothermal oxidation, the specimen was cleaned in isopropanol for 5 mins and was placed in alumina crucible. Isothermal oxidation at designated temperature was carried out using a STA449 F3 Jupiter instrument. The heating and cooling rate was 3° per min.

An oxidation test was also carried out in air at 1500 °C for 100 h using a Lenton furnace.

2.9 Density measurement

The density measurements for the alloys were carried out using a MS104S Mettler Toledo analytical balance (accuracy 0.01g/cm^3). Five measurements were taken for each alloy and the average value calculated.

CHAPTER 3

THE MICROSTRUCTURE OF THE ALLOY Nb-11Ti-18Si-1Hf-6Mo-2.5W-xSn-xGe

3.1 Introduction

Availability of new ultra high temperature materials can lead to improved efficiency of gas turbines while using turbine inlet temperatures approaching 1800 °C. Nb silicide based alloys can offer a balance of attractive room and elevated temperature properties (Subramanian et al., 1997, Bewlay et al., 1996).

In the Nb silicide alloys, boosting and complementing the desired intrinsic properties of the bcc Nb_{ss}, tetragonal Nb_5Si_3, and forming in the microstructure new phases with beneficial properties has become the pivot in these alloys development. Vellios and Tsakiropoulos (2007) studied the role of Sn and Ti additions in microstructure of Nb-18Si based alloys and reported the stabilisation of A15 Nb_3Sn with Si/Sn ~ 1 in the alloys Nb-18Si-5Sn (NV9) and Nb-24Ti-18Si-5Sn (NV6). Although it is not categorically stated by Vellios and Tsakiropoulos, the A15 Nb_3Sn in these alloys formed independent of Nb_{ss} and would mean that A15 Nb_3Sn formed congruently with Si/Sn = 1. A15 Nb_3Sn is important in the Nb silicide based alloys for hot strength retention.

According to Vellios and Tsakiropoulos, the synergy of Ti + Sn causes macrosegregation of Si. The latter is not observed in Nb-24Ti-18Si (KZ3) (Zelenitsas and Tsakiropoulos, 2005) and Nb-18Si-5Sn (NV9) (Vellios and Tsakiropoulos, 2007).

Tin is very effective at destabilisation of Nb_3Si (this phase is stabilised by Ti). Nb_3Si did not form and βNb_5Si_3 was the primary solidification phase in the alloys NV6 and NV9. Vellios and Tsakiropoulos also reported that Ti partitions to both βNb_5Si_3 and Nb_{ss}, solubility of Ti in Nb_{ss} increase in the presence of Sn but that of Sn decrease in the βNb_5Si_3 with increase in Ti; the solubility of Ti in βNb_5Si_3 is sensitive to cooling rate and that Sn partitioned to Nb_{ss} and has no significant effect on the chemistry of Nb_{ss} (Si solubility).

However, Sun et al. (2012) in their thermodynamic description of Nb-Si-Sn ternary system (supported by their own experimental work) reported αNb_5Si_3 as the primary phase for the composition Nb-18Si-5Sn and that eutectic in the alloy is a ternary eutectic consisting of Nb_{ss} + αNb_5Si_3 + A15 Nb_3Sn (Sun et al., 2012).

Zifu and Tsakiropoulos (2011) studied the effects of Ti and Ge in the microstructure of Nb-18Si-5Ge (ZF1), Nb-18Si-10Ge (ZF2) and Nb-24Ti-18Si-5Ge (ZF3) silicide based alloys and reported that the synergy of Ti + Ge caused macrosegregation of Si and stabilise Nb_{ss} + Ti_5Si_3 eutectic (Ti_5Si_3 has unwanted hexagonal hP16 structure, isomorphous with γNb_5Si_3). Ge is less effective in destabilisation of Nb_3Si (the latter is formed only in ZF3). According to Zifu and Tsakiropoulos (2010, 2011) βNb_5Si_3 is the primary solidification phase in all the three alloys (ZF1, ZF2 and ZF3). Ge partitioned to βNb_5Si_3 and its solubility depends on its concentration in the nominal alloy composition (Zifu and Tsakiropoulos, 2010).

Molybdenum and tungsten partition to Nb_{ss} and can reduce the Si solubility in it to zero (Grammenos and Tsakiropoulos, 2011), with improvement in fracture toughness. The latter depends on Mo and W content. Hf has no significant effect on Si solubility in the Nb_{ss}. In the alloy Nb-20Si-5Hf-5Mo-3W (YG8), Hf has opposite segregation behaviour with W in Nb_{ss} (i.e., increase in Hf results to a decrease in W). In the Nb_5Si_3, Hf has adverse effect on solubility of Mo and W. This effect is stronger on W which concentration is zero with Mo in as cast alloy (YG8) but while Mo exhibit some measurable concentration after heat treatment (1500 °C / 100 h), W remains zero.

The motivation for the work presented in this chapter was to study the synergistic effects of the refractory metals (RMs) Mo and W with Sn and Ge in the absence of Cr and Al on microstructure of Nb-11Ti-18Si-1Hf-6Mo-2.5W-xSn-xGe (x = 2 and 5) silicide based alloys.

3.2 Experimental

The nominal compositions of the alloys of this study are given in Table 2.1. The addition of 11 at%Ti was made to account for the adverse effect of this element on high temperature strength (Begley and Bechtold, 1961), and 1 at%Hf to account for adverse effect of Hf on high temperature strength retention. The additions of Mo and W were chosen as these elements are (i) known to improve the high temperature

strength of Nb, and (ii) change phase stability. The content of W (2.5 at%) was lower than that of Mo (6 at%) owing to the superior strengthening effect of the former element (Begley, 1994) and to balance strengthening with density. The concentration of Mo was chosen to balance strength and oxidation behaviour. The concentrations of Ge and Sn were chosen owing to the effects they have on vol% of Nb_{ss} and to evaluate the stability of A15 Nb_3Sn and the chemistry of Nb_{ss} (its Si content). Inaddition, the synergy of Ge and Sn is expected to counterbalance the anticipated negative effect of the synergy of low Ti content with the additions of Mo and W on oxidation behaviour. Both the Ge and Sn are important regarding the stability of Nb_3Si (Vellios and Tsakiropoulos, 2007, Zifu and Tsakiropoulos, 2010) and Sn is important regarding the formation A15 Nb_3Sn in the microstructure of Nb silicide based alloys (Vellios and Tsakiropoulos, 2007). The Si concentration (18 at%) was chosen to be in the range for achieving best creep behaviour (Bewlay et al., 2002).

The alloys were prepared, heat treated and characterised as described in Chapter 2.

3.3 Results

The densities of the alloys and %area of Nb_5Si_3 are given in Table 3.1. In the results, the phases suggested by the XRD using the ICDD data base were labelled in the diffractograms of Figures 3.1 and 3.4, and the EDS data presented in Table 3.3 to 3.6 with major substituting element(s).

In this chapter, A15 is used to mean cP8 $(Nb, Ti)_3Sn$ and/or $(Nb, Mo)_3Sn$. The phases present in the alloys were $(Nb, Mo)_{ss}$, $(Nb, Ti)_5Si_3$, HfO_2, with or without A15. TiN formed in BA6-HT. The $(Nb, Ti)_5Si_3$ appeared in β and / or α form. The crystal structure information and lattice parameters for the phases are given in Table 3.2.

Table 3.1 The nominal composition of the alloys BA1 and BA6, their densities and % area of Nb_5Si_3.

Nominal alloy composition (at %)	**Alloy code**	**Density (g/cm^3)**	**Nb_5Si_3 %area**	
			AC	**HT**
Nb-11Ti-18Si-1Hf-6Mo-2.5W-2Sn-2Ge	**BA1**	8.0	57	51
Nb-11Ti-18Si-1Hf-6Mo-2.5W-5Sn-5Ge	**BA6**	7.9	56	57

3.3.1 Nb-11Ti-18Si-1Hf-6Mo-2.5W-2Sn-2Ge (Alloy BA1)

3.3.1.1 As cast

The actual composition of the cast alloy (BA1-AC) was Nb-11.8Ti-17.3Si-1.0Hf-7.7Mo-2.4W-1.8Sn-1.8Ge. There was macrosegregation of Si, the concentration of which was in the range 16.3 at% to 19.1 at% see Table 3.3. The microstructure according to the XRD consisted of αNb_5Si_3, βNb_5Si_3 and Nb_{ss} (Figure 3.1a). These phases were confirmed by SEM with EDS analyses (Table 3.3). The presence of HfO_2 was confirmed by SEM (Figure 3.2f). In the XRD diffractogram, there were no peaks for Nb_3Si, γNb_5Si_3 and Nb_3Sn. The microstructure (Figure 3.2) consisted of anomalous eutectic of Nb_{ss} + Nb_5Si_3 at the very-bottom, primary Nb_5Si_3, anomalous and lamellae eutectics at the other parts of the ingot but with higher volume of the lamellar eutectic in the middle of the ingot. The average composition of the eutectic was Nb-10.0Ti-13.8Si-0.4Hf-9.8Mo-3.6W-1.7Sn-1.3Ge with Si+Sn+Ge = 16.8 at%. There were Ti-rich areas at edges of Nb_{ss} dendrites where the concentration of Ti was about 20 at%. According to the EDS analyses, some of the $(Nb, Mo)_{ss}$ grains contained no measurable amount of Si and their average composition was Nb-6.5Ti-0.1Hf-15.2Mo-8.3W-1.7Sn-0.5Ge**.** The $(Nb, Mo)_{ss}$ was rich in Mo and W with Mo+W = 23.5 at% and Mo/W = 1.8. There were also Ti-rich areas in the $(Nb, Ti)_5Si_3$ that were observed at the very bottom of the ingot with average composition Nb-15.1Ti-32.4Si-1.1Hf-2.5Mo-0.5Sn-3.3Ge with no detectable amount of W and Nb/(Ti+Hf) = 2.8. The lattice parameter of the bcc solid solution (3.2706 Å) was lower compared with pure Nb (3.303 Å) see Table 3.2. The c/a ratios of the $\alpha(Nb, Ti)_5Si_3$ and $\beta(Nb, Ti)_5Si_3$ were 1.8131 and 0.50297 respectively and were higher than unalloyed αNb_5Si_3 (1.809) and lower than unalloyed βNb_5Si_3 (0.506).

3.3.1.2 Heat treated

The actual composition of the heat treated specimen (BA1-HT) was Nb-12.0Ti-19.9Si-0.8Hf-5.6Mo-1.8W-1.9Sn-2.0Ge. Compared with BA1-AC, the difference in composition was attributed to chemical inhomogeneities in the cast alloy. According to Figure 3.1b, the phases present after the heat treatment were the αNb_5Si_3, Nb_3Sn and Nb_{ss}. These phases were confirmed by SEM with EDS analyses (Figure 3.3 and Table

3.4). The presence of HfO_2 was confirmed by the SEM (Figure 3.3). The microstructure had coarsened and the (Nb, Ti)$_3$Sn was formed and was linking (Nb, Mo)$_{ss}$ grains. Thus, the A15 (Nb, Ti)$_3$Sn was stabilised after the heat treatment. In the (Nb, Ti)$_3$Sn, the total sp elements content Si+Sn+Ge = 18.5 at%. Peaks for the βNb_5Si_3 were not observed in the diffractogram and therefore the β(Nb, Ti)$_5Si_3$ had completely transformed to α(Nb, Ti)$_5Si_3$. Thus the equilibrium microstructure of BA1 consisted of (Nb, Mo)$_{ss}$, (Nb, Ti)$_3$Sn and α(Nb, Ti)$_5Si_3$. In the α(Nb, Ti)$_5Si_3$, the Si+Sn+Ge was 37.6 at% and was in agreement with the Si content of the Nb_5Si_3 in the Nb-Si phase diagram (37.5 at%) (Okamoto et al., 1990).

Furthermore, all the α(Nb, Ti)$_5Si_3$ grains analysed contained (on average) no measurable amount of W. According to the EDS analyses, (Nb, Mo)$_{ss}$ with no Si and "normal" (Nb, Mo)$_{ss}$ (i.e., the (Nb, Mo)$_{ss}$ containing Si) were present. In the (Nb, Mo)$_{ss}$ there was a decrease in Mo+W and increase in Mo/W after the heat treatment. The α(Nb, Ti)$_5Si_3$ was richer in Ti and Ge than the (Nb, Ti)$_3$Sn and the (Nb, Mo)$_{ss}$ was richer in Mo, Ti and W than the (Nb, Ti)$_3$Sn. The increase and/or decrease in the lattice parameters of the phases after heat treatment were due to solute redistribution. Hafnia particles were observed near the surface and bottom of BA1-HT.

3.3.2 Nb-11Ti-18Si-1Hf-6Mo-2.5W-5Sn-5Ge (Alloy BA6)

3.3.2.1 As cast

The actual composition of the cast alloy (BA6-AC) was Nb-10.8Ti-17.4Si-1.1Hf-6.1Mo-2.0W-4.0Sn-5.3Ge. There was weak macrosegregation of Si. According to Figure 3.4a the phases present are the Nb_3Sn, βNb_5Si_3 and Nb_{ss}. These phases were confirmed by SEM with EDS analyses (Figure 3.5 and Table 3.5). The Figure 3.5 also confirmed the presence of HfO_2. The percentage area of the β(Nb, Ti)$_5Si_3$ was 56%. In the β(Nb, Ti)$_5Si_3$ the Si+Sn+Ge was 36.7 at% and the Nb/(Ti+Hf) = 6.1. No peaks of αNb_5Si_3, (tP32) Nb_3Si or (hP16) γNb_5Si_3 were observed in the XRD diffractogram. The entire analysed (Nb, Mo)$_{ss}$ grains contained Si.

The scale (size) of the A15 increased from the very-bottom and very-top to the middle of the ingot see Figure 3.5. The average composition of the (Nb, Ti)$_3$Sn in the top-half (from very-top to the middle) of the ingot was Nb-12.2Ti-4.4Si-0.6Hf-8.2Mo-2.5W-10.3Sn-3.7Ge with Si+Sn+Ge = 18.4 at% and (Si+Ge)/Sn = 0.8. Notice the difference

in the Si/Sn = 0.4 with Si/Sn ~ 1(0.8) in the bottom-half of the ingot in Table 3.5. The differences in the concentration of Ti and W with those in the latter table were also significant. For the $(Nb, Mo)_3Sn$ in the bottom-half of the specimen, the average Si+Sn+Ge was 16.8 at% and the (Si+Ge)/Sn was 1.3.

The %area of the eutectic increased from the bottom to the top of the ingot. The average composition of the eutectic was Nb-11.6Ti-10.5Si-1.0Hf-8.7Mo-3.6W-4.1Sn-4.6Ge. This was a ternary eutectic consisting of Nb_{ss} + Nb_3Sn + βNb_5Si_3 with Si+Sn+Ge = 19.2 at%. In the ternary eutectic, the Nb_{ss} and Nb_3Sn were co-continuous.

In the middle of the ingot, it was difficult to confirm the presence of the Nb_{ss} by EDS (see Figure 3.5e). The eutectic in the bottom-half of the ingot had similar composition with those in the top-half of the ingot.

The lattice parameters of the $(Nb, Mo)_{ss}$, A15 and c/a ratio of the $\beta(Nb, Ti)_5Si_3$ were less than the unalloyed phases (Table 3.2).

3.3.2.2 Heat treated

The actual composition of the heat treated specimen (BA6-HT) was Nb-11.0Ti-17.6Si-1.0Hf-5.7Mo-1.9W-4.3Sn-5.9Ge. The microstructure according to Figures 3.4b, 3.6 and Table 3.6 consisted of $\alpha(Nb, Ti)_5Si_3$, $(Nb, Ti)_3Sn$, $(Nb, Mo)_{ss}$, HfO_2 and TiN. The absence of βNb_5Si_3 in Figure 3.4b means that $\beta Nb_5Si_3 \rightarrow \alpha Nb_5Si_3$ transformation had been completed. The %area of the 5-3 silicide was 57%. There were bright contrast precipitates in the 5-3 silicide phase (Figure 3.6). In the $(Nb, Ti)_3Sn$ the Si+Sn+Ge were 18.8 at% and the (Si+Ge)/Sn ratio was ~ 0.5. The $(Nb, Mo)_{ss}$ contained no Si and the Mo+W content had increased significantly compared with the BA6-AC (from 19 at% to 36.8 at%, and the ratio Mo/W had decreased slightly from 2.1 to 1.7). The microstructure was contaminated near the surfaces of the specimen where TiN had formed Figure 3.6d.

The lattice parameter of the bcc $(Nb, Mo)_{ss}$ decreased while that of the A15 increased after the heat treatment. The a, c lattice parameters and the c/a ratio of the $\alpha(Nb, Ti)_5Si_3$ were larger than those of the unalloyed αNb_5Si_3. The heat treated specimen showed two distinct contrasts after grinding and polishing. That is, from the very-

Table 3.2 The crystal structures of phases and their lattice parameters in the BA1 and BA6 alloys.

Alloy code	Phase	Pearson symbol	Lattice parameters (Å)									
			As cast			Heat treated			Reference values			
									a	c	c/a	ICDD
			a	c	c/a	a	c	c/a				
BA1	Nb_{ss}	cI2	3.2706	-	-	3.2715	-	-	3.303	-	-	00-034-0370
	αNb_5Si_3	tI32	6.58	11.93	1.8131	6.5619	11.922	1.8169	6.5698	11.887	1.809	00-030-0874
	βNb_5Si_3	tI32	10.0416	5.0506	0.50297	-	-	-	10.028	5.0698	0.506	00-030-0875
	Nb_3Sn	cP8	-	-	-	5.1745	-	-	5.295	-	-	04-004-7714
BA6	Nb_{ss}	cI2	3.2654	-	-	3.2381	-	-	3.303	-	-	00-034-0370
	αNb_5Si_3	tI32	-	-	-	6.579	11.929	1.8132	6.5698	11.887	1.809	00-030-0874
	βNb_5Si_3	tI32	10.0687	5.0599	0.5025	-	-	-	10.028	5.0698	0.506	00-030-0875
	Nb_3Sn	cP8	5.1748	-	-	5.2899	-	-	5.295	-	-	04-004-7714

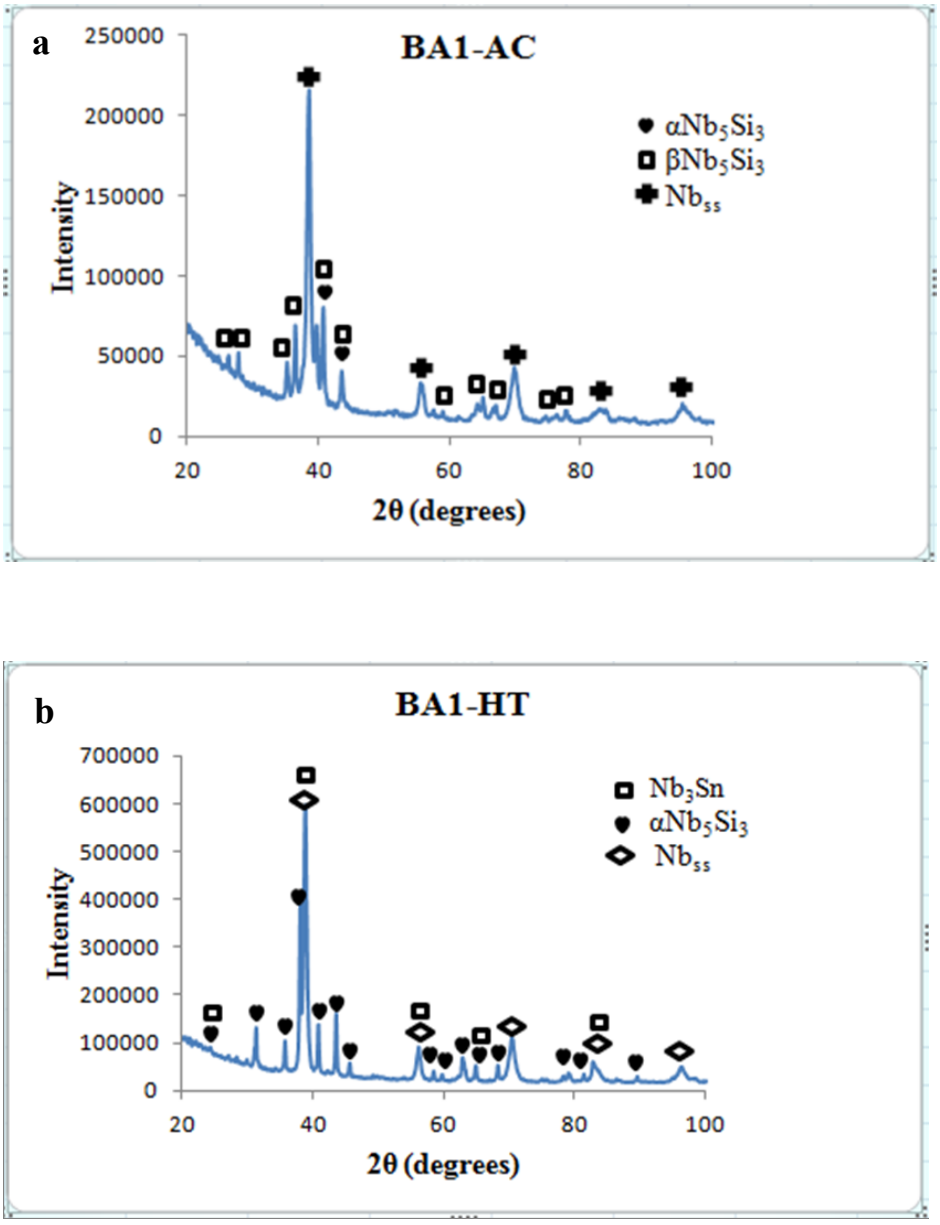

Figure 3.1 X-ray diffractograms of the alloy BA1 (a) as cast, (b) heat treated.

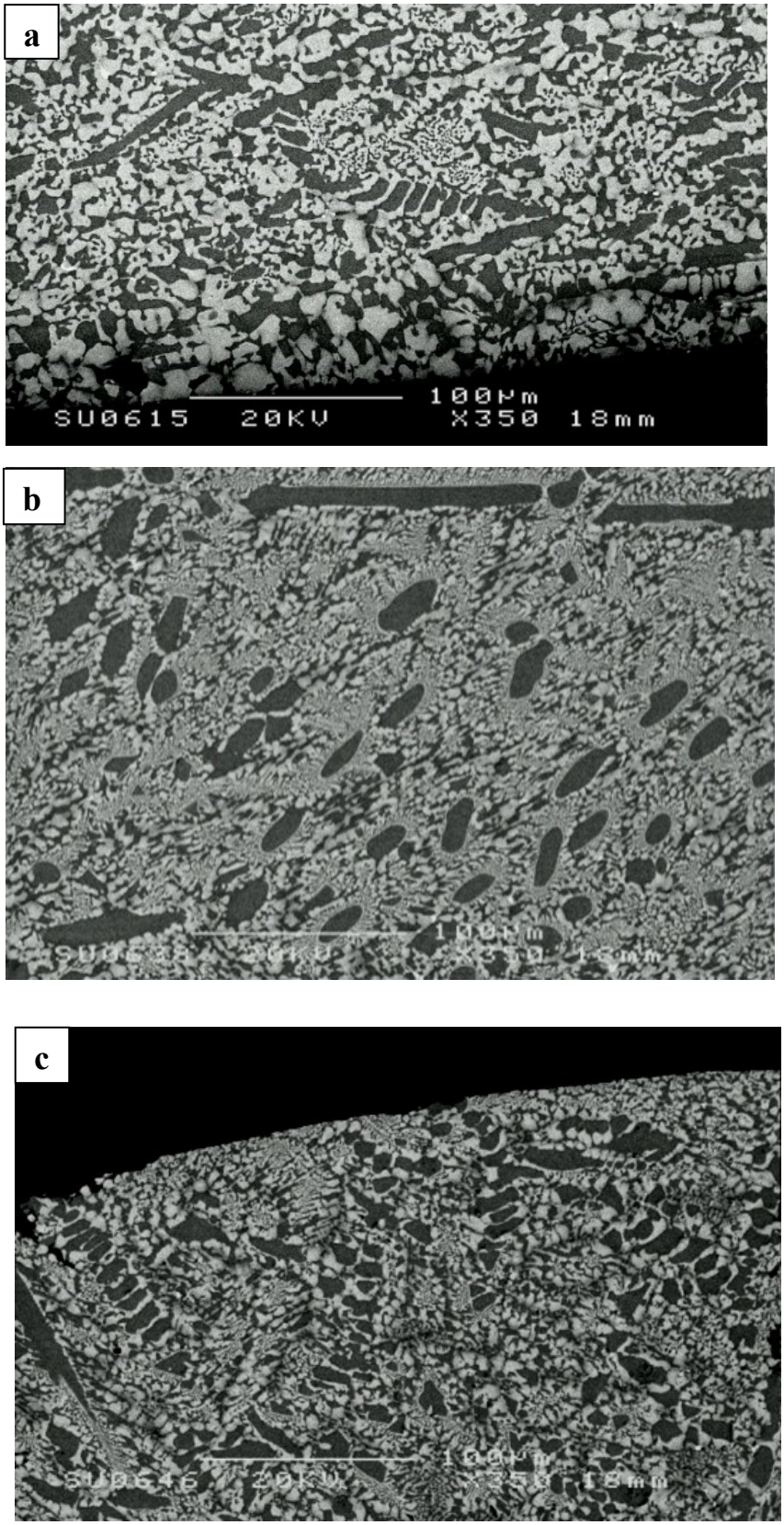

Figure 3.2 continues on next page.

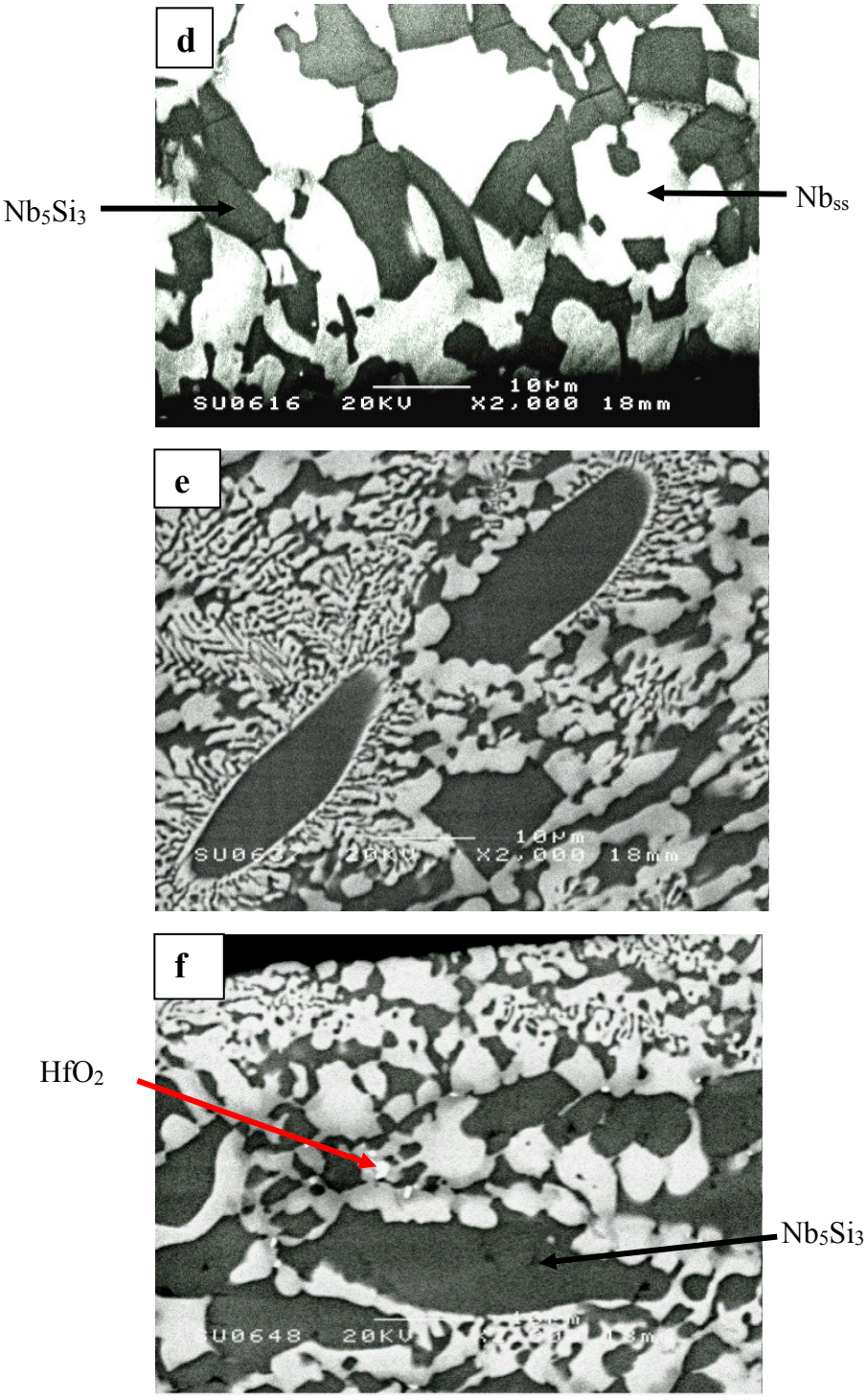

Figure 3.2 Backscattered electron micrographs of the alloy BA1-AC (a to c) bottom, middle and top, (d to f) from same area but at higher magnification where (d) shows the microstructure at the very bottom of the ingot. In d, e, and f the dark contrast phase is the $(Nb, Ti)_5Si_3$ and the light grey contrast at the edges of the $(Nb, Mo)_{ss}$ is Ti-rich.

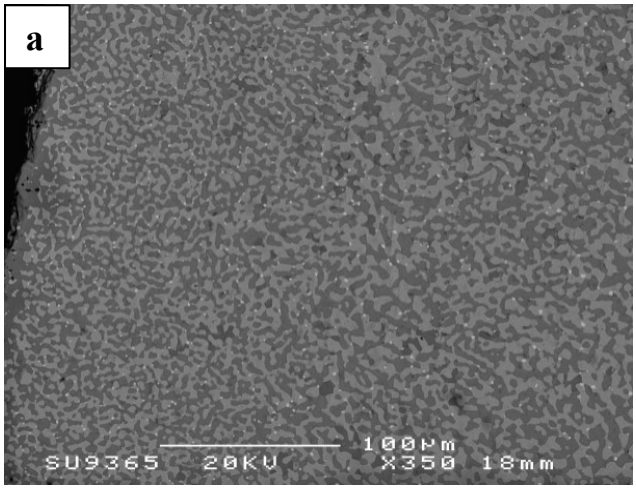

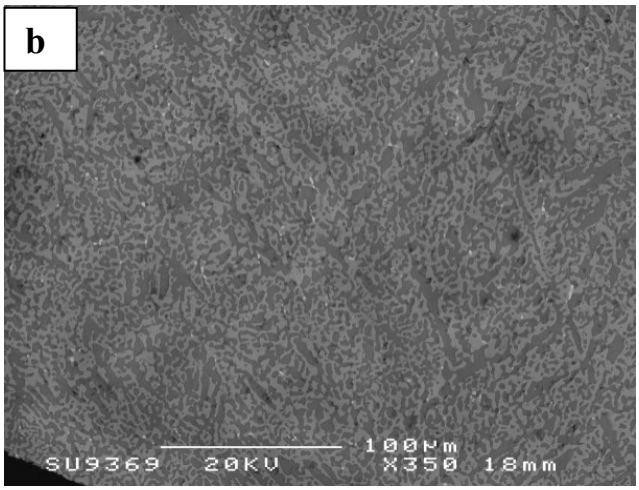

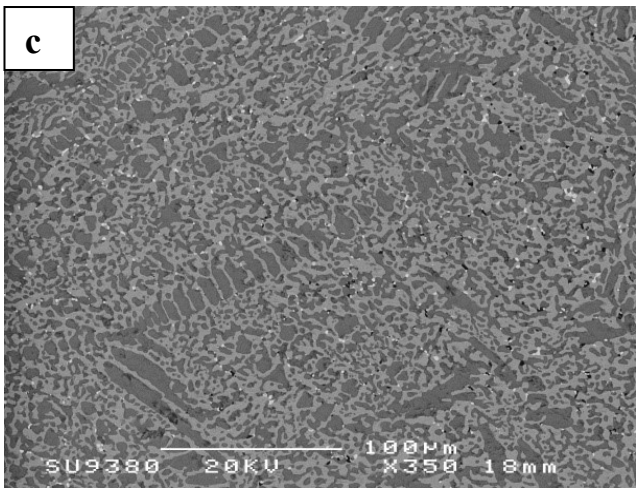

Figure 3.3 continues on next page.

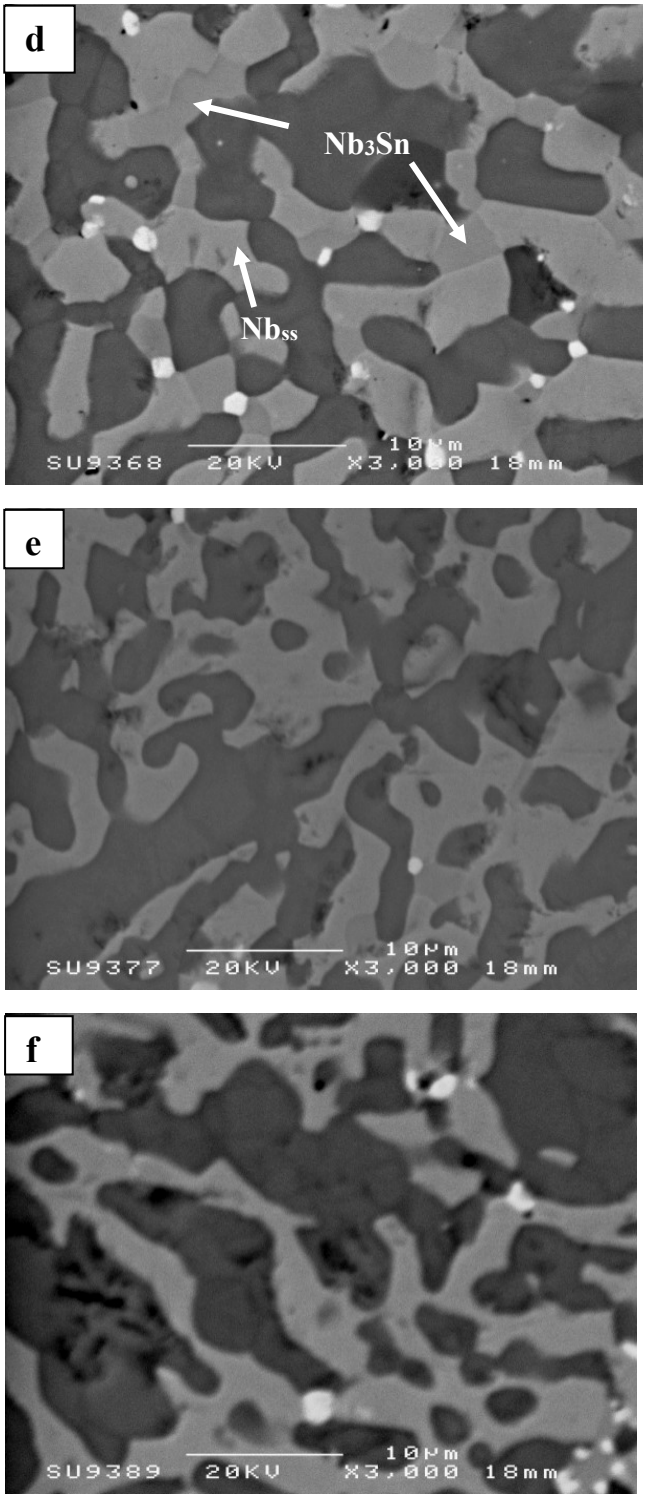

Figure 3.3 Backscattered electron micrographs of the alloy BA1-HT (a to c) bottom, middle and top, (d to f) is from the same area but at higher magnification. The white contrast phase is hafnia.

Table 3.3 Chemical analyses (at%) for bulk and phase compositions in alloy BA1-AC.

Part of the ingot/ Phase	Element (at%)							
	Nb	**Ti**	**Si**	**Hf**	**Mo**	**W**	**Sn**	**Ge**
Bottom	55.7±0.5 55.1-56.3	11.8±0.5 11.1-12.4	18.0±0.7 17.3-19.1	0.9±0.1 0.8-1.0	7.7±0.3 7.4-8.1	2.4±0.3 2.1-2.8	1.7±0.2 1.5-1.9	1.8±0.2 1.6-2.0
Middle	56.6±0.6 55.7-57.2	11.7±0.3 11.3-12.1	16.8±0.5 16.3-17.5	1.0±0.1 0.8-1.2	7.8±0.4 7.2-8.2	2.5±0.2 2.3-2.9	1.9±0.1 1.8-2.1	1.7±0.2 1.5-2.0
Top	56.5±0.5 55.9-57.0	11.8±0.1 11.7-12.0	17.0±0.5 16.3-17.4	1 .0±0.1 0.8-1.1	7.7±0.2 7.5-7.9	2.4±0.2 2.2-2.7	1.8±0.1 1.8-2.0	1.8±0.1 1.7-2.0
$(Nb, Ti)_5Si_3$	50.5±0.4 49.9–51.3	8.6±0.2 8.2–9.0	33.7±0.5 32.2-34.7	0.3±0.1 0 .1-0.5	3.0±0.2 2.8-3.4	0.4±0.2 0.1-0.7	0.8±0.1 0.6–1.0	2.7±0.1 2.4–2.9
$(Nb, Mo)_{ss}$	65.2±0.6 64.5-66.2	7.2±0.6 6.3–8.2	1.7±0.6 0.7–2.7	0.2 0.0–0.4	16.0±0.5 15.2-16.9	7.4±0.6 6.1–8.2	1.8±0.2 1.5–2.2	0.5±0.1 0.3–0.7
Eutectic	59.4±0.4 58.6-60.1	10.0±0.5 9.1-10.7	13.8±0.9 12.1-14.9	0.4±0.2 0.1-0.7	9.8±0.5 9.1-11.0	3.6±0.2 3.1-3.9	1.7±0.3 1.3-2.1	1.3±0.2 0.9-1.5

Table 3.4 Chemical analyses (at%) for bulk and phase compositions in alloy BA1-HT.

Part of the ingot / Phase	Element (at%)							
	Nb	**Ti**	**Si**	**Hf**	**Mo**	**W**	**Sn**	**Ge**
Bottom	55.8 ±0.4 55.5-56.3	11.9±0.5 11.3-12.6	20.0±0.4 19.4-20.5	0.8±0.1 0.7-1.0	5.8±0.3 5.5-6.2	1.9±0.1 1.8-2.1	1.9±0.1 1.8-2.1	1.9±0.3 1.5-2.2
Middle	55.7±0.5 55.0-56.4	12.2±0.1 12.1-12.3	19.9± 0.6 19.3-20.6	0.8±0.1 0.7-0.9	5.6±0.2 5.4-5.9	1.8±0.2 1.6-2.1	2.0±0.2 1.8-2.2	2.0 ±0.2 1.9-2.2
Top	56.3 ±0.3 56.2-57.0	12.0 ±0.2 11.7-12.3	19.8 ±0.1 19.7-19.8	0 .8±0.1 0.6-0.8	5.4 ±0.2 5.2-5.6	1.8 ±0.1 1.7-1.9	1.9±0.1 1.7-2.3	2.0±0.3 1.7-2.3
$(Nb, Ti)_5Si_3$	49.9±0.4 49.3-50.5	10.0±0.6 9.0-10.9	34.1±0.5 33.2-34.9	0.6±0.2 0.3-0.9	1.9±0.3 1.4-2.5	0-0.2	0.8±0.1 0.7-1.1	2.7±0.3 2.2-3.1
$(Nb, Mo)_{ss}$	68.6±0.8 65.7-70.5	11.0±0.9 9.2-12.0	0.8±0.8 0.2-2.5	0-0.3	11.2±0.7 10.2-12.7	5.0±0.4 4.4-5.7	2.7±0.2 2.5-3.0	0.7±0.4 0.2-1.2
$(Nb, Mo)_{ss}$ (no Si)	69.7±1.3 68.5-71.6	10.1±1.7 8.0-11.7	0	0	12.0±0.8 10.9-12.8	5.2±0.1 5.0-5.3	2.4±0.2 2.2-2.8	0.6±0.2 0.3-1.0
$(Nb, Ti)_3Sn$	65.9±0.3 65.3-66.5	7.8±0.3 7.3-8.2	1.4±0.1 1.2-1.7	0-0.3	5.1±0.3 4.6-5.7	2.7±0.3 2.4-3.2	16.0±0.4 15.4-16.4	1.1±0.2 0.8-1.5

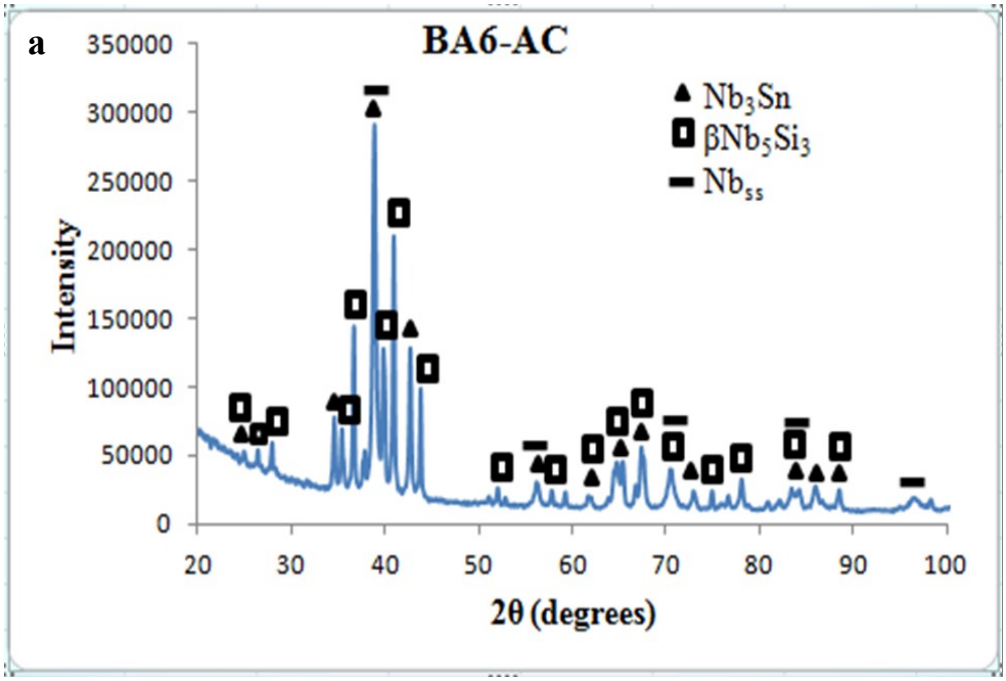

Figure 3.4 X-ray diffractograms of the alloy BA6 (a) as cast and (b) heat treated.

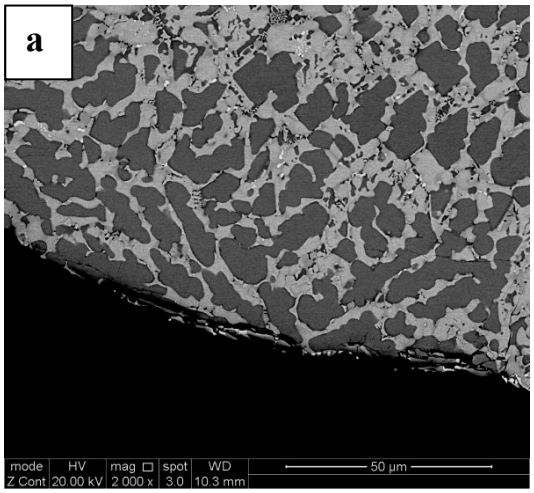

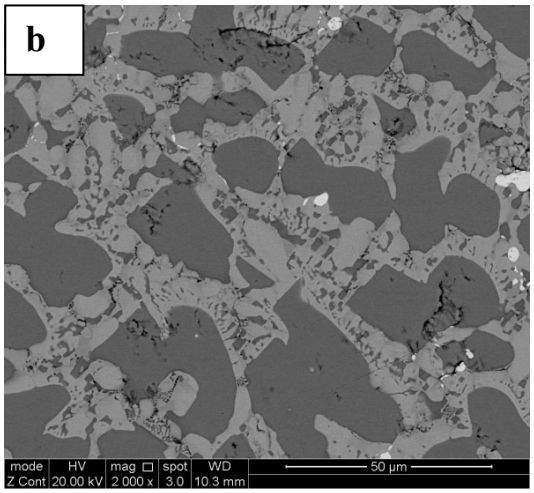

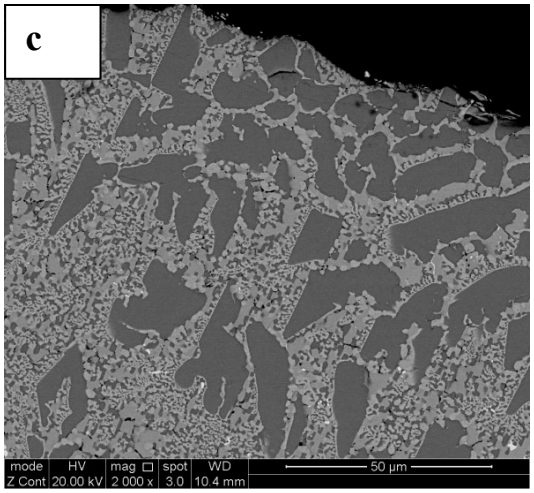

Figure 3.5 continues on next page.

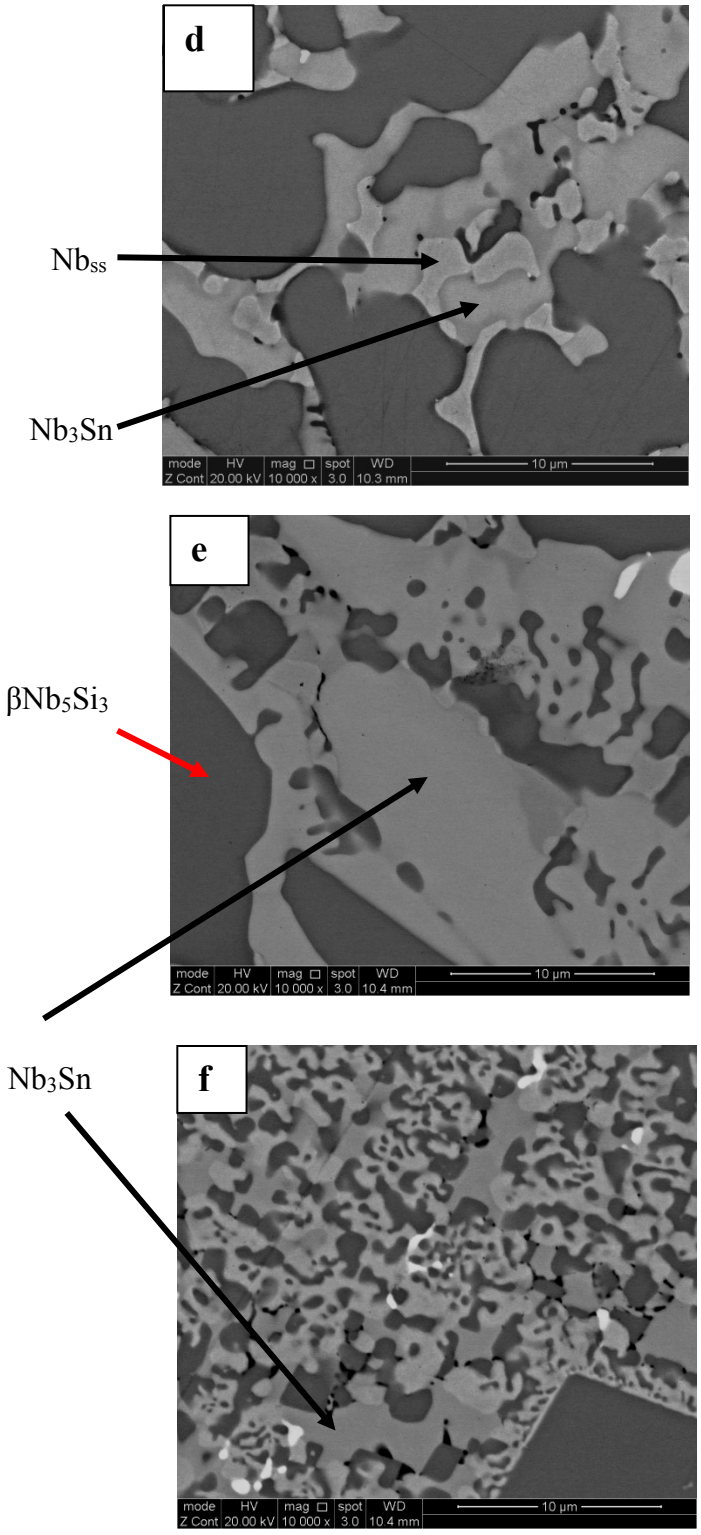

Figure 3.5 Backscattered electron micrographs of the alloy BA6-AC (a to c) bottom, middle and top; (d to f) same area at higher magnification. The white contrast phase is hafnia.

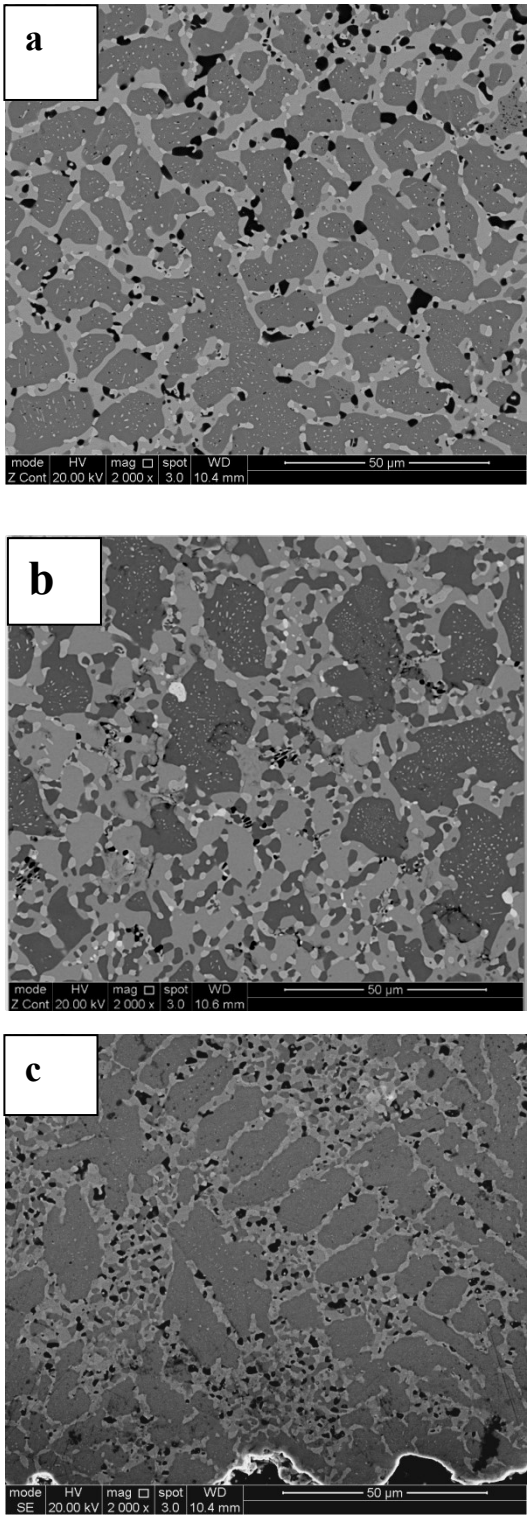

Figure 3.6 continues on next page.

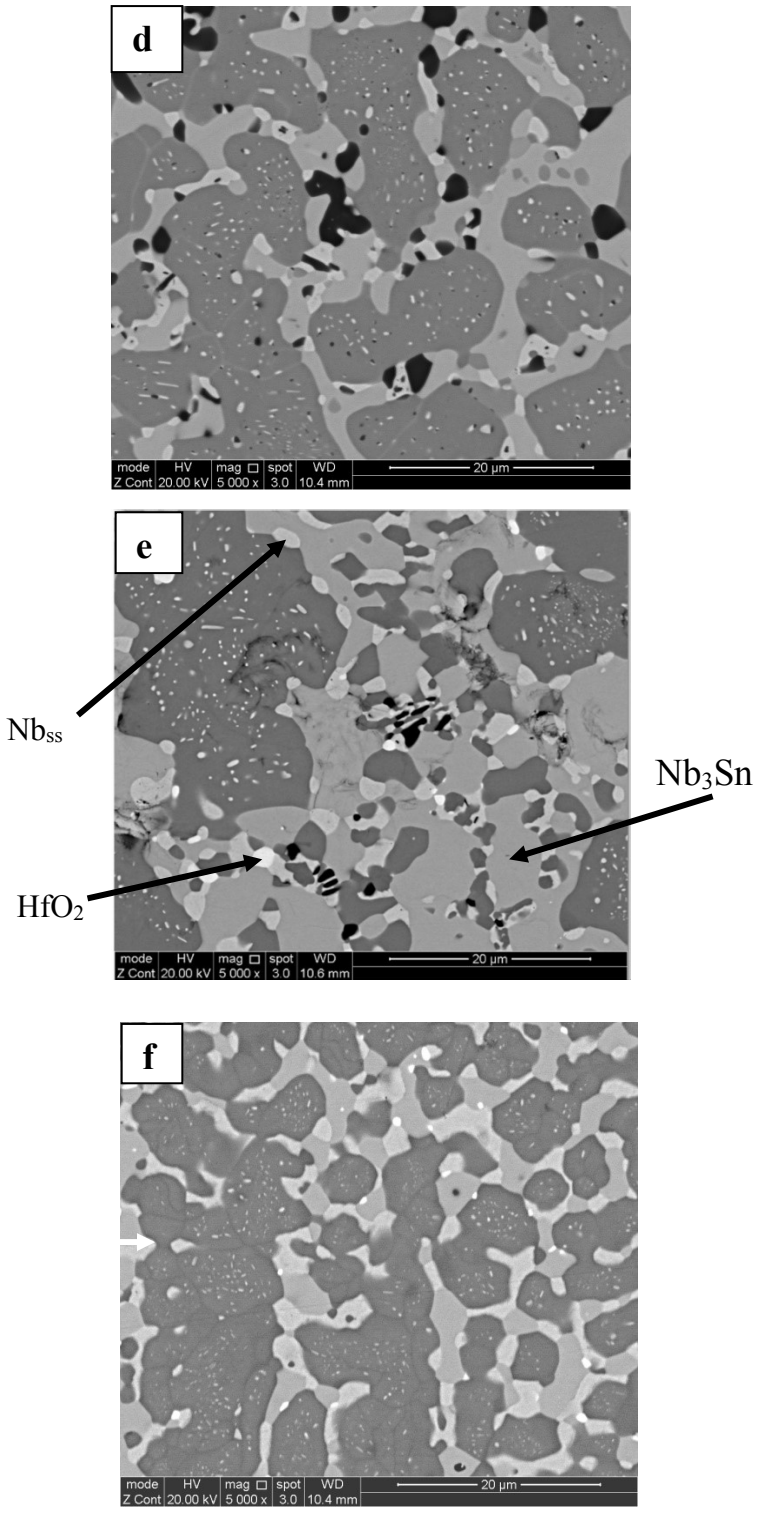

Figure 3.6 Backscattered electron micrographs of the alloy BA6-HT (a to c) bottom, middle and top at low magnification; (d) bottom, (e) middle and (f) a localised microstructure in the middle (top part of the ingot). The dark con-

contrast phase in (a) and (d) is TiN.

Table 3.5 Chemical analyses (at%) for bulk and phase compositions in the alloy BA6-AC.

Part of ingot / phase	Elements (at%)							
	Nb	**Ti**	**Si**	**Hf**	**Mo**	**W**	**Sn**	**Ge**
Bottom	52.3±0.7 51.5-53.4	10.9±0.3 10.5-11.3	17.9±0.4 17.2-18.2	1.0±0.1 0.9-1.1	6.0±0.5 5.5-6.6	2.0±0.1 1.9-2.2	4.5±0.2 4.3-4.8	5.4±0.2 5.1-5.7
Middle	53.7±0.3 53.3-53.9	10.9±0.1 10.8-11.1	17.0±0.2 16.8-17.2	1.2±0.2 0.9-1.4	6.3±0.2 6.0-6.6	2.0±0.1 1.9-2.2	3.8±0.2 3.7-4.1	5.1±0.2 5.0-5.5
Top	53.6±0.2 53.3-53.8	10.6±0.2 10.4-10.8	17.4±0.2 17.0-17.6	1.1 1.1-1.1	6.1±0.3 6.0-6.5	2.0±0.2 1.7-2.2	3.7±0.1 3.6-3.8	5.5±0.2 5.3-5.9
$(Nb, Ti)_5Si_3$	51.4±0.4 50.8-52.1	7.7±0.3 7.3-8.2	28.5±0.4 28.0-29.3	0.7±0.1 0.5-0.9	2.9±0.3 2.4-3.4	0.6±0.2 0.4-0.9	1.2±0.1 0.9-1.4	7.0±0.5 5.9-7.8
$(Nb, Mo)_{ss}$	62.0±0.5 61.1-62.8	11.4±0.9 10.8-13.2	1.3±0.4 0.9-2.0	0.6±0.2 0.3-0.8	12.8±0.6 11.6-13.7	6.2±0.3 5.5-6.7	4.0±0.3 3.5-4.4	1.7±0.7 0.6-2.7
$(Nb, Mo)_3Sn$*	60.5±0.6 59.3-61.4	8.1±0.4 7.6-8.7	5.8±0.4 5.2-6.7	0.4±0.2 0-0.7	9.5±0.4 8.9-10.4	4.7±0.2 4.4-5.0	7.2±0.6 6.7-8.3	3.8±0.4 3.1-4.7
Eutectic	55.9±1.1 54.3-57.1	11.6±0.9 10.7-13.8	10.5±0.6 9.6-11.6	1.0±0.4 0.7-1.7	8.7±0.7 7.5-9.6	3.6±0.6 2.5-4.1	4.1±0.8 3.5-5.5	4.6±0.3 3.9-5.0

*This is the average composition of the A15 phase in the bottom half of the ingot.

Table 3.6 Chemical analyses (at%) for bulk and phase compositions in the alloy BA6-HT

Part of ingot / phase	**Elements (at%)**							
	Nb	**Ti**	**Si**	**Hf**	**Mo**	**W**	**Sn**	**Ge**
Middle	52.6±0.3 52.1-53.0	11.0±0.2 10.9-11.3	17.6±0.3 17.3-18.1	1.0±0.2 0.9-1.2	5.7±0.3 5.3-6.1	1.9±0.1 1.9-2.1	4.3±0.5 3.8-4.9	5.9±0.5 5.5-6.7
$(Nb, Ti)_5Si_3$	51.2±0.9 49.7-52.3	9.0±0.8 8.2-10.3	27.9±0.9 26.1-29.0	0.7 0.4-0.9	2.5±0.4 1.8-3.9	0.3 0-0.8	1.6±0.1 1.4-1.8	6.8±0.4 6.1-7.5
$(Nb, Mo)_{ss}$ (no Si)	54.0±0.6 53.1-54.9	6.3±0.5 5.7-7.3	0	0.2 0-0.6	23.4±0.7 22.3-24.4	13.4±0.4 12.6-14.0	1.2±0.2 0.9-1.6	1.5±0.4 0.7-2.0
$(Nb, Ti)_3Sn$	58.0±0.4 57.4-58.6	11.9±0.3 11.6-12.4	2.9±0.3 2.5-3.3	0.2 0-0.7	8.7±0.4 8.0-9.2	2.4±0.1 2.1-2.6	12.8±0.3 12.1-13.2	3.1±0.2 2.7-3.4

bottom to the centre of the specimen, there was a different contrast compared with the very-top to the centre. However, SEM studies with EDS analyses did not provide clear evidence as to the cause of the two contrasts in the specimen after the heat treatment. However, there was localized finer microstructure in the middle upper part of the specimen (see Figure 3.6f).

3.4 Discussion

The synergistic effects of Mo and W with Sn and Ge on phase selection, stability and the chemistry of Nb_{ss} in the Nb-Ti-Si-Hf-Mo-W-Sn-Ge system could be highlighted by comparing the alloys Nb-11Ti-18Si-1Hf-6Mo-2.5W-2Sn-2Ge (BA1) with Nb-11Ti-18Si-1Hf-6Mo-2.5W-5Sn-5Ge (BA6), and simpler alloys with or without Mo, W, Sn or Ge.

3.4.1 As cast

3.4.1.1 Phases present in the cast alloys

The phases present in the cast alloys BA1-AC and BA6-AC were the $(Nb, Mo)_{ss}$, $\alpha(Nb, Ti)_5Si_3$, $\beta(Nb, Ti)_5Si_3$ and HfO_2, and $(Nb, Mo)_{ss}$, $\beta(Nb, Ti)_5Si_3$, A15 and HfO_2, respectively (see Figures 3.1, 3.2, 3.4 and 3.5, and Tables 3.3 and 3.5). The A15 phase was absent in BA1-AC and the $\alpha(Nb, Ti)_5Si_3$ in the BA6-AC. According to phase equilibria, in the Mo–Si system (Figure 1.15) the Mo_5Si_3 is isomorphous with βNb_5Si_3; in the Si–W system (Figure 1.17) the W_5Si_3 is isomorphous with the βNb_5Si_3. According to Sun et al. (2012) αNb_5Si_3 formed in place of βNb_5Si_3 in the alloy Nb-18Si-5Sn. The Mo+W contents of the $(Nb, Ti)_5Si_3$ were the same in BA1-AC and BA6-AC, but the Ge content was different and was higher in BA6-AC. Germanium forms Nb_5Ge_3 (Figure 1.21) isomorphous with βNb_5Si_3. According to Zifu and Tsakiropoulos (2010) the βNb_5Si_3 was formed in the cast Nb-18Si-5Ge alloy but both βNb_5Si_3 and Ti_5Si_3 in the Nb-24Ti-18Si-5Ge . In the BA1-AC, both the $\alpha(Nb, Ti)_5Si_3$ and $\beta(Nb, Ti)_5Si_3$ were observed whereas only the latter was observed in the BA6-AC. In the BA1-AC, the synergy of Ge with Mo and W could not completely suppress the destabilising effect of Sn on the $\beta(Nb, Ti)_5Si_3$. The absence of $\alpha(Nb, Ti)_5Si_3$ in BA6-AC could be attributed to the increase in Ge content of the 5-3 silicide. Either this

made the $\beta Nb_5Si_3 \rightarrow \alpha Nb_5Si_3$ transformation promoted by Sn very sluggish or the increase in Ge enhanced the stabilising effect of Mo and W on βNb_5Si_3.

According to Vellios and Tsakiropoulos (2007b), (i) the Nb_3Sn formed in the Nb-18Si-5Sn (NV9) alloy with Si/Sn ~ 1 and Si+Sn ~ 17.8 at%, and (ii) the 24 at%Ti addition in the Nb-24Ti-18Si-5Sn (NV6) alloy did not suppress the formation of the Nb_3Sn in the cast alloy. The Nb_3Sn was not observed in BA1-AC but was formed in BA6-AC, where the Sn and Ge were higher, and had (Si+Ge)/Sn = 1.3 or 0.8, and Si+Ge+Sn = 16.8 at% or 18.4 at% respectively. The Nb_3Sn and Nb_3Ge are A15 compounds and thus Ge can substitute for Sn and promote formation of A15 Nb_3Sn.

The data for BA1-AC suggest that 1.8 at%Sn was not enough to form A15 phase during solidification.

The data for BA6-AC suggest that 4 at%Sn was more than enough to form the A15 phase during solidification if a balance in vol% with Nb_{ss} were desired in the alloy.

Thus the critical amount of Sn required for formation of the Nb_3Sn in the cast alloy of BA alloys presented in this chapter is in the range 1.8 at% < Sn < 4 at%, and Sn/Ge < 1.

3.4.1.2 Microstructures of the cast alloys

The microstructures of BA1-AC and BA6-AC (Figures 3.2 and 3.5) essentially consisted of two- and three- phase microstructure respectively. Unlike the small volume fraction of fine eutectic observed at the bottom, very top and top of BA1-AC, large volume fraction was observed in the middle of the ingot. In BA1-AC, the Nb_{ss} + Nb_5Si_3 eutectic had average composition Nb-10.0Ti-13.8Si-0.4Hf-9.8Mo-3.6W-1.7Sn-1.3Ge with Si+Sn+Ge = 16.8 at%. In BA6-AC, the Nb_{ss} + Nb_3Sn + βNb_5Si_3 ternary eutectic had average composition Nb-11.6Ti-10.5Si-1.0Hf-8.7Mo-3.6W-4.1Sn-4.6Ge with Si+Sn+Ge = 19.2 at%. Unlike the BA1-AC, the eutectic in BA6-AC was observed in large volume at the top of the ingot.

The formation of Nb_{ss} + Nb_5Si_3 eutectic in BA1-AC instead of the Nb_{ss} + Nb_3Si eutectic was attributed (i) to the presence and synergy of Mo and W in the alloy with Mo+W = 8.5 at%, which was expected to suppress the Nb_{ss} + Nb_3Si eutectic as discussed in Chapter 1, (ii) to the presence of Sn which suppressed the Nb_3Si

formation (supported by results of Sun et al. (2012)), and synergy of Sn and Ti in the alloy, supported by the results of Vellios and Tsakiropoulos (2007b), and (iii) to the presence of Ge, supported by the results of Zifu and Tsakiropoulos (2010). The formation of the ternary eutectic in BA6-AC was attributed to increase in Sn concentration, supported by Sun et al. (2012).

The aforementioned compositions of the eutectics in BA1-AC and BA6-AC showed (i) that the Si contents were lower than that in the Nb-Si binary (18.2 at% see Figure 1.2 in Chapter 1), (ii) that the Si content decreased further in BA6-AC as the concentrations of Sn and Ge increased, and (iii) that the W content of the eutectic did not change. Vellios and Tsakiropoulos (2007b) showed that the synergy of Sn and Ti decreased the Si content of the eutectic from 18 at% in Nb-18Si-5Sn (alloy NV9) to 16.3 at% in Nb-24Ti-18Si-5Sn (alloy NV6) while keeping the Si+Sn to about 20.5 at% in both alloys. Zifu and Tsakiropoulos (2010) showed that Ge decreased the Si content of the eutectic to 13.6 at% in Nb-18Si-5Ge (alloy ZF1) to 9.3 at% in Nb-18Si-10Ge (alloy ZF2) while keeping the Si+Ge to about 17.6 at% as the Ge content in the alloy increased. Grammenos and Tsakiropoulos (2011) showed that the Si content in the eutectics in Nb-20Si-5Mo-3W (alloy YG6) and Nb-20Si-5Hf-5Mo-3W (alloy YG8) was the same or slightly above the bulk Si content. Thus, the lower Si contents of the eutectics in BA1-AC and BA6-AC could be attributed to the effects of Si and Ge.

The transition in microstructure observed in the bottom of BA1-AC (see Figure 3.2a and d) have been observed in Nb-18Si-5Ge (alloy ZF1), Nb-18Si-10Ge (alloy ZF2) (Zifu and Tsakiropoulos, 2010) and Nb-19Si-5Mo (Chattopadhyay et al., 2007). The latter attributed their formation to the synergy of high Si concentration and undercooling. High concentration of Si compared with the bulk and top was indeed the case in BA1-AC (Table 3.3).

Transitions in eutectics from anomalous to regular eutectic occur with decreasing melt undercooling ΔT and the microstructure generally consists of solid solution with an intermetallic. In anomalous eutectics one phase is continuous. In the bottom of BA1-AC the coarse microstructure consisted of Nb_{ss} with Nb_5Si_3. The two phases have different crystal structures and entropies of fusion and thus would require different "kinetic undercooling" (Abbaschian and Lipschutz, 1997). In unrestrained

solidification of eutectic melts with decreasing melt undercooling, a transition can occur from entirely anomalous eutectic to a mixture of regular and anomalous eutectic to regular eutectic (Han and Wei, 2002).

The microstructure in the bottom of the ingot of BA1-AC could be explained as follows: The melt in contact with the water cooled crucible was undercooled above some critical value $\Delta T_{critical} \sim 0.25\Delta T_{max}$, where $\Delta T_{critical}$ and ΔT_{max} are respectively the critical undercooling for the formation of anomalous eutectic and the maximum undercooling achievable in the eutectic system (Li and Kuribayashi, 2003). At $\Delta T > \Delta T_{critical}$ the growth rates for the Nb_{ss} and Nb_5Si_3 were different with the solid solution phase growing faster than the silicide (simpler structure and lower entropy of fusion for the Nb_{ss}). This led to decoupled growth of the two phases of the eutectic and resulted to the anomalous microstructure. However, as the latter grew the temperature of the melt ahead of the solid/liquid interface (S/L) increased because of the released latent heat of solidification and this resulted to lower growth rates and eventually coupled growth between the two phases, thus forming the regular eutectic.

In the BA1-AC alloy, there were (i) Ti-rich area at the edges of the solid solution with about 20 at%Ti, (ii) $(Nb, Mo)_{ss}$ with Mo+W = 23.4 at% and Mo/W = 2.2, and (iii) $(Nb, Mo)_{ss}$ with no Si. The average composition of the latter was Nb-6.5Ti-0.1Hf-15.2Mo-8.3W-1.7Sn-0.5Ge with Mo+W = 23.5 at% and Mo/W = 1.8.

In the BA6-AC, all the $(Nb, Mo)_{ss}$ analysed contained Si and had Mo+W = 19 at% and Mo/W = 2.1. Using the normal $(Nb, Mo)_{ss}$ to make comparisons, increase in the concentrations of Sn and Ge in BA6 did not affect the ratio Mo/W of the $(Nb, Mo)_{ss}$ which was ~ 2, but the (Mo+W) content was lowered by ~ 18.8%. By increasing the nominal concentrations of Sn and Ge, the concentrations of Ti, Hf, Sn and Ge in the $(Nb, Mo)_{ss}$ increased whereas those of Mo, W and Si decreased. Compared with Nb-20Si-5Mo-3W (alloy YG6) (Grammenos and Tsakiropoulos, 2011) in which there was Nb solid solution with or without Si, the ratio Mo/W was ~ 2, as in BA1 and BA6.

But the Mo+W content was lower by 46.2% and 33.7% in YG6 for the Nb solid solution with Si than in BA1-AC and BA6-AC, respectively. For the Nb solid solution without Si, the Mo+W content in the YG6 was 40.9% lower than that in BA1-AC.

In BA1 and BA6, increase in Ge+Hf+Sn+Ti in the Nb_{ss} led to a decrease in Mo+W.

The data for the alloys BA1-AC, BA6-AC and YG6-AC suggest that the Mo/W ratio is about 2 in the $(Nb, Mo)_{ss}$ in alloys with RMs (Mo, W) and with or without Ti, Ge, Hf and Sn.

In the 5-3 silicides of BA1-AC and BA6-AC, the Mo+W was constant at ~ 3.5 at% and did not change as the concentrations of Sn and Ge increased in the alloy BA6. However, the Sn+Ge increased from 3.5 to 8.2 at% with increase of Ge being significant. This confirmed that Ge partitioned to 5-3 silicide. The concentrations of Sn and Ge in the 5-3 silicide were consistent with Nb silicide alloys with or without Mo or W additions whereas the concentrations of Mo and W was not in agreement with Ti and/or Hf containing Nb silicide alloys where the Mo+W content in the Nb_5Si_3 was essentially zero.

Compared with YG6 and YG8 (Grammenos and Tsakiropoulos, 2011) where the Mo+W content of the Nb_5Si_3 was essentially zero, the data for BA1-AC and BA6-AC would suggest that the higher Mo+W content in the Nb_5Si_3 could be attributed to the synergy of Sn and Ge with low concentrations of Ti and Hf.

3.4.2 Heat treated

3.4.2.1 Phases present after heat treatment

After the heat treatment, the phases present in the alloys were the $(Nb, Mo)_{ss}$, $(Nb, Ti)_3Sn$, $\alpha(Nb, Ti)_5Si_3$ and HfO_2 in BA1-HT, and $(Nb, Mo)_{ss}$ no Si, $(Nb, Ti)_3Sn$, $\alpha(Nb, Ti)_5Si_3$, HfO_2 and TiN in BA6-HT. Thus the transformation $\beta Nb_5Si_3 \rightarrow \alpha Nb_5Si_3$ had been completed and the equilibrium microstructure in the alloys consisted of $(Nb, Mo)_{ss}$, $(Nb, Ti)_3Sn$, $\alpha(Nb, Ti)_5Si_3$. In the $(Nb, Ti)_3Sn$ in both alloys, the Si+Sn+Ge was about 18.5 at% and the data for BA6-HT showed a significant increase in the concentration of Sn in the $(Nb, Ti)_3Sn$ after the heat treatment.

The concentrations of alloying elements in the $\alpha(Nb, Ti)_5Si_3$ in BA6-HT were similar to those in $\beta(Nb, Ti)_5Si_3$ of BA6-AC. The same similarity was observed in BA1 except for the concentrations of Mo and W which decreased after the heat treatment.

3.4.2.2 Microstructures of the heat treated alloys

The microstructures of BA1-HT and BA6-HT had coarsened, and there was significant vol% of bright contrast precipitates in the silicide phase in BA6-HT but not in BA1-HT. The BA6-HT specimen seemed to consist of two halves but the large area EDS of both halves did not show significant difference in composition. The main difference was some localised microstructures seen on the upper halve of the specimen, see Figure 3.6f, where the area with bright phase precipitates in the α(Nb, Ti)$_5$Si$_3$ seemed to be separated by darker contrast region, suggesting enrichment in low Z (atomic number) element like Ti.

The EDS data for the A15 suggest two kinds of Nb$_3$Sn in the as cast microstructure: (i) (Nb, Mo)$_3$Sn (see Table 3.5) and (ii) (Nb, Ti)$_3$Sn (see text in section 3.3.2). The micrograph (Figure 3.5a-c) showed similar microstructures from middle to very-bottom but different from very-top to the middle. During melting, the ingot separated into two halves on cooling, but was intact after final round of re-melting. This suggests there was liquid miscibility gap which severity keeps decreasing with re-melting, probably due to decrease in Sn.

The localised microstructure (after HT) and the composition difference of the A15 (in AC condition) supports there was miscibility gap in the cast alloy which closed up in the A15 and opened out in the 5-3 silicide after the heat treatment. It is concluded that there were two events in the microstructure of the alloy BA6 during the heat treatment namely: (i) βNb$_5$Si$_3$ → αNb$_5$Si$_3$ transformation and (ii) miscibility gap opening out in the 5-3 silicide. The latter was considered to be the cause of the precipitation of the bright contrast phase believed to be Nb$_{ss}$, and the low Z-element enriched areas at the edges of the α(Nb, Ti)$_5$Si$_3$. Considering there was no similar precipitation accompanying the βNb$_5$Si$_3$ → αNb$_5$Si$_3$ in BA1-HT the precipitation of the bright phase and low Z element enrichment might not be linked with βNb$_5$Si$_3$ → αNb$_5$Si$_3$ + Nb$_{ss}$ transformation suggested by Zelenitsas and Tsakiropoulos, (2005). Thus, there was additional event in the microstructure which effect was not strong at low concentrations of Sn and Ge. It is also suggested that Nb silicide alloy with αNb$_5$Si$_3$ in the cast microstructure will precipitate Nb$_{ss}$ if miscibility gap opens out in it.

According to the EDS data in the Table 3.4, two types of $(Nb, Mo)_{ss}$ are present in BA1-HT. These are $(Nb, Mo)_{ss}$ with and without Si. The former had Mo+W = 16.2 at% and Mo/W = 2.2. The Mo+W had decreased compared with BA1-AC. For the $(Nb, Mo)_{ss}$ with no Si, the Mo+W was 17.2 at% and Mo/W was 2.3.

In the BA6-HT, only the $(Nb, Mo)_{ss}$ with no Si was formed with Mo+W = 36.8 at% and Mo/W = 1.7. The data for the $(Nb, Mo)_{ss}$ in BA1-HT and BA6-HT would suggest that the formation of Nb_{ss} with no Si is driven (i) by the increasing Mo+W content of the solid solution and (ii) decreasing the Mo/W in the Nb_{ss}. Table 3.7 compares the Mo+W and Mo/W data for cast alloys and the Nb_{ss} with no Si in as cast and heat treated alloys (BA1, BA6, YG6 and YG8).

The data shows (i) that as the Mo+W content of the Nb_{ss} in BA1 and BA6 decreased that the Mo/W ratio increased, (ii) that the synergy of low concentrations of Ti and Hf with low concentrations of Sn and Ge led to stronger partitioning of Mo and W to Nb_{ss} in the as cast alloy, (iii) that the synergy of low concentrations of Ti and Hf with higher concentrations of Sn and Ge reduced the partitioning of Mo and W to Nb_{ss} in the as cast alloy, (iv) that there is stronger partition of Mo and W to Nb_{ss} after heat treatment at higer concentrations of Sn and Ge, and (v) that the Mo/W ratio did not vary much compared with the Mo+W in the alloys BA1, BA6 and YG6.

3.4.2.3 Lattice parameters of Nb_{ss}, αNb_5Si_3, βNb_5Si_3 and Nb_3Sn

The lattice parameters of the phases observed in the cast and heat treated alloys are given in Table 3.2. The data showed that the $(Nb, Mo)_{ss}$ had lower lattice parameters than unalloyed Nb in both alloys and conditions. The atomic radii (Å) of unalloyed Nb, Ti, Hf, Mo, W, Si, Sn and Ge are 1.45, 1.40, 1.55, 1.45, 1.35, 1.10, 1.45 and 1.25Å (Slater, 1964). Thus the substitution for Nb atoms with lower atomic radii elements caused the decrease in the lattice parameters of the $(Nb, Mo)_{ss}$ compared to the unalloyed Nb.

Similarly, in the $\alpha(Nb, Ti)_5Si_3$, $\beta(Nb, Ti)_5Si_3$ and A15, Mo, W, Ti and Hf substituted for Nb atoms whiles Sn and Ge for Si in the silicide, and Ge and Si for Sn in the A15.

The difference in lattice parameters of the $(Nb, Mo)_{ss}$, $\alpha(Nb, Ti)_5Si_3$ and A15 in BA1-HT and BA6-HT compared to the cast BA1-AC and BA6-AC was due to solute redistribution after the heat treatment.

Table 3.7 Comparison of Mo+W and Mo/W in Nb_{ss} with no Si in BA1 and BA6 with YG6 and YG8 alloys

Nominal alloy composition / alloy code	**Nominal Values (at%)**		**Actual values (at%) in Nb_{ss} no Si**			
			As cast		**Heat treated**	
	Mo+W	**Mo/W**	**Mo+W**	**Mo/W**	**Mo+W**	**Mo/W**
Nb-11Ti-18Si-1Hf-**6**Mo-**2.5**W-2Sn-2Ge (BA1)	8.5	2.4	23.5	1.8	17.2	2.3
Nb-11Ti-18Si-1Hf-**6**Mo-**2.5**W-5Sn-5Ge (BA6)	8.5	2.4	-	-	36.8	1.7
Nb-20Si-**5**Mo-**3**W (YG6)	8	1.7	13.9	1.7	13.8	2.6
Nb-20Si-5Hf-**5**Mo-**3**W (YG8)	8	1.7	-	-	18.2	1.3

3.5 Conclusions

The microstructures of the alloys BA1 and BA6 were studied in the as cast and heat treated conditions. The following conclusions were made:

1. The phases present in the BA1-AC and BA1-HT were $\alpha(Nb, Ti)_5Si_3$, $\beta(Nb, Ti)_5Si_3$, $(Nb, Mo)_{ss}$ and HfO_2, and $\alpha(Nb, Ti)_5Si_3$, $(Nb, Mo)_{ss}$, A15 and HfO_2, respectively. In the BA6-AC and BA6-HT, the phases present were $\beta(Nb, Ti)_5Si_3$, $(Nb, Mo)_{ss}$, A15 and HfO_2, and $\alpha(Nb, Ti)_5Si_3$, $(Nb, Mo)_{ss}$ no Si, A15, HfO_2 and TiN respectively.
2. The A15 was stabilised in the heat treated alloys but was formed only in the as cast alloy BA6.

3. The increase in Sn and Ge concentration in BA6 led to formation of ternary eutectic and reduced the macrosegregation of Si significantly.
4. The synergy of low concentrations of Hf and Ti with Sn and Ge led to strong partition of Mo and W to Nb_{ss} and that the partitioning was stronger after heat treatment at higher concentrations of Sn and Ge.
5. Mo and W had opposite segregation behaviour with Hf, Si, Sn and Ti in the Nb_{ss}.
6. The critical concentration of Sn required for formation of A15 in the cast alloy of this study is in the range 1.8 at% < Sn < 4 at%, and Sn/Ge < 1.
7. Germanium partitioned to Nb_5Si_3 rather than A15 and Sn partitioned to the Nb_{ss}. The increase in Ge, Hf and Ti concentrations in the Nb_5Si_3 resulted to a decrease in the concentrations of Mo, Si and W.

CHAPTER 4

THE MICROSTRUCTURE OF Nb-11Ti-18Si-1Hf-6Mo-2.5W-xSn-xGe-xCr-xAl

CONTENTS REMOVED.

CHAPTER 5

STUDY OF THE EFFECTS OF Ti CONCENTRATION ON MICROSTRUCTURE OF Nb-xTi-18Si-1Hf-6Mo-2.5W-5Sn-5Ge-5Cr-5Al

CONTENTS REMOVED.

CHAPTER 6

MACROHARDNESS AND OXIDATION BEHAVIOUR OF SELECTED ALLOYS OF THIS STUDY

CONTENTS REMOVED.

CHAPTER 7

CONCLUSIONS AND SUGGESTIONS FOR FUTURE WORK

CONTENTS REMOVED.

REFERENCES

ABBASCHIAN, R. & LIPSCHUTZ, M. D. 1997. Eutectic solidification processing via bulk melt undercooling. *Materials Science and Engineering A,* 226-228**,** 13-21.

ANTONOVA, N., FIRSTOV, S. A. & MIRACLE, D. B. 2003. Ti-Nb Phase Diagram, ASM Alloy Phase Diagram Database™. *In:* VILLARS, P., EDITOR-IN-CHIEF., OKAMOTO, H. & CENZUAL, K., SECTION EDITORS (eds.) http://www1.asminternational.org/AsmEnterprise/APD, ASM International, Materials Park, OH, 2006.

BEGLEY, R. T. 1994. Columbium Alloy Development at Westinghouse. *In:* DALDER, E. N. C., GROBSTEIN, T. & OLSEN, C. S. (eds.) *Evolution of Refractory Metals and Alloys* Warrendale, PA: The Minerals, Metals & Materials Society.

BEGLEY, R. T. & BECHTOLD, J. H. 1961. Effect of alloying on the mechanical properties of niobium. *Journal of The Less-Common Metals,* 3**,** 1-12.

BERTHOD, P. 2005. Kinetics of High Temperature Oxidation and Chromia Volatilization for a Binary Ni–Cr Alloy. *Oxidation of Metals,* 64**,** 235-252.

BEWLAY, B. P., JACKSON, M. R. & GIGLIOTTI, M. F. X. 2002. Niobium Silicide High Temperature In Situ Composites *In:* WESTBROOK, J. H. & FLEISCHER, R. I. (eds.) *Intermetallic Compounds-Principles and Practice.* John Wiley and Sons Ltd.

BEWLAY, B. P., JACKSON, M. R. & LIPSITT, H. A. 1996. The balance of mechanical and environmental properties of a multielement niobium-niobium silicide-based in situ composite. *Metallurgical and Materials Transactions A: Physical Metallurgy and Materials Science,* 27**,** 3801-3808.

BEWLAY, B. P., JACKSON, M. R. & LIPSITT, H. A. 1997. The Nb-Ti-Si Ternary Phase Diagram: Evaluation of Liquid-Solid Phase Equilibria in Nb- and Ti-Rich Alloys. *Journal of Phase Equilibria,* 18**,** 264-278.

BEWLAY, B. P., JACKSON, M. R., ZHAO, J.-C., SUBRAMANIAN, P. R., MENDIRATTA, M. G. & LEWANDOWSKI, J. J. 2003a. Ultrahigh-Temperature Nb-Silicide-Based Composites. *MRS Bulletin*.

BEWLAY, B. P., JACKSON, M. R., ZHAO, J. C. & SUBRAMANIAN, P. R. 2003b. A review of very-high-temperature Nb-silicide-based composites. *Metallurgical and Materials Transactions A: Physical Metallurgy and Materials Science,* 34 A**,** 2043-2052.

BEWLAY, B. P., YANG, Y., CASEY, R. L., JACKSON, M. R. & CHANG, Y. A. 2009. Experimental study of the liquid-solid phase equilibria at the metal-rich region of the Nb-Cr-Si system. *Intermetallics,* 17**,** 120-127.

CHAN, K. S. 2002. Alloying effects on fracture mechanisms in Nb-based intermetallic in-situ composites. *Materials Science and Engineering A,* 329-331**,** 513-522.

CHAN, K. S. 2005. Alloying effects on the fracture toughness of Nb-based silicides and Laves phases. *Materials Science and Engineering: A,* 409**,** 257-269.

CHAN, K. S. & DAVIDSON, D. L. 1999. Effects of Ti addition on cleavage fracture in Nb-Cr-Ti solid-solution alloys. *Metallurgical and Materials Transactions A: Physical Metallurgy and Materials Science,* 30**,** 925-939.

CHATTOPADHYAY, K., SINHA, R., MITRA, R. & RAY, K. K. 2007. Effect of Mo and Si on morphology and volume fraction of eutectic in Nb-Si-Mo alloys. *Materials Science and Engineering A,* 456**,** 358-363.

CHEN, S. L., DANIEL, S., ZHANG, F., CHANG, Y. A., YAN, X. Y., XIE, F. Y., SCHMID-FETZER, R. & OATES, W. A. 2002. The PANDAT software package and its applications. *Calphad: Computer Coupling of Phase Diagrams and Thermochemistry,* 26**,** 175-188.

DAI, R., ZHANG, J. F., ZHANG, S. G. & LI, J. G. 2013. Liquid immiscibility and core-shell morphology formation in ternary Al–Bi–Sn alloys. *Materials Characterization,* 81**,** 49-55.

GENG, J. & TSAKIROPOULOS, P. 2007. A study of the microstructures and oxidation of Nb-Si-Cr-Al-Mo in situ composites alloyed with Ti, Hf and Sn. *Intermetallics,* 15**,** 382-395.

GENG, J., TSAKIROPOULOS, P. & SHAO, G. 2006a. The effects of Ti and Mo additions on the microstructure of Nb-silicide based in situ composites. *Intermetallics,* 14**,** 227-235.

GENG, J., TSAKIROPOULOS, P. & SHAO, G. 2006b. Study of three-phase equilibrium in the Nb-rich corner of Nb-Si-Cr system. *Intermetallics,* 14**,** 832-837.

GENG, J., TSAKIROPOULOS, P. & SHAO, G. 2007a. A study of the effects of Hf and Sn additions on the microstructure of Nbss/Nb5Si3 based in situ composites. *Intermetallics,* 15**,** 69-76.

GENG, J., TSAKIROPOULOS, P. & SHAO, G. 2007b. A thermo-gravimetric and microstructural study of the oxidation of Nbss/Nb5Si3-based in situ composites with Sn addition. *Intermetallics,* 15**,** 270-281.

GENG, T., LI, C., DU, Z., GUO, C., ZHAO, X. & XU, H. 2011. Thermodynamic assessment of the Nb-Ge system. *Journal of Alloys and Compounds,* 509**,** 3080-3088.

GOKHALE, A. B. & ABBASCHIAN, G. J. 1990. Mo-Si Phase Diagram, ASM Alloy Phase Diagram Database™. *In:* VILLARS, P., EDITOR-IN-CHIEF., OKAMOTO, H. & CENZUAL, K., SECTION EDITORS (eds.). http://www1.asminternational.org/AsmEnterprise/APD, ASM International, Materials Park, OH, 2006.

GOLDSCHMIDT, H. J. & BRAND, J. A. 1961a. The Constitution of the Chromium-Niobium-Molybdenum System. *J. Less-Common Metals,* 3**,** 44-61.

GOLDSCHMIDT, H. J. & BRAND, J. A. 1961b. The Constitution of the Chromium-Niobium-Silicon System. *J. Less-Common Metals,* 3**,** 34-43.

GRAMMENOS, I. & TSAKIROPOULOS, P. 2010. Study of the role of Al, Cr and Ti additions in the microstructure of Nb-18Si-5Hf base alloys. *Intermetallics,* 18**,** 242-253.

GRAMMENOS, I. & TSAKIROPOULOS, P. 2011. Study of the role of Hf, Mo and W additions in the microstructure of Nb-20Si silicide based alloys. *Intermetallics,* 19**,** 1612-1621.

GRILL, R. & GNADENBERGER, A. 2006. Niobium as mint metal: Production-properties-processing. *International Journal of Refractory Metals and Hard Materials,* 24**,** 275-282.

HAN, X. J. & WEI, B. 2002. Microstructural Characteristics of Ni-Sb Eutectic Alloys under Substantial Undercooling and Containerless Solidification Conditions. *Metallurgical and Materials Transactions A,* 33A**,** 1221-1228.

JACKSON, M. R. & BEWLAY, B. 1999. *Silicide composite with niobium-based metallic phase and silicon-modified laves phase.* . United States patent application 09/131,609.

JACKSON, M. R., BEWLAY, B. P. & BRIANT, C. L. 2002. *Creep Resistant Nb-Silicide Based Two-Phase Composites*. United States patent application 09/651,667.

JACKSON, M. R., BEWLAY, B. P., ROWE, R. G., SKELLY, D. W. & LIPSITT, H. A. 1996. High-temperature refractory metal-intermetallic composites. *JOM,* 48**,** 39-44.

KAUFMAN, L. & NESOR, H. 1975. Nb-Ti-W Phase Diagram, ASM Alloy Phase Diagram Database™. *In:* VILLARS, P., EDITOR-IN-CHIEF., OKAMOTO, H. & CENZUAL, K., SECTION EDITORS (eds.). http://www1.asminternational.org/AsmEnterprise/APD, ASM International, Materials Park, OH, 2006.

KIM, J.-H., TABARU, T., HIRAI, H., KITAHARA, A. & HANADA, S. 2003. Tensile properties of a refractory metal base in situ composite consisting of an Nb solid solution and hexagonal Nb5Si3. *Scripta Materialia,* 48**,** 1439-1444.

KIM, W. Y., TANAKA, H. & HANADA, S. 2002. High temperature strength at 1773 K and room temperature fracture toughness of Nbss/Nb5Si3 in situ composites alloyed with Mo. *Journal of Materials Science,* 37**,** 2885-2891.

KOFF, B. L. 2004. Gas Turbine Technology Evolution: A Designer's Perspective. *JOURNAL OF PROPULSION AND POWER,* 20**,** 577-595.

LI, M. & KURIBAYASHI, K. 2003. Nucleation-controlled microstructures and anomalous eutectic formation in undercooled Co-Sn and Ni-Si eutectic melts. *Metallurgical and Materials Transactions A: Physical Metallurgy and Materials Science,* 34**,** 2999-3008.

MA, C. L., LI, J. C., TAN, Y., TANAKA, R. & HANADA, S. 2004. Microstructure and mechanical properties of Nb/Nb5Si3 in situ composites in Nb-Mo-Si and Nb-W-Si systems. *Materials Science and Engineering A,* 386**,** 375-383.

MA, C. L., TAN, Y., TANAKA, H., KASAMA, A., TANAKA, R., MIURA, S., MISHIMA, Y. & HANADA, S. 2000. Phase equilibria in Nb-Mo-rich zone of the Nb-Si-Mo ternary system. *Materials Transactions, JIM,* 41**,** 1329-1336.

MIRKOVIĆ, D., GRÖBNER, J. & SCHMID-FETZER, R. 2008. Liquid demixing and microstructure formation in ternary Al–Sn–Cu alloys. *Materials Science and Engineering: A,* 487**,** 456-467.

MITRA, R. 2006. Mechanical behaviour and oxidation resistance of structural silicides. *International Materials Reviews,* 51**,** 13-64.

MURAKAMI, T., SASAKI, S., ICHIKAWA, K. & KITAHARA, A. 2001. Microstructure, mechanical properties and oxidation behaviour of Nb-Si-Al and Nb-Si-N powder compacts prepared byspark plasma sintering. *Intermetallics,* 9**,** 621-627.

MURRAY, J. L. 1990. Ti-W Phase Diagram, ASM Alloy Phase Diagram Database™. *In:* VILLARS, P., EDITOR-IN-CHIEF., OKAMOTO, H. & CENZUAL, K., SECTION EDITORS (eds.). http://www1.asminternational.org/AsmEnterprise/APD, ASM International, Materials Park, OH, 2006.

NAIDU, S. V. N., SRIRAMAMURTHY, A. M. & RAMA RAO, P. 1990a. Nb-W Phase Diagram, ASM Alloy Phase Diagram Database™. *In:* VILLARS, P., EDITOR-IN-CHIEF., OKAMOTO, H. & CENZUAL, K., SECTION EDITORS (eds.). http://www1.asminternational.org/AsmEnterprise/APD, ASM International, Materials Park, OH, 2006.

NAIDU, S. V. N., SRIRAMAMURTHY, A. M. & RAMA RAO, P. 1990b. Si-W Phase Diagram, ASM Alloy Phase Diagram Database™. *In:* VILLARS, P., EDITOR-IN-CHIEF., OKAMOTO, H. & CENZUAL, K., SECTION EDITORS (eds.). http://www1.asminternational.org/AsmEnterprise/APD, ASM International, Materials Park, OH, 2006.

NETO, J. G. C., FRIES, S. G., LUKAS, H. L., GAMA, S. & EFFENBERG, G. 1993. Nb-Cr Phase Diagram, ASM Alloy Phase Diagram Database™. *In:* VILLARS, P., EDITOR-IN-CHIEF., OKAMOTO, H. & CENZUAL, K., SECTION EDITORS (eds.). http://www1.asminternational.org/AsmEnterprise/APD, ASM International, Materials Park, OH, 2006.

OKAMOTO, H. 1991. Mo-Nb Phase Diagram, ASM Alloy Phase Diagram Database™. *In:* VILLARS, P., EDITOR-IN-CHIEF., OKAMOTO, H. & CENZUAL, K., SECTION EDITORS (eds.). http://www1.asminternational.org/AsmEnterprise/APD, ASM International, Materials Park, OH, 2006.

OKAMOTO, H. 2001. Cr-Si Phase Diagram, ASM Alloy Phase Diagram Database™. *In:* VILLARS, P., EDITOR-IN-CHIEF., OKAMOTO, H. & CENZUAL, K., SECTION EDITORS (eds.). http://www1.asminternational.org/AsmEnterprise/APD, ASM International, Materials Park, OH, 2006.

OKAMOTO, H. 2002. Cr-Ti Phase Diagram, ASM Alloy Phase Diagram Database™. *In:* VILLAS, P., EDITOR-IN-CHIEF., OKAMOTO, H. & CENZUAL, K., SECTION EDITORS. (eds.) http://www1.asminternational.org/AsmEnterprise/APD, ASM International, Materials Park, OH, 2006.

OKAMOTO, H. 2003. Nb-Sn Phase Diagram, ASM Alloy Phase Diagram Database™. *In:* VILLARS, P., EDITOR-IN-CHIEF., OKAMOTO, H. & CENZUAL, K., SECTION EDITORS (eds.). http://www1.asminternational.org/AsmEnterprise/APD, ASM International, Materials Park, OH, 2006.

OKAMOTO, H., GOKHALE, A. B. & ABBASCHIAN, G. J. 1990. Nb-Si Phase Diagram, ASM Alloy Phase Diagram Database™. *In:* VILLARS, P., EDITOR-IN-CHIEF., OKAMOTO, H. & CENZUAL, K., SECTION EDITORS (eds.). http://www1.asminternational.org/AsmEnterprise/APD, ASM International, Materials Park, OH, 2006.

OLESINSKI, R. W. & ABBASCHIAN, G. J. 1990. Ge-Si Phase Diagram, ASM Alloy Phase Diagram Database™. *In:* VILLARS, P., EDITOR-IN-CHIEF., OKAMOTO, H. & CENZUAL, K., SECTION EDITORS (eds.). http://www1.asminternational.org/AsmEnterprise/APD, ASM International, Materials Park, OH, 2006.

PAN, V. M., LATYSHEVA, V. I., KULIK, O. G. & POPOV, A. G. 1982. Ge-Nb-Si Phase Diagram, ASM Alloy Phase Diagram Database™. *In:* VILLARS, P., EDITOR-IN-CHIEF., OKAMOTO, H. & CENZUAL, K., SECTION

EDITORS (eds.). http://www1.asminternational.org/AsmEnterprise/APD, ASM International, Materials Park, OH, 2006.

PARLAKYIGIT, A. & KARAOGLANLI, A. 2014. Effects of Microstructural Transformation in TBCs Consisting of NiCrAlY Metallic Bond Coat and YSZ Ceramic Top Coat after Oxidation at 900° C. *Acta Physica Polonica A,* 125**,** 232-234.

PINT, B. A., DISTEFANO, J. R. & WRIGHT, I. G. 2006. Oxidation resistance: One barrier to moving beyond Ni-base superalloys. *Materials Science and Engineering A,* 415**,** 255-263.

QU, S., HAN, Y. & SONG, L. 2007. Effects of alloying elements on phase stability in Nb-Si system intermetallics materials. *Intermetallics,* 15**,** 810-813.

RAGHAVAN, V. 2005. Al-Nb-Ti Phase Diagram, ASM Alloy Phase Diagram Database™ *In:* VILLARS, P., EDITOR-IN-CHIEF., OKAMOTO, H. & CENZUAL, K., SECTION EDITORS (eds.). http://www1.asminternational.org/AsmEnterprise/APD, ASM International, Materials Park, OH, 2006.

RAGHAVAN, V. 2011. Al-Cr-Nb (Aluminum-Chromium-Niobium). *Journal of Phase Equilibria and Diffusion,* 32**,** 241.

SAUTHOFF, G. 1996. State of intermetallics development. *Materials and Corrosion - Werkstoffe und Korrosion,* 47**,** 589-594.

SCHLESINGER, M. E., OKAMOTO, H., GOKHALE, A. & ABBASCHIAN, R. 1993. The Nb-Si (niobium-silicon) system. *Journal of Phase Equilibria,* 14**,** 502-509.

SEIFERT, H. J., LUKAS, H. L. & PETZOW, G. 1996. Ti-Si Phase Diagram, ASM Alloy Phase Diagram Database™. *In:* VILLARS, P., EDITOR-IN-CHIEF., OKAMOTO, H. & CENZUAL, K., SECTION EDITORS (eds.). http://www1.asminternational.org/AsmEnterprise/APD, ASM International, Materials Park, OH, 2006.

SHAO, G. 2004. Thermodynamic assessment of the Nb-Si-Al system. *Intermetallics,* 12**,** 655-664.

SHAO, G. 2005. Thermodynamic modelling of the Cr-Nb-Si system. *Intermetallics,* 13**,** 69-78.

SLATER, J. C. 1964. Atomic radii in crystals. *The Journal of Chemical Physics,* 41**,** 3199-3204.

SUBRAMANIAN, P. R., MENDIRATTA, M. G., DIMIDUK, D. M. & STUCKE, M. A. 1997. Advanced intermetallic alloys - Beyond gamma titanium aluminides. *Materials Science and Engineering A,* 239-240**,** 1-13.

SUN, Z., GUO, X. & ZHANG, C. 2012. Thermodynamic modeling of the Nb-rich corner in the Nb-Si-Sn system. *Calphad: Computer Coupling of Phase Diagrams and Thermochemistry,* 36**,** 82-88.

SVECHNIKOV, V. N., SHURIN, A. K. & ALFINTSEVA, R. A. 1970. Hf-Mo-Nb Phase Diagram, ASM Alloy Phase Diagram Database™. *In:* VILLARS, P., EDITOR-IN-CHIEF., OKAMOTO, H. & CENZUAL, K., SECTION EDITORS (eds.). http://www1.asminternational.org/AsmEnterprise/APD, ASM International, Materials Park, OH, 2006.

TAUB, A. I. & FLEISCHER, R. L. 1989. Intermetallic compounds for high-temperature structural use. *Science,* 243**,** 616-621.

TSAKIROPOULOS, P. 2010. Beyond Nickel-Based Superalloys. *In:* BLOCKLEY, R. & SHYY, W. (eds.) *Encyclopedia of Aerospace Engineering.* John Wiley & Sons, Ltd.

TSAKIROPOULOS, P. 2014. *RE: Private communication.*

TURCHI, P. E. A., KAUFMAN, L. & LIU Z.K. 2006. Cr-Mo Phase Diagram, ASM Alloy Phase Diagram Database™. *In:* VILLARS, P., EDITOR-IN-CHIEF., OKAMOTO, H. & CENZUAL, K., SECTION EDITORS (eds.). http://www1.asminternational.org/AsmEnterprise/APD, ASM International, Materials Park, OH, 2006.

VELLIOS, N. & TSAKIROPOULOS, P. 2007. The role of Sn and Ti additions in the microstructure of Nb-18Si base alloys *Intermetallics,* 15**,** 1518-1528.

VENKATRAMAN, M. & NEUMANN, J. P. 1990. Cr-Sn Phase Diagram, ASM Alloy Phase Diagram Database™. *In:* VILLARS, P., EDITOR-IN-CHIEF., OKAMOTO, H. & CENZUAL, K., SECTION EDITORS (eds.). http://www1.asminternational.org/AsmEnterprise/APD, ASM International, Materials Park, OH, 2006.

WANG, C. P., LIU, X. J., OHNUMA, I., KAINUMA, R. & ISHIDA, K. 2005. Design and development of the self-assemble Cu-Fe base composites. *Journal of Materials and Metallurgy,* 4**,** 127-131.

YANG, Y., BEWLAY, B. P., CHEN, S.-L. & CHANG, Y. A. 2007. Application of phase diagram calculations to development of new ultra-high temperature structural materials. *Transactions of Nonferrous Metals Society of China,* 17**,** 1396-1404.

YANG, Y., CHANG, Y. A., ZHAO, J. C. & BEWLAY, B. P. 2003. Thermodynamic modeling of the Nb-Hf-Si ternary system. *Intermetallics,* 11**,** 407-415.

ZAKHAROV, A. M. & SAVITSKII, E. M. 1966. Mo-Ti-W Phase Diagram, ASM Alloy Phase Diagram Database™. *In:* VILLARS, P., EDITOR-IN-CHIEF., OKAMOTO, H. & CENZUAL, K., SECTION EDITORS (eds.). http://www1.asminternational.org/AsmEnterprise/APD, ASM International, Materials Park, OH, 2006.

ZELENITSAS, K. 2005. *Study of Niobium Silicide-based Alloys for Operational Temperatures Beyond 1150 °C* PhD, The University of Sheffield.

ZELENITSAS, K. & TSAKIROPOULOS, P. 2005. Study of the role of Al and Cr additions in the microstructure of Nb–Ti–Si in situ composites. *Intermetallics,* 13**,** 1079–1095.

ZELENITSAS, K. & TSAKIROPOULOS, P. 2006a. Effect of Al, Cr and Ta additions on the oxidation behaviour of Nb–Ti–Si in situ composites at 800 ◦C. *Materials Science and Engineering A,* 416**,** 269–280.

ZELENITSAS, K. & TSAKIROPOULOS, P. 2006b. Study of the role of Ta and Cr additions in the microstructure of Nb-Ti-Si-Al in situ composites. *Intermetallics,* 14**,** 639-659.

ZHAO, J. C., JACKSON, M. R. & PELUSO, L. A. 2003. Determination of the Nb-Cr-Si phase diagram using diffusion multiples. *Acta Materialia,* 51**,** 6395-6405.

ZHAO, J. C., JACKSON, M. R. & PELUSO, L. A. 2004a. Cr-Nb-Ti Phase Diagram, ASM Alloy Phase Diagram Database™. *In:* VILLARS, P., EDITOR-IN-CHIEF., OKAMOTO, H. & CENZUAL, K., SECTION EDITORS (eds.).

http://www1.asminternational.org/AsmEnterprise/APD, ASM International, Materials Park, OH, 2006.

ZHAO, J. C., JACKSON, M. R. & PELUSO, L. A. 2004b. Evaluation of Phase Relations in the Nb-Cr-Al System at 1000°C Using a Diffusion-Multiple Approach. *Journal of Phase Equilibria and Diffusion,* 25**,** 152-159.

ZHAO, J. C., JACKSON, M. R. & PELUSO, L. A. 2004c. Mapping of the Nb-Ti-Si phase diagram using diffusion multiples. *Materials Science and Engineering A,* 372**,** 21-27.

ZIFU, L. 2012. *Thesis* PhD, The University of Sheffield.

ZIFU, L. & TSAKIROPOULOS, P. 2010. Study of the effects of Ge addition on the microstructure of Nb-18Si in situ composites. *Intermetallics,* 18**,** 1072-1078.

ZIFU, L. & TSAKIROPOULOS, P. 2011. Study of the effect of Ti and Ge in the microstructure of Nb-24Ti-18Si-5Ge in situ composite. *Intermetallics,* 19**,** 1291-1297.